

NORTHWESTERN UNIVERSITY

Expanding the Properties and Utility of DNA-Engineered Nanoparticle Superlattices through
Monodispersity, Metallization, and Interfacing with Electronic Circuitry

A DISSERTATION

SUBMITTED TO THE GRADUATE SCHOOL
IN PARTIAL FULFILLMENT OF THE REQUIREMENTS

For the degree

DOCTOR OF PHILOSOPHY

Field of Materials Science and Engineering

By

Taegon Oh

EVANSTON, ILLINOIS

March 2019

© Copyright by Taegon Oh 2019

All Rights Reserved

Abstract

Expanding the Properties and Utility of DNA-Engineered Nanoparticle Superlattices through Monodispersity, Metallization, and Interfacing with Electronic Circuitry

Taegon Oh

Colloidal crystal engineering with DNA offers new opportunities for materials scientists to build and program the structures of superlattices beyond what can be accomplished in Nature with atomic crystal lattices. Thus far, such materials primarily have been studied for their optical properties due to the insulating nature of the DNA bonds and the large distances between the particles, a consequence of DNA length. In addition, the size heterogeneity of the colloidal crystals generated by all known techniques, limits the use of such structures for device applications. My thesis introduces strategies for controlling the growth and monodispersity of colloidal crystals engineered with DNA, introduces a novel way to metallize and strengthen the DNA bond interconnects, so that such structures can be moved from aqueous media into a wide variety of other media, and explores the functional consequences of metallization in the context of conductivity.

Chapter 1 reviews the field of colloidal crystal engineering with DNA, setting the stage for the experiments carried out in this thesis. In Chapter 2, On Wire Lithography (OWL) is used to create nanowire devices that allow for the selective functionalization of electrodes with DNA and the controlled growth of nanoparticle devices in a pre-designed nanogap. Chapter 3 takes inspiration from biology where density gradients are used to separate proteins based upon size. In Chapter 3, a powerful density gradient method for controlling the growth of superlattices in such a way that they can be driven to one size is described. In this method, growth quenching is effected by the superlattices falling into sublayers that do not permit growth. Chapter 4 describes a post-

synthetic stabilization procedure for DNA-assembled colloidal crystals that relies on Ag^+ ions to form coordinate covalent bonds between the nucleobases in the “DNA bonds”. This substantially increases the stability of such structures and avoids the need to move them into solid-state matrices to study or use them.

Using the methods introduced in Chapter 2 and the synthetic procedures described in Chapters 3 and 4, the work in Chapter 5 explores the conductivity of the metallized superlattices, showing that Ag^+ not only stabilizes the DNA bonds but transforms them into conducting entities. Chapter 6 provides a forward looking perspective and examines the consequences of these advances with respect to generating programmable device architectures based upon nanoparticle superlattices engineered with DNA.

Thesis Advisor: Professor Chad A. Mirkin

Acknowledgements

First and most importantly, I thank God for my talents, health, opportunities, and all the other blessings offered to me and my family. I stand upon these blessings, as taught by Paul “*I can do all this through him who gives me strength.*” I especially appreciate the blessing of relationships with the people I met during my Ph. D. program, many of whom are listed below.

Special thanks to my advisor Professor Chad Mirkin, who provided me and my research with much inspiration and freedom, enabling independent scientific thought and a research environment not limited by resources. Without this inspiration and freedom, I cannot imagine completing (or even starting) any of the projects that make up my thesis. He also advised me on how to improve my personal attributes, represented by the following adjectives: proactive (on conducting research), confident (on my thoughts), clear (on expressions), and patient (for the right time to discuss and complete work). I will not forget these words, as he once recommended me to write them on my bathroom mirror and shout out each morning!

I also appreciate my committee, Professor Vinayak Dravid, Professor Lincoln Lauhon, and Professor George Schatz for their encouragement, support, and helpful discussions throughout the program.

I really appreciate the great mentorship and friendship of my former officemates. Dr. Tuncay Ozel first introduced me to nanoscience and was an example of someone who was caring, successful, and productive. Dr. Jessie Ku shared an office with me, and the memory of our discussions (mostly random daily chatting), her encouragement, and our scientific collaborations will be never forgotten. I thank Dr. Bryan Mangelson for my first introduction to the lab, and for being a great example of a husband and father that one day I would like to become. I also thank

my officemates Jungsoo Park and Yuan Liu for being great and kind friends and providing an academic-friendly, quiet environment. It relaxed me.

I was very fortunate to have great collaboration opportunities inside and outside of the Mirkin Group: Dr. Sarah Park, Dr. Eileen Seo, Professor Mark Hersam, Dr. Jae-Hyeok Lee, Professor Jang, and Seung-Hoon Lee. I learned a great deal from each of them, and it has been fun to discuss with them random, raw, crude, unrefined ideas since they have been the people who took these ideas seriously and provided good feedback. I also enjoyed my collaborations with Dr. Seungkyu Lee, Dr. Fernando Castro, Dr. KunHo Yoon, and EunBi Oh. Although we did not produce manuscripts (yet), I really enjoyed my interactions with them and the team-based scientific pursuit.

Many thanks to my former and current labmates; there are too many to name them all, but the caring and positive learning environment they helped establish became a second home. The office staff, Pam Watson, Dr. Sarah Petrosko, Dr. Sara Rupich, Dr. Tanushri Sengupta, Dr. Caroline Ko, and Elizabeth Forest, invest so much effort to make certain the Mirkin Group runs smoothly, and I appreciate that. I am also grateful to have had access to the outstanding NU facilities and instruments. They are truly some of the best at any university in the world. Special thanks to the core facility managers in NUANCE, IMSERC, Keck, and QBIC, including Dr. Jinsong Wu, Dr. Ben Myers, Dr. Karl Hagglund, Dr. Eric Roth, Dr. Reiner Bleher, Dr. Xinqi Chen, and Dr. Keith MacRenaris. Also, I thank my friends I met at school and church, including Dr. Joohoon Kang, Dr. Ho-Il Ji, Dr. Kyoungdoc Kim, Dr. Woongkyu Lee, and many others, for helpful discussions and career advice.

I am extremely grateful for a continuous 5-year fellowship from the Kwanjeong Educational Foundation, which provided me with tremendous financial freedom. I also appreciate

the support of my research through the Office of Naval Research and the Air Force Office of Scientific Research.

Since I can remember, my parents have supported me and my decisions, and they trained me to be a creative and critical thinker. Without their encouragement, guidance, and prayers, this thesis would not be possible. Very special thanks to Aunt Youngsook Oh and my grandmother for their continuous support and prayers. I appreciate my sister, Dr. Rosy Oh, and brother-in-law, Dr. Jaewook Kim, for being members of our loving family, and all of my other family members for being supportive and teaching me about being a good person and life in general.

Last but not least, I thank my love, partner, and best friend, Yunhee Ji. She and our time together have been the remedy for Ph.D. stress and anxiety. She has endured much with me and provided encouragement with love.

List of Abbreviations

AAO: Anodic Aluminum Oxide

bcc: Body-Centered Cubic

CD: Circular Dichroism

DNA: Deoxyribose Nucleic Acid

fcc: Face-Centered Cubic

ICP-OES: Inductively Coupled Plasma Optical Emission Spectroscopy

MHA: 16-Mercaptohexadecanoic Acid

OD: Optical Density

OWL: On-Wire Lithography

PAE: Programmable Atom Equivalent

PB or PBS: Phosphate Buffer Solution

PDI: Polydispersity Index

PEG: Polyethylene Glycol

RD: Rhombic Dodecahedral Colloidal Single Crystals

SAM: Self-Assembled Monolayer

SAXS: Small-Angle X-ray Scattering

SDS: Sodium Dodecyl Sulfate

SEM: Scanning Electron Microscopy

STEM: Scanning Transmission Electron Microscopy

T_m : Melting Temperature

XPS: X-ray photoelectron Spectroscopy

Table of Contents

Abstract	3
Acknowledgements	5
List of Abbreviations	8
List of Figures	12
Chapter 1 Introduction.....	17
1.1 Objectives and Thesis Overview	18
1.2 Surface Modification and Nanoparticle Assembly with DNA.....	19
1.3 Colloidal Crystal Engineering with DNA	20
Chapter 2 DNA-Interconnected Molecular Transport Junctions and Selective Functionalization of Template-Synthesized Nanostructures	23
2.1 Summary	24
2.2 Background	24
2.2.1 Experimental Approaches towards Single-DNA Charge Transport	24
2.2.2 Molecular Transport Junctions by On-Wire Lithography	26
2.3 Selective Functionalization of Nanostructures and Directional Assembly.....	27
2.4 Charge Transport through DNA Strands	39
2.5 Charge Transport through DNA-Assembled Superlattices.....	41
2.6 Conclusions	45
2.7 Experimental	45
2.7.1 Materials and Instruments	45
2.7.2 Synthesis and Characterization of DNA	46
2.7.3 Electrochemical Synthesis of Nanorods.....	47
2.7.4 DNA Functionalization	48
2.7.5 DNA Loading Density on Spherical Particles.....	48
Chapter 3 Uniformity Control over Colloidal Single Crystal Formation	49
3.1 Summary	50
3.2 Background	51
3.3 Colloidal Crystallization and Density Layers	53

	10
3.4 Materials Selection for Density Layers.....	55
3.5 Results and Discussions	57
3.5.1 Observation of Colloidal Crystal Formation and Sedimentation	57
3.5.2 Size Uniformity	59
3.5.3 Shape Uniformity and Mobility in Viscous Solution.....	61
3.5.4 Effect of PAE Concentration on the Size Distribution of Microcrystals	63
3.5.5 Other PAE Systems	65
3.6 Conclusions	69
3.7 Experimental	70
3.7.1 Materials and Instruments	70
3.7.2 Preparation of PAEs and Their Hybridization	70
3.7.3 Preparation of PAE Microcrystals.....	71
3.7.4 Silica Encapsulation of Microcrystals.....	71
3.7.5 Characterization Methods	72
Chapter 4 Stabilization of DNA-Engineered Colloidal Crystals	74
4.1 Summary	75
4.2 Background	75
4.3 Results and Discussions	76
4.3.1 Stability in Pure Water and in the Solid State	76
4.3.2 Molecular Level Characterizations	79
4.3.3 Thermal and Chemical Stability.....	82
4.3.4 Reversibility	85
4.3.5 Other PAE Systems	87
4.4 Conclusions	87
4.5 Experimental	91
4.5.1 Materials.....	91
4.5.2 Functionalization of Nanoparticles with DNA.....	91
4.5.3 Superlattice Assembly.....	92
4.5.4 Preparation of PAE Crystals Stabilized with Ag ⁺	93
4.5.5 Silica Encapsulation of PAE Crystals	93
4.5.6 Characterization Methods	94

	11
Chapter 5 Metallo-DNA as Conductive Interconnects for Nanoparticles	96
5.1 Summary	97
5.2 Background	97
5.3 Results and Discussions	99
5.3.1 Conductivity of Ag-DNA Measured by Nanogap Devices.....	99
5.3.2 Conductivity of Ag-Mediated Colloidal Crystals	102
5.4 Conclusions	108
5.5 Experimental	108
5.5.1 Materials.....	108
5.5.2 Electrochemical Synthesis.....	109
Chapter 6 Conclusion and Future Remarks.....	111
References	116
Appendix A. Supplementary Images and Information for Chapter 2.....	131
Appendix B. Supplementary Figures for Chapter 3	139
Curriculum Vitae	142

List of Figures

- Figure 2.1.** Schematic diagrams of the selective functionalization process along with electron micrographs of the corresponding intermediate structures (cross-sectional SEM and STEM). (a) When Ni-Au-Ni trimer nanorods are synthesized in the nanopores, the ends of the Au segments are covered by Ni and the sides are protected by the AAO template. The masking materials can be orthogonally removed in stepwise fashion to perform MHA passivation or DNA functionalization on each face. (b) A similar strategy is applied to functionalize the inner cavity of Au nanorod dimers supported by a SiO₂ backbone. Before the gap material is removed, exposed surfaces can be modified with a MHA SAM. Etching of Ni, the gap material, is followed by the localized immobilization of DNA onto the newly opened gap. Scale bars: 50 nm. 29
- Figure 2.2.** Verification of the stability and functionality of DNA after exposure to chemicals. (a) Schemes of experiments used to test the stability of DNA on 20 nm Au spherical particles after chemical treatment (left) and respective digital photographs for visual inspection of their colloidal stability at each step (right). For all of the tested conditions, the particles remain well-suspended and visual analysis verifies the robustness of the DNA-Au nanoparticles. (b) Melting curves of the conjugates are monitored at their peak extinction wavelength ($\lambda=520$ nm) while decreasing the temperature at 0.1 °C·min⁻¹ increments from 65 to 25 °C. Narrow melting transitions (FWHM < 2 °C) indicate that DNA hybridization events still occur between nanoparticles after the chemical treatments. (c) Visible spectra of the samples below (25 °C) and above (65 °C) the melting temperature (45 °C)..... 32
- Figure 2.3.** Results of the MHA stability test, represented with the time-resolved current curves at a constant voltage of -900 mV during the electrodeposition of Ni, and the visual observation of Ni features by SEM. The suppressed currents at the initial deposition stages can be attributed to the presence of pinholes, and thus, intact SAM. The Ni segments overgrown through the pinholes are visualized by SEM. Scale bars equal to 500 nm. 34
- Figure 2.4.** (a) Schemes describing the mixtures of selectively functionalized rods/gaps and 60 nm spherical nanoparticles with complementary DNA. (1) Au nanorods with DNA on top and bottom bases. (2) Au nanorods with DNA functionalization on the sides. (3) Au dimers with DNA functionalization in the gap. (b) The colorimetric change at an elevated temperature was visually observable for all of the samples. (c) Melting curves of the three assemblies. (d) Vis-NIR spectra of the assemblies at 25 °C and 65 °C, in 0.5 M NaCl, 10 mM PB D₂O solution..... 36
- Figure 2.5.** Electron micrographs showing the DNA-directed assembly of spherical Au nanoparticles onto the selectively modified Au nanorods and nanogaps. The assemblies are shown in two ways: (a) assemblies in solution (dark-field STEM) and (b) on a substrate (SEM). (a) As expected, the spherical particles with complementary DNA strands are preferentially adsorbed onto the designated DNA-functionalized surfaces. (b) Asymmetric functionalization can be performed after the nanorods are cast onto a SiO₂ substrate. Stepwise assembly of 20 nm spherical particles (two layers) show clear discrimination among un-functionalized, non-selectively functionalized, and selectively functionalized (from left to right) nanorods/nanogaps. The assembled structures are embedded in

silica before imaging. Additional micrographs can be found in the Supporting Information. Scale bars: (a) 100 nm and (b) 200 nm. 37

Figure 2.6. (a) A SEM micrograph for an OWL-generated molecular transport junction bridged with DNA. Scale bar: 300 nm. (b) A STEM micrograph of a gapped nanowire in the same batch, showing ~10 nm gap spacing. Scaler bar: 50 nm. (c) The I-V characteristics measured and averaged from more than 10 devices for each sample (control: empty gaps). 40

Figure 2.7. (a) A schematic illustration for a new design where an OWL-generated nanogap is filled with DNA-assembled nanoparticle superlattices. (b) Even though the designed structure was formed as designed, the superlattices disassembled with a brief dip-washing in water. Thus, stabilization methods were employed to retain such structure in the gap for measurement, (c) silica encapsulation and (d) RuII-complex intercalation. All scale bars in (b-d) are 100 μm . (e) I-V characteristics of samples in (b-d). (f) The temporal responses of the current flow with constant voltage at 5 V. 42

Figure 2.8 Molecular structure of Ru^{II} intercalator complex. 43

Figure 3.1. Schematics and SEM images comparing the standard crystallization process of nanoparticle superlattices and a method to enhance uniformity. (a) Schematics of the current slow-cooling method where faceted rhombic dodecahedra may continue to grow as they sediment out of solution. (b) A representative scanning electron micrograph of rhombic dodecahedra synthesized by the current slow cooling method, where the sizes of the microcrystals vary, and coalescent crystals are frequently observed. (c) Schematics of proposed incorporation of a quenching sublayer to realize more uniform colloidal crystals. (d) A scanning electron micrograph of the microcrystals collected from the viscous sublayer shows improved uniformity in size and shape. e. Legends for the schematics, describing the PAE system used in this study: the blue and red circles represent A and B PAEs, respectively, which hybridize to each other by DNA anchor strands functionalized on particles and linker strands connecting PAEs together (**Table 3.6**). The number of modular units (n) controls the length of DNA linkers and lattice parameters of the resulting superlattices. Schemes are not drawn to scale. Purple rhombic dodecahedra represent the assembled microcrystals. Scale bars: 2 μm 54

Figure 3.2. (a) Density layers built with free PAE solution without linkers/saturated sucrose solution (left), microcrystal suspension/saturated sucrose solution (middle), and microcrystal suspension/saturated sucrose solution with 0.5 M NaCl (right). (b) Same PAE solutions mixed with linkers were added on top of different density gradient media on the bottom, saturated sucrose solution with NaCl, 10% dextran sulfate, 0.5 M NaCl in D₂O, 0.5 M KBr, 50% glycerol with NaCl, 2:3 diluted OptiprepTM with NaCl, 2:3 diluted Percoll[®] with NaCl, from left to right. The time stamps in (a) and (b) are in format of hh:mm:ss. 56

Figure 3.3. Control and quenched superlattices and their size distributions. (a) Optical images of the growth solution of PAEs at different stages of the slow cooling process. As the temperature is decreased at 0.01 $^{\circ}\text{C}\cdot\text{min}^{-1}$ through the melting temperature (~41 $^{\circ}\text{C}$), the PAEs assemble and sediment out of solution. (b) Radially averaged one-dimensional SAXS data (semi-logarithmic scale) confirms identical bcc lattice symmetry and lattice parameters (gray bars) for the control (black) and quenched (red) samples. (c) A representative scanning electron micrograph of the control sample (top) with its size distribution (middle, semi-logarithmic scale) and frequency of well-formed

superlattices (bottom). In the SEM images, the excess silica that forms during the encapsulation process can be observed around the rhombic dodecahedral microcrystals. The red line in the SEM image denotes a characteristic edge length, L . (d) The same information as in c for quenched samples. Scale bars: (a) 1 μm and (c, d) 1 μm 58

Figure 3.4. (a) Time-dependent extinction decay (at $T = 25\text{ }^\circ\text{C}$) of PAEs at $\lambda = 520\text{ nm}$ in a 0.5 M NaCl solution (black) and the same PAEs in 1:1 mixture of 0.5 M NaCl solution and 10% w/v dextran sulfate solution, i.e. 0.25 M NaCl and 5% w/v dextran sulfate (red). At $t = 0$, the linker strands are added so that the PAEs hybridize and are brought into proximity. (b) Same data plotted based upon Avrami theory. The linear fit (least squares method) at the earlier stage of each sample provides the values to calculate the rate constants of the decay. 62

Figure 3.5. Observation of the crystallization process (cooling rate $0.01\text{ }^\circ\text{C}\cdot\text{min}^{-1}$) with the dextran sulfate sublayer, and the concentrations of PAE in the growth solutions are varying from 2 nM to 20 nM, from left to right. 64

Figure 3.6. Microcrystal size distributions with varying lattice parameters. (a) Representative SEM images (left: control, right: quenched) and histogram of microcrystal edge lengths for 20 nm Au nanoparticles and $n = 0$ DNA (highest Au volume fraction sample). The excess silica from the encapsulation process can be observed around the microcrystals. The control sample is represented with gray bars, and the quenched samples with red bars in the histogram. (b, c) Same data as in (a) for $n = 1$ and 2 samples (decreasing Au volume fractions), respectively. All scale bars: 1 μm 66

Figure 3.7. Microcrystal size distributions for 10 nm Au, 40 nm Au, and 20 nm Ag nanoparticle assemblies. This quenching technique can be extended to DNA nanoparticle superlattices of varying nanoparticle sizes and compositions. The SEM micrographs of control (left) and quenched (middle) samples, and the histograms (right, gray: control, red: quenched) are represented for (a) 10 nm in diameter Au nanoparticles ($n = 0$ DNA), (b) 40 nm in diameter Au nanoparticles ($n = 2$ DNA), and (c) 20 nm in diameter Ag nanoparticles ($n = 1$ DNA). The excess silica from the encapsulation process can be observed around the microcrystals. All scale bars: 1 μm 68

Figure 4.1. (a) Schematic illustrating the synthesis of Ag^+ -stabilized PAE crystals (Ag-RDs). (b) In contrast to unmodified PAE crystals (RDs), which are stable in 0.5 M NaCl but dissociate upon resuspension in pure water, Ag-RDs are stable in water. (c) Radially-averaged one-dimensional SAXS patterns show lattice contraction upon the transformation into Ag-RDs (green) by transferring RDs (purple) to 0.5 M AgNO_3 . Ag-RDs are stable in unsalted water (grey). The first five peaks in each pattern were assigned to bcc lattices. (d) SEM micrographs (bottom: high resolution images of (110) facets from the corresponding squares) confirm the nondestructive contraction of RD to Ag-RD while maintaining crystallinity. Scale bars: (top) 500 nm and (bottom) 100 nm. 77

Figure 4.2. CD spectra of (a) A DNA (anchor + linker), B DNA, A DNA with Ag^+ , and B DNA with Ag^+ , and (b) mixture A DNA and B DNA with and without Ag^+ 80

Figure 4.3. (a) Schematic representation of a DNA strand (TCAG). Color representation is correlated to the peak fittings. (b) XPS spectra of RDs at N 1s core level peaks (left) and O 1s core level peaks (right) before Ag^+ -stabilization. (c) Same data for Ag-RDs. 81

Figure 4.4. (a) Melting curves (left) measured by variable-temperature UV-vis spectroscopy for RDs composed of 20 nm spherical Au nanoparticles suspended in 0.5 M NaCl (purple), and Ag-RDs in water (green). An inset SEM image confirms that the Ag-RDs maintain the Wulff shape after heating at 90 °C. SAXS patterns (right) for Ag-RDs in water do not change over the range of 20 – 90 °C. Scale bar: 1 μ m. (b) Ag-RDs can be transferred into variety of pH solutions (left), and acetone (pink), ethanol (blue), isopropyl alcohol (yellow, right) while maintaining their symmetry and lattice parameters. (c) SAXS patterns (top) and variable-temperature UV-vis spectroscopy (bottom) show the reverse reaction from Ag-RD to RD by transferring to 0.5 M NaCl solution. By comparison with NaClO₄, Cl⁻ is indeed responsible for the Ag⁺ elimination. 83

Figure 4.5. SEM images of Ag-RDs after being heated in the solid state under air for 5 h on Si wafers. The Ag-RDs remain intact up to 200 °C. Above 250 °C, the Ag-RDs start breaking and sintering. All scale bars: 1 μ m. 84

Figure 4.6. Change in lattice parameters as a function of (a) dehydration, (b) addition of 0.5 M NaCl, and (c) addition of 0.5 M NaClO₄ over three cycles. The lattice parameters were calculated from SAXS measurements. 86

Figure 4.7. Schematics for the unit cells, radially averaged one-dimensional SAXS patterns, and SEM images of untreated PAE crystals (purple) and Ag⁺-stabilized PAE crystals (green). (a) bcc superlattice of 20 nm nanoparticles with longer DNA linkers (**Table 4.3**), (b) fcc superlattice of 20 nm nanoparticles, and (c) bcc superlattice of 10 nm nanoparticles. Scale bars: 1 μ m and 100 nm for insets. 88

Figure 4.8. (a) Large-scale synthesis (> mg) of rhombic dodecahedral PAE crystals in uniform and pure powder form. (b) A magnified image of the highlighted area in panel a. Scale bars: (a) 5 μ m and (b) 500 nm. 89

Figure 5.1. (a) A representative SEM micrograph for gapped device. (b) I-V characteristics of a DNA-interconnected device with/without Ag⁺. Scale bar: 200 nm (c) Binned conductivity (log) data, without Ag⁺ (extraction by cysteine, left) and with Ag⁺ (right). (d) On-off switching of conductance by Ag⁺-mediation and extraction. (e) Arrhenius plot (Eqn 5.2) recorded by variable-temperature I-V measurement. 100

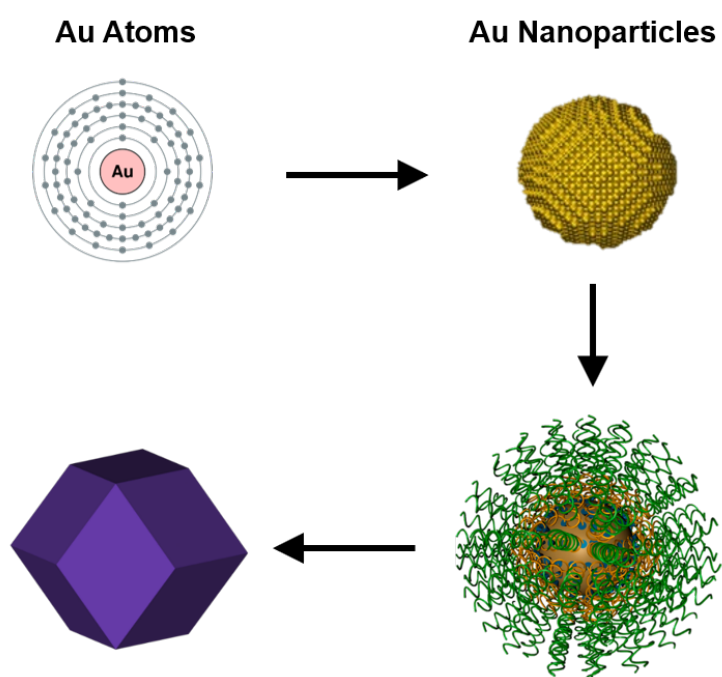
Figure 5.2. (a) A photograph of the pellet press used for the conductivity measurements of powder samples in this study. (b) I-V characteristics for (1) Ag⁺-mediated crystals without PEG spacers in DNA, (2) unmetallized PAE crystals, and (3) Ag⁺-mediated crystals with PEG spacers in DNA (**Table 4.4**). 103

Figure 5.3. (a) Schematic diagram for bcc PAE crystal lattices with increasing interparticle distance (DNA length), n = 0, 1, and 2 (**Table 5.1**) from top to bottom, respectively. The schemes were drawn to scale with the values from SAXS. (b) The measured conductivity plotted versus the interparticle distance for each sample. 106

Figure 5.4. (a) Schematic diagram for bcc PAE crystal lattices with increasing core diameters, 10 nm, 40 nm, and 80 nm from left to right. The schemes were drawn to scale with reference values from SAXS. (b) I-V characteristics for all of the samples and (c) conductivity plotted versus the core

	16
diameters of each sample. The shaded area in (c) indicates the upper measurement limit of our setup mainly due to contact resistance.	107
Figure 6.1. (a) Schematic diagrams and respective electron micrographs for selective functionalization of template-synthesized nanoring surfaces, side barrels (top), top and bottom ends (middle), and inner faces (bottom). (b) Assembly of spherical nanoparticles selectively adsorbed and bound into the center of a nanoring. Scale bar: 50 nm.....	114
Figure A.1. Additional STEM micrographs for the directed assemblies of 20 nm Au nanoparticles onto the selectively functionalized barrels of Au nanorods.	131
Figure A.2. Additional STEM micrographs for the directed assemblies of 20 nm Au nanoparticles onto the selectively functionalized bases of Au nanorods.	132
Figure A.3. Additional STEM micrographs for the directed assemblies of 20 nm Au nanoparticles onto the selectively functionalized gaps of Au nanorod dimers.	133
Figure A.4. Additional STEM micrographs for the directed assemblies of 60 nm Au nanoparticles onto the selectively functionalized barrels of Au nanorods.	134
Figure A.5. Additional STEM micrographs for the directed assemblies of 60 nm Au nanoparticles onto the selectively functionalized bases of Au nanorods.	135
Figure A.6. Additional SEM micrographs for the substrate assemblies of 20 nm Au nanoparticles onto the DNA-functionalized Au nanorod: (a) without functionalization, (b) non-selective functionalization, and (c) selectively functionalization on the bases.....	136
Figure A.7. Additional SEM micrographs for the substrate assemblies of 20 nm Au nanoparticles onto the DNA-functionalized Au nanorod dimers: (a) without functionalization, (b) non-selective functionalization, and (c) selectively functionalization in the gap.....	137
Figure B.1. Supplementary SEM micrographs of PAE colloidal crystals (20 nm Au nanoparticles and $n = 1$ DNA linkers) assembled without quenching sublayer. The colloidal crystals have been false colored to distinguish from the silica debris. All scale bars: 1 μm	139
Figure B.2. Optical micrographs showing the wide-angle view of assembled microcrystals with 20 nm Au nanoparticles and $n = 1$ DNA linkers, in (a) control and (b) quenched samples. Scale bars: 10 μm	140
Figure B.3. Radially averaged one-dimensional SAXS patterns showing the same diffraction patterns (bcc) but different lattice parameters for the PAE systems studied. The parameters are tabulated in Table 3.7	141

Chapter 1 Introduction



1.1 Objectives and Thesis Overview

Most of the unique properties of nanomaterials, whose size regime sits between the atomic and microscopic scale, arise from their high surface-to-bulk ratio. The surface of the nanomaterial, along with composition, size, and shape, generates desirable materials characteristics. The surface properties play an especially important role in modulating the assembly of nanoparticles into superstructures, a process that is highly dependent on the surface charge, polarity, and specific interactions between surface ligands.¹⁻⁸ Among the strategies for assembling nanoparticles into larger structures, DNA-mediated methods,¹⁻² pioneered by Mirkin, are a powerful approach where the hybridization of surface-immobilized DNA can act as nanoparticle “bonds.” Since DNA hybridization is highly specific with the formation of Watson-Crick base pairing (Adenosine (A) – Thymidine (T) and Guanosine (G) – Cytidine (C)), one can deliberately program the selectivity, strength, and length of these nanoparticle bonds through the sequence design. The nanoparticle assemblies in this manner can be regarded as analogues of atomic arrangement but with programmable bonds, and from this analogy, the building blocks, DNA-functionalized nanoparticles, have been frequently termed as programmable atom equivalents (PAEs).

Over the past decade, surface-immobilized DNA has been used to bring colloidal nanoparticles into proximity¹ and as scaffolds for assembling nanoparticles of a broad range of sizes, shapes, and compositions into highly ordered colloidal crystals.² In colloidal crystals, the physical properties of the individual building blocks are combined to exhibit a collective behavior not observed in the constituent components. Although colloidal crystals engineered with DNA have promising optical applications due to their plasmonic and photonic properties;⁹⁻¹³ several significant challenges in DNA-assembled colloidal crystal engineering must be solved before they can be applied more broadly to photocatalysis, electronics, and others.

My dissertation will identify some of these challenges and discuss possible solutions to each of them. Chapter 2 defines the problem of charge transport between nanoparticles through DNA, and describes our attempts to measure the conductivity of DNA using nanogap devices. Chapter 3 discusses the polydispersity in microscopic geometries of colloidal single crystals, which plays a huge role in the structure-function relationship, and introduces a new method to enhance the uniformity based on density layers to quench overgrowth and coalescence. In Chapter 4, the structural stability of the colloidal crystals, which is sensitive to changes in temperature, solvents, and others, is substantially improved by the formation of metallo-DNA complex compounds. Chapter 5 examines the electrical conductivities of the metallo-DNA and metal-stabilized colloidal crystals and the possibility for the metallo-DNA to potentially become conductive nanoparticle bonds.

1.2 Surface Modification and Nanoparticle Assembly with DNA

In 1996, Mirkin and coworkers¹ introduced polymeric aggregates of Au nanoparticles using the hybridization of surface-immobilized DNA strands. In this assembly system, two different types of non-complementary DNA strands terminated with thiol in the 3'-ends were functionalized onto Au particles using well-established Au-thiol conjugation chemistry.¹⁴ Upon the mixture of the DNA-functionalized nanoparticles with the "linker" strands, the DNA hybridization events connect nanoparticles together and initiate nanoparticle aggregation. The sequence design for "linker" strands is composed of two major parts: one part to hybridize with the surface immobilized strands and the "sticky end" that can hybridize with other linker strands of neighboring entities. The aggregation can be observed by the red-shifts of the optical extinction peak which reveals red-to-blue color change of the colloid due to the plasmonic coupling between

nanoparticles. As described in the next section, DNA-mediated nanoparticle assembly that utilizes this design has developed over the past two decades to employ the hybridization specificity, strength, and length, all of which are controllable with great precision by the sequence design, to realize highly ordered nanoparticle superstructures with programmable interparticle distance, bond strength, and crystal symmetries.

1.3 Colloidal Crystal Engineering with DNA

There are a handful methodologies for constructing ordered nanoparticle superlattices and colloidal crystals using surface charge, size, and hydrophilic/hydrophobic interactions.^{3, 5, 7-8} Nearly all of these characteristics used for assembly are inevitably dependent on the composition, size, and shape of the core; therefore, the core dictates the resulting crystal lattice structure and symmetry. One of the most advantageous features of DNA-mediated colloidal crystal engineering is that assembly in this fashion can be isolated from the core composition and solely controlled by the surface-immobilized DNA design. Specifically, Park and coworkers¹⁵ reported the construction of body-centered cubic (bcc) and face-centered cubic (fcc) lattices composed of identical spherical Au nanoparticles, and the lattice symmetry was determined solely by the complementarity of the DNA-functionalized nanoparticles, which have subsequently become known as PAEs. Later, Macfarlane and coworkers¹⁶ developed design rules for nanoparticle superlattice formation based on the hydrodynamic radius of PAEs and the number of linker strands binding to the cores in addition to the complementarity. Since then, over 40 different crystal symmetries, including unprecedented quasicrystal structures,¹⁷ made of DNA-functionalized colloidal particles of various compositions^{13, 18-20} have been reported, with lattice parameters ranging from ~20 nm to few microns, that utilize anisotropic building blocks,²¹⁻²³ preassembled

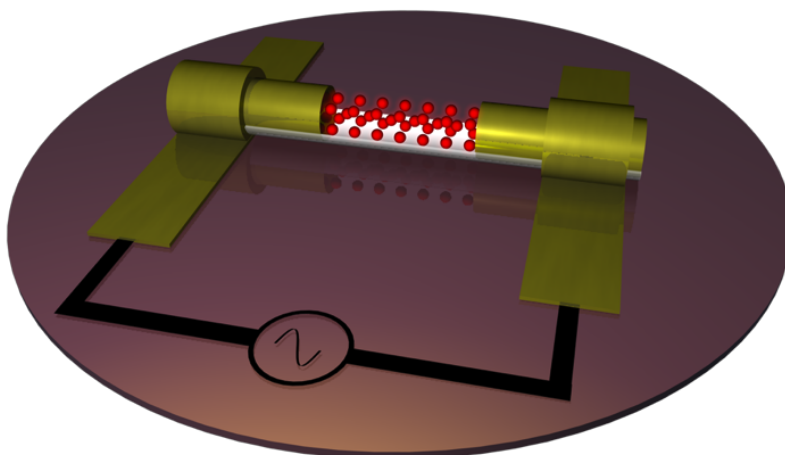
clusters,²⁴ hollow PAEs,²⁵ and DNA origami structures.²⁶ As mentioned, the assembly dynamics in this system is independent of the core compositions, and superlattice formation with building blocks other than Au nanoparticles have been demonstrated.¹⁸

Furthermore, based on the fact that DNA-mediated nanoparticle assembly exhibits sharp melting transition which is comparable to liquid-to-solid phase transition, Auyeung and coworkers²⁷ reported the formation of microscale colloidal single crystals shaped in thermodynamically favored Wulff polyhedra using a slow cooling process. For example, the crystalline form of PAE assembly with bcc lattice symmetry will eventually form a rhombic dodecahedral crystal habit exposing (110) facets. In addition, colloidal single crystals shaped in cubes, octahedra, and rhombic dodecahedra were realized by the use of anisotropic building blocks,²⁸ and Seo and coworkers²⁹ revealed hexagonal prisms with AlB₂ lattices as a kinetic product of crystallization process.

In the meantime, substrate-assisted methods for DNA-engineered superlattice formation have been developed as a counterpart to solution-crystallized superlattices.³⁰ In this approach, a substrate composed of a thin Au film is functionalized with DNA using Au-thiol chemistry. Then, a layer of PAEs is attached via DNA hybridization with the substrate-immobilized DNA. Additional PAE layers are built by iteratively introducing PAEs with DNA sequences that are complementary to the proceeding layer, thus, enabling layer-by-layer assembly of polycrystalline bcc lattices. These two-dimensional nanoparticle superlattice sheets can also be synthesized in millimeter scale, delaminated from the substrate, and conformally transferred to other substances.³¹ By using prepatterned posts, instead of a uniform Au layer, for assembly, one can control crystal domain sizes and orientations, allowing one to realize two-dimensional single crystal sheets and patterns with precise control over nano- and microscale geometries.³²⁻³³ Recently,

based upon the aforementioned advantages and extensive development of DNA-mediated superlattice formation, the studies on the characteristics in materials perspectives and attempts for practical applications have been carried out especially in the optical properties.^{9-11, 13, 34}

Chapter 2 DNA-Interconnected Molecular Transport Junctions and Selective Functionalization of Template-Synthesized Nanostructures



Portions of this chapter have been published³⁵ in *Journal of the American Chemical Society*, **2017**, *139* (20), 6831.
Co-authors of this work: Jessie C. Ku, Tuncay Ozel, Chad A. Mirkin
Copyright 2019 American Chemical Society

2.1 Summary

While the efficacy of charge transport through native DNA duplex is rather disputable, the possibilities it will bring to the nanoparticle and molecular device society is beyond our depth. In this chapter, our attempts to build nanogap junction devices and results from the measurement of electrical conductivity through DNA and DNA-interconnected superlattices are introduced by means of templated electrochemical synthesis. The largest portion of this chapter is allocated to the asymmetric functionalization of template-synthesized nanostructures, which is a key part of the successful fabrication of molecule-bridged nanogaps. It describes a novel approach for the selective chemical functionalization and localized assembly of one-dimensional nanostructures (rods and gaps), based upon the systematic activation (DNA functionalization) and passivation (self-assembled monolayers) of specific surface sites through the use of orthogonal chemical reactions on electrochemically grown metal nanorod arrays in porous anodic aluminum oxide (AAO) templates. The ability to orthogonally functionalize the ends or the side of a nanorod, as well as the gaps between two rods, with different DNA strands allows one to synthesize nanostructure assemblies that would be difficult to realize any other way and that could ultimately be utilized for making a wide variety of device architectures.

2.2 Background

2.2.1 Experimental Approaches towards Single-DNA Charge Transport

First suggested in early 1960s,³⁶ the conductivity of DNA has drawn an enormous attention (and controversy) in the molecular electronics field due to the great potential represented by the flexibility, versatility, and programmability, seemingly ideal for molecular wires as long as it can transport charges effectively. Especially during the past two decades, based on technological

advances in experimental tools for building molecular junctions, researchers have utilized different strategies to build single- (or few-) DNA-bridged junctions to directly measure the conductance and I-V behavior. Before direct measurements with metal electrodes, the initial attempts were made based upon the incorporation of photoactive donor and acceptor molecules, which are conjugated organic compounds³⁷ or metal complexes,³⁸ in the two ends of DNA strands. In such systems, the charge transport behaviors were indirectly probed with changes in the optical properties (transient absorption/emission) of the acceptor probes as response to the photoexcitation of the donor molecules and diffusion of photoelectrons. More direct measurements with two-point-probe configurations, where the applied voltage between the two electrodes is manually controlled and the only current paths is through DNA strands, were carried out from the late 1990s. Fink and Schönenberger³⁹ used low-energy electron point source microscope equipped with a mobile electrical probe, and the resistance of a long DNA bunch (multiple strands, sub-1- μm) was measured to be few $\text{M}\Omega$ range. Dekker and coworkers⁴⁰ built gapped Pt nanoelectrodes using e-beam lithography and the sub-10 nm gap was bridged by (supposedly single or few) DNA strands, whose resistance was in $\text{G}\Omega$ range. Several methods were attempted and reported around that time, but the results were rather confusing among themselves, giving conductance values corresponding to from insulators⁴¹ to superconductors,⁴² mainly due to the lack of control experiments and different surrounding experimental conditions that possibly affected the structure of DNA.

In 2003, Tao and coworkers developed a scanning-probe-microscopy- (SPM-) based method to build a molecular junction between the substrate and the probe that can be repeatedly connected and broken.⁴³ Using this method, the conductance across the junction can be measured and statistically analyzed to generate reproducible conductance data. The SPM-break-junction technique was then used to examine the conductance through short DNA duplexes, DNA with

different conformations, mismatched DNA, and many others.⁴⁴⁻⁴⁸ In 2007, enabled by a wide use of carbon nanotubes and the development of e-beam lithography,⁴⁹ Barton and coworkers used nanogaps formed by lithographically etched carbon nanotubes. The open gap was bridged by an amine-terminated DNA duplex (claimed based on the narrow width of electric leads) to be electrically examined.⁵⁰ A recent study used conductive atomic force microscopy to measure long-range (tens of nanometers) charge transport through G-quadruplex DNA strands as well as DNA duplexes as a control.⁵¹ With these advances in measurement technology, the conductivity of “natural” DNA is approaching to be defined, but some of the recent results have been still incoherent to the mainstream arguments and the values are somewhat low to become effective molecular wires to connect nanoparticles for energy transports and communications.

2.2.2 Molecular Transport Junctions by On-Wire Lithography

Previously in our group, a fabrication method for molecular junctions has been developed based upon the formation of nanogaps by on-wire lithography (OWL).⁵²⁻⁵⁵ In this fabrication methodology, templated electrochemical growth through AAO membranes is used for the synthesis of multisegment nanowires, specifically, with two Au segments separated by a few-nanometer-scale Ni layer. After the synthesis, these nanowires are released into solution by dissolving the template, and spread onto a substrate by dropcast or vacuum filtration. Then, onto the one side of the nanowires, thin layer of insulating material (typically SiO₂) is deposited via physical vapor deposition. The nanowires are resuspended in solution by ultrasonication. The sacrificial Ni layers are then selectively removed by an appropriate etchant (typically FeCl₃ or H₃PO₄ solution), while the thin insulating layer holds the two Au nanowires together. Then, all the exposed Au surfaces, including the gaps between Au dimers, are functionalized with molecules of

interest, typically by means of Au-thiol bonds. The functionalized Au dimers are cast onto a SiO₂ chips with prepatterned Au electrodes. Each of the Au dimer are electrically connected to an electrode by e-beam lithography. Finally, the nanogap junctions bridged by the molecules can be electrically characterized. Using this method, electrical properties of molecular wires have been tested and some interesting quantum mechanical phenomena were discovered.^{54, 56-60} This method is particularly advantageous due to the high throughput synthesis of the nanogaps where the gap spacing can be tailored with a nanometer precision, and electrode materials can be chosen from a wide variety of materials library for electrochemical plating techniques.

However, this method may not be suitable for designing electrical measurement of molecules like DNA whose conformations and hybridization is highly influenced by the environment such as the salt concentration and hydration state. The formations of Watson-Crick base pairing and DNA duplexes is not guaranteed to retain in the solid state and requires the measurement to be performed in the salt solution. If the entire or part of the circuitry is exposed to the DNA-hybridizing media (basically salt solution), the measurement will be intensely disturbed by leakage current through the media. This motivated the development of selective activation and passivation of template-synthesized nanostructures, especially the nanogap structures.

2.3 Selective Functionalization of Nanostructures and Directional Assembly

The surface modification of nanoparticles provides a way to program their interactions with neighboring entities.⁶¹ Oligonucleotides are the best example of this programmability, where a 17-mer, for example, provides $\sim 4^{17}$ unique combinations of bases, many of which are perfectly orthogonal in their recognition properties for complementary oligonucleotides. This observation has been utilized heavily to create probes for measuring oligonucleotide concentration,⁶²⁻⁶³

therapeutic constructs for gene regulation⁶⁴ and sequence-specific immuno-modulation strategies,⁶⁵ and even for creating higher-order assemblies from patterned surfaces or nanoparticle building blocks preferentially functionalized with oligonucleotides at discrete geometric sites.^{2, 66}

A long-standing challenge has been the selective functionalization of anisotropic structures with programmable ligands at desired locations. For rods and prisms, researchers have explored kinetic control approaches,⁶⁷⁻⁶⁸ anisotropic zeta potentials,⁶⁹ and reactivity differences on different geometric faces⁷⁰⁻⁷² to selectively functionalize them with different chemical entities. However, the similarity in chemistry makes it virtually impossible to modify them with different chemical structures. Alternatively, one can use nanostructures made of different compositions and selectively modify them based upon such differences.⁷³⁻⁸¹ Some researchers have post-synthetically masked certain faces of the nanostructure, while exposing others, to effect surface modification at designated sites.⁸²⁻⁸⁴ This section describes a new method that relies on the electrochemical synthesis of nanorods in AAO templates, a method pioneered by Martin and Moskovits,⁸⁵⁻⁸⁶ and our OWL,⁵² to make nanorod architectures with oligonucleotides exclusively placed on the two ends, the cylindrical surface of the rod, or in the gaps between rods (**Figure 2.1**). This method relies on the ability to selectively mask regions of the rod during its synthesis within the template and is capable of selective functionalization of billions of rods with desired oligonucleotides at pre-designated geometric locations on the rods in parallel. Although we explore the capabilities of this new technique with rods made only of Au, given the widespread use of template-mediated syntheses for metals,^{85, 87-88} semiconductors,⁸⁹⁻⁹² conducting polymers,^{91, 93-94} and the ability to construct various geometric shapes including non-circular prisms and coaxial structures,⁹⁵⁻⁹⁶ this approach is likely extendible to other classes of materials with different shapes.

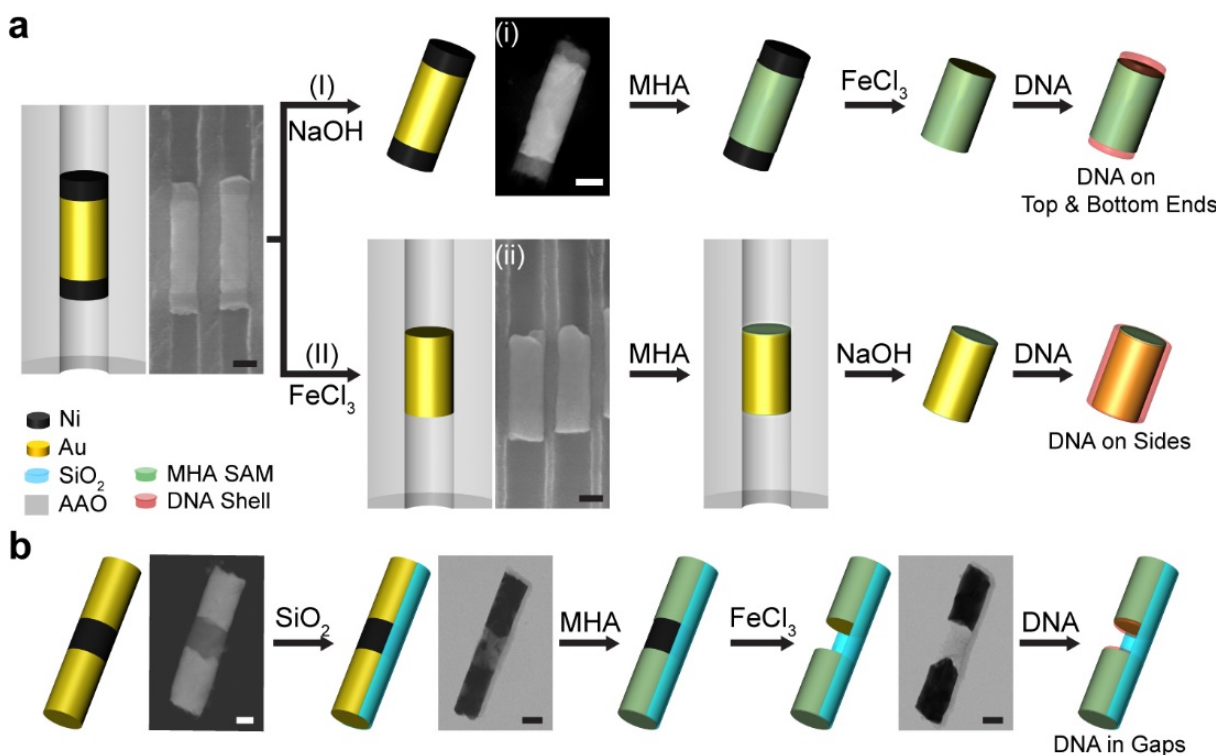


Figure 2.1. Schematic diagrams of the selective functionalization process along with electron micrographs of the corresponding intermediate structures (cross-sectional SEM and STEM). (a) When Ni-Au-Ni trimer nanorods are synthesized in the nanopores, the ends of the Au segments are covered by Ni and the sides are protected by the AAO template. The masking materials can be orthogonally removed in stepwise fashion to perform MHA passivation or DNA functionalization on each face. (b) A similar strategy is applied to functionalize the inner cavity of Au nanorod dimers supported by a SiO₂ backbone. Before the gap material is removed, exposed surfaces can be modified with a MHA SAM. Etching of Ni, the gap material, is followed by the localized immobilization of DNA onto the newly opened gap. Scale bars: 50 nm.

In a typical experiment, Au nanorods were synthesized within a porous AAO template using a conventional three-electrode electrochemical configuration.⁵⁵ The pore walls of the template isolated the cylindrical surface of the nanorods from the top and bottom faces (ends) (**Figure 2.1a**).⁹⁷ Sacrificial Ni segments can be electrochemically plated on these ends before and after the deposition of the Au segments. Because of the contrasting classes of materials capping the ends and the barrel sides (a metal and an oxide, respectively), orthogonal chemistry could be applied to selectively address each surface. This process could be performed in two ways: (I) dissolving the template or (II) removing the metal capping segments (**Figure 2.1a**). In (I), the AAO template was dissolved in a 3 M aqueous NaOH for 10 min, releasing the Ni-Au-Ni nanorods into solution and exposing the barrel of the Au rods. In (II), the sacrificial Ni segments were etched by soaking the template with nanorods in 3% FeCl₃ (aq) for 10 min, exposing their top and bottom faces. Notably, the etchants were chosen so that the target material could be removed orthogonally, leaving the Au rods and the other masks undamaged. The concentrated basic solution and ferric ions specifically removed the AAO membrane (i) and the Ni caps (ii), respectively (**Figure 2.1a**). The selectively exposed portions of the Au nanorod faces were then chemically passivated with a self-assembled monolayer (SAM) by immersing them in an ethanolic solution of 10 mM 16-mercaptohexadecanoic acid (MHA) for 12 h. After sequential rinsing with 90% ethanol and water, the remaining masks (Ni or AAO) were removed with their respective etchants. The resulting structures were washed three times with water, and the newly exposed Au surfaces were modified with 3'-propylthiol-terminated DNA (**Table 2.2**) by incubating the nanorods in an aqueous 10 mM phosphate buffer solution (PBS, pH 7.6) containing ~10 μM DNA and 1.0 M NaCl for 12 h, thus chemically activating designated sites on the nanorods.

A similar approach was used to selectively address the gap between the Au dimers prepared by OWL (**Figure 2.1b**).^{52, 55} Au dimers with a Ni segment in the middle were synthesized using electrochemistry and dispersed by dissolving the template in 3 M NaOH (aq). These tri-segmented nanorods were then transferred onto an empty AAO template via vacuum filtration.⁵⁵ A 7 nm thick SiO₂ layer was deposited on the template using an electron beam evaporator to cover the upper half of the nanorods, and they were then dispersed in ethanol via sonication. The uncovered sides of the Au nanorods were chemically passivated by immersing them in a 10 mM ethanolic MHA, and an MHA SAM formed on the exposed Au surface. Then, the sacrificial Ni segment was etched with 3% FeCl₃ (aq) while the SiO₂ sheath maintained the position of the Au segments. Finally, the pristine gap faces were functionalized with DNA as described above.

In this process, the first chemical adsorbate on the Au surface, either DNA or MHA, was exposed to a variety of chemicals during the removal of the template and sacrificial capping materials. To examine the effects of the chemicals on the ligands, we evaluated the state of the adsorbates under various treatments (3 M NaOH (aq), 3% FeCl₃ (aq), neat acetone, or neat ethanol, **Figure 2.2a**) with pure water as a control. In a typical experiment, 20 nm Au nanoparticles were functionalized with 3'-propylthiol-modified DNA strands (**Table 2.2**).⁹⁸ After washing with water, they were treated with each solution for 1 h at room temperature, considerably longer than the time required for complete removal of the masking materials. After thorough washing with water, aliquots were taken from each sample to measure the DNA surface coverage via an Oligreen® assay and inductively coupled plasma optical emission spectroscopy (ICP-OES, Experimental section for details). Importantly, significant changes in the DNA loadings were not observed after any of the chemical treatments (**Table 2.1**).

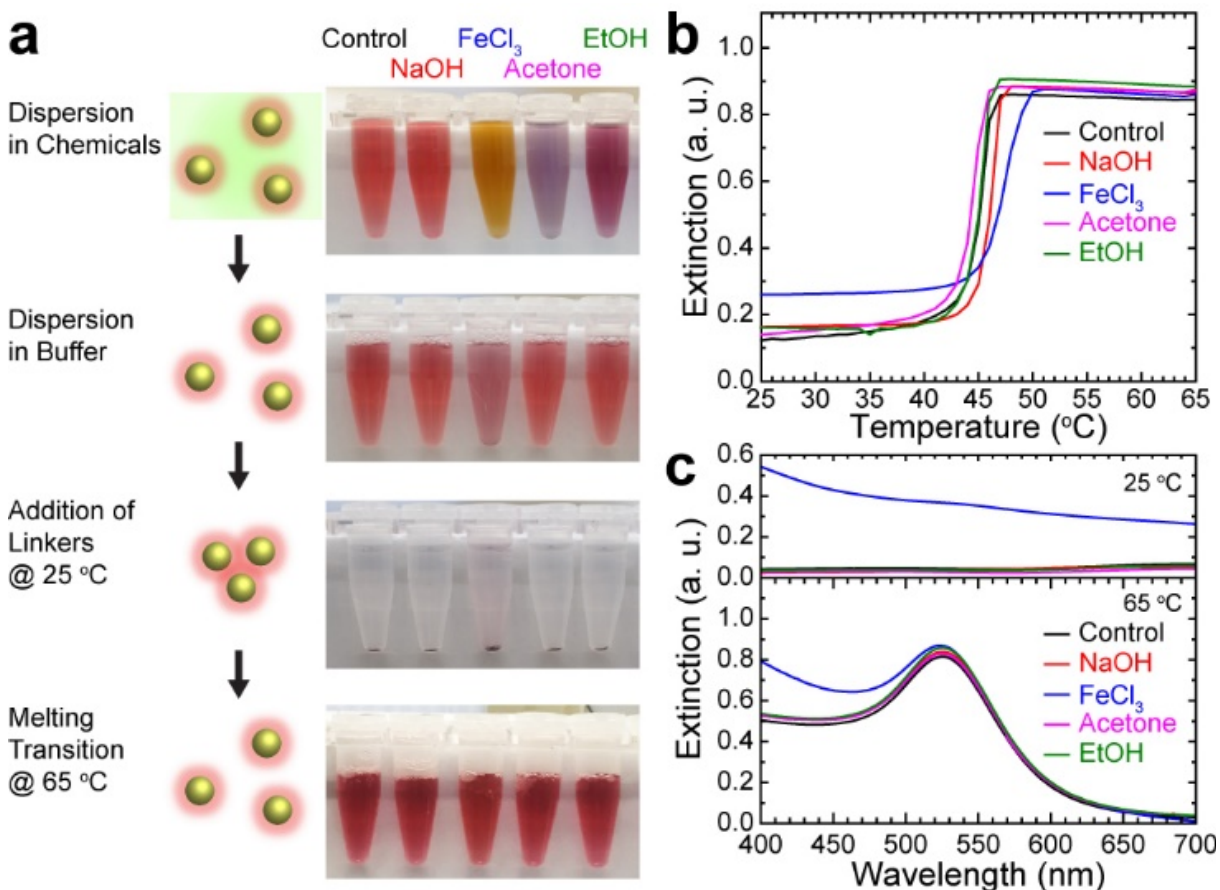


Figure 2.2. Verification of the stability and functionality of DNA after exposure to chemicals. (a) Schemes of experiments used to test the stability of DNA on 20 nm Au spherical particles after chemical treatment (left) and respective digital photographs for visual inspection of their colloidal stability at each step (right). For all of the tested conditions, the particles remain well-suspended and visual analysis verifies the robustness of the DNA-Au nanoparticles. (b) Melting curves of the conjugates are monitored at their peak extinction wavelength ($\lambda=520$ nm) while decreasing the temperature at 0.1 °C \cdot min⁻¹ increments from 65 to 25 °C. Narrow melting transitions (FWHM < 2 °C) indicate that DNA hybridization events still occur between nanoparticles after the chemical treatments. (c) Visible spectra of the samples below (25 °C) and above (65 °C) the melting temperature (45 °C).

Table 2.1. DNA loading density after treating the DNA-Au nanoparticle conjugates with water (control), 3 M NaOH, 3% FeCl₃, acetone, ethanol, or 10 mM MHA solution.

Control	NaOH	FeCl₃	Acetone	Ethanol	MHA
342 ± 17	324 ± 16	319 ± 18	334 ± 16	324 ± 16	153 ± 10

Further, we analyzed the hybridization of the DNA-modified particles with their complementary DNA in 0.5 M aqueous NaCl (a). By introducing complementary DNA linkers (**Table 2.2**, 175 linker strands per particle), one can induce hybridization events observable with the naked eye and UV-vis spectroscopy; when the particles hybridize and are brought into close proximity, their localized surface plasmon resonance at 520 nm red-shifts, resulting in a red-to-blue color change.¹ This behavior was observed for all samples and was reversible at elevated temperatures (**Figure 2.2**), indicating that the DNA on the particle surface was not damaged or chemically modified. The efficacy of backfilling with an MHA SAM was tested by treating the DNA-functionalized nanoparticles with 10 mM ethanolic MHA. The MHA rapidly removed the adsorbed DNA,⁹⁹ emphasizing the importance of effecting SAM formation prior to DNA functionalization.

The MHA SAM can serve as an effective passivation layer only if it remains intact under the chemical conditions used for the selective removal of the capping materials. The chemical resistance of the MHA SAM to 3 M NaOH, 3% FeCl₃, or acetone was tested with substrate-based experiments by attempting electrochemical deposition of Ni on MHA-modified Au thin films (**Figure 2.3**). In this experiment, Au thin films (50 nm) on Si with a Cr adhesion layer (2 nm) were immersed in a 10 mM ethanolic MHA solution for 12 h. The samples were rinsed with ethanol and immersed in each solution (water as a control, 3 M NaOH, 3% FeCl₃, or acetone) for 10 min. As a positive control, SAM was damaged with a 5 min O₂ plasma cleaning. Each of these samples was rinsed with water and used as a working electrode in Ni electrodeposition. Importantly, all of

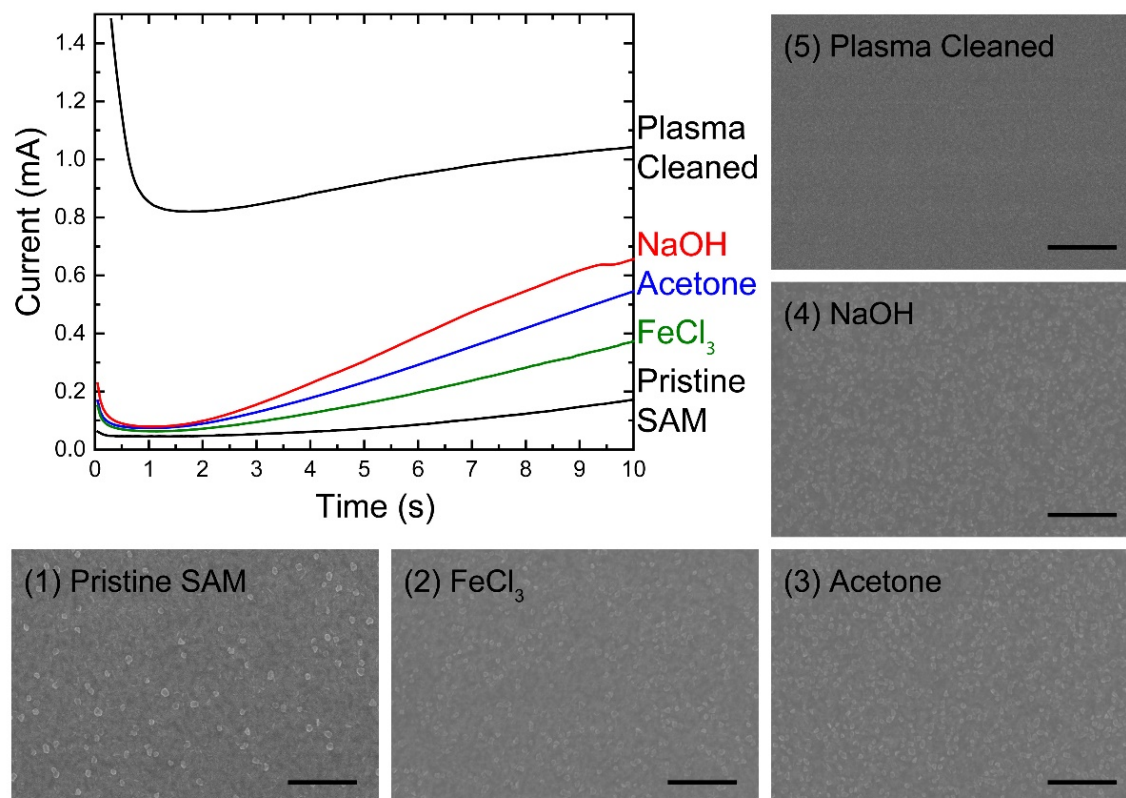


Figure 2.3. Results of the MHA stability test, represented with the time-resolved current curves at a constant voltage of -900 mV during the electrodeposition of Ni, and the visual observation of Ni features by SEM. The suppressed currents at the initial deposition stages can be attributed to the presence of pinholes, and thus, intact SAM. The Ni segments overgrown through the pinholes are visualized by SEM. Scale bars equal to 500 nm.

the samples exhibited a low initial current as explained in the literature¹⁰⁰ and consistent with intact SAM (**Figure 2.3**). Eventually, the current gradually increased as deposited Ni started to fill in pinholes in the MHA layer, as evidenced by electron microscopy (**Figure 2.3**). Taken together, these data are consistent with a conclusion that the MHA SAM remains intact after being treated with the etching solutions. This substantiated our claim that the aforementioned chemicals did not alter the surface coverage of MHA on Au.

The selective functionalization of nanostructures with DNA provides the ability to control subsequent assembly events in a directional and programmable manner. As a proof-of-concept demonstration and to further test the selective functionalization of the rods with DNA, we studied their hybridization with complementary spherical DNA-Au nanoparticle conjugates in 0.5 M NaCl. Upon mixing, the rods (or gaps) and spherical particles assembled and settled over time. A narrow melting transition measured by temperature-dependent UV-vis spectrometry (FWHM ~ 2 °C, **Figure 2.4**) confirmed that the assemblies were indeed DNA-mediated. Using literature procedures,¹⁰¹ the assemblies were encapsulated in silica to lock the position of the assemblies in the solid state for scanning transmission electron microscopy (STEM). One can clearly see that the spherical particles hybridize selectively to the regions of the rods with complementary DNA (sides, ends, and gaps, **Figure 2.5a**, additional images in **Appendix A**).

When the assembly process is carried out on a substrate, the nanorods can be functionalized in a site-specific manner with multiple layers of spherical particles in stepwise fashion, much like supramolecular crystals grown and evolved from a macroscopic flat substrate.³⁰ After synthesis and dispersion in ethanol, Ni-Au-Ni (Au rods) or Au-Ni-Au (Au dimers with a gap) tri-segmented rods with diameters of 300 nm were dropcast onto 7.5 mm by 15 mm Si substrates with a 500 nm thick thermal oxide layer. The wafers were then submerged in 10 mM ethanolic MHA for 12 h at

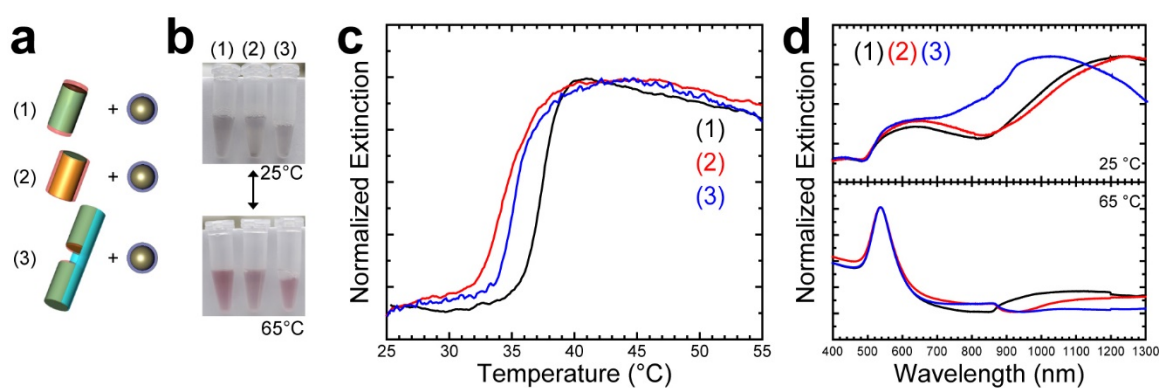


Figure 2.4. (a) Schemes describing the mixtures of selectively functionalized rods/gaps and 60 nm spherical nanoparticles with complementary DNA. (1) Au nanorods with DNA on top and bottom bases. (2) Au nanorods with DNA functionalization on the sides. (3) Au dimers with DNA functionalization in the gap. (b) The colorimetric change at an elevated temperature was visually observable for all of the samples. (c) Melting curves of the three assemblies. (d) Vis-NIR spectra of the assemblies at 25 °C and 65 °C, in 0.5 M NaCl, 10 mM PB D₂O solution.

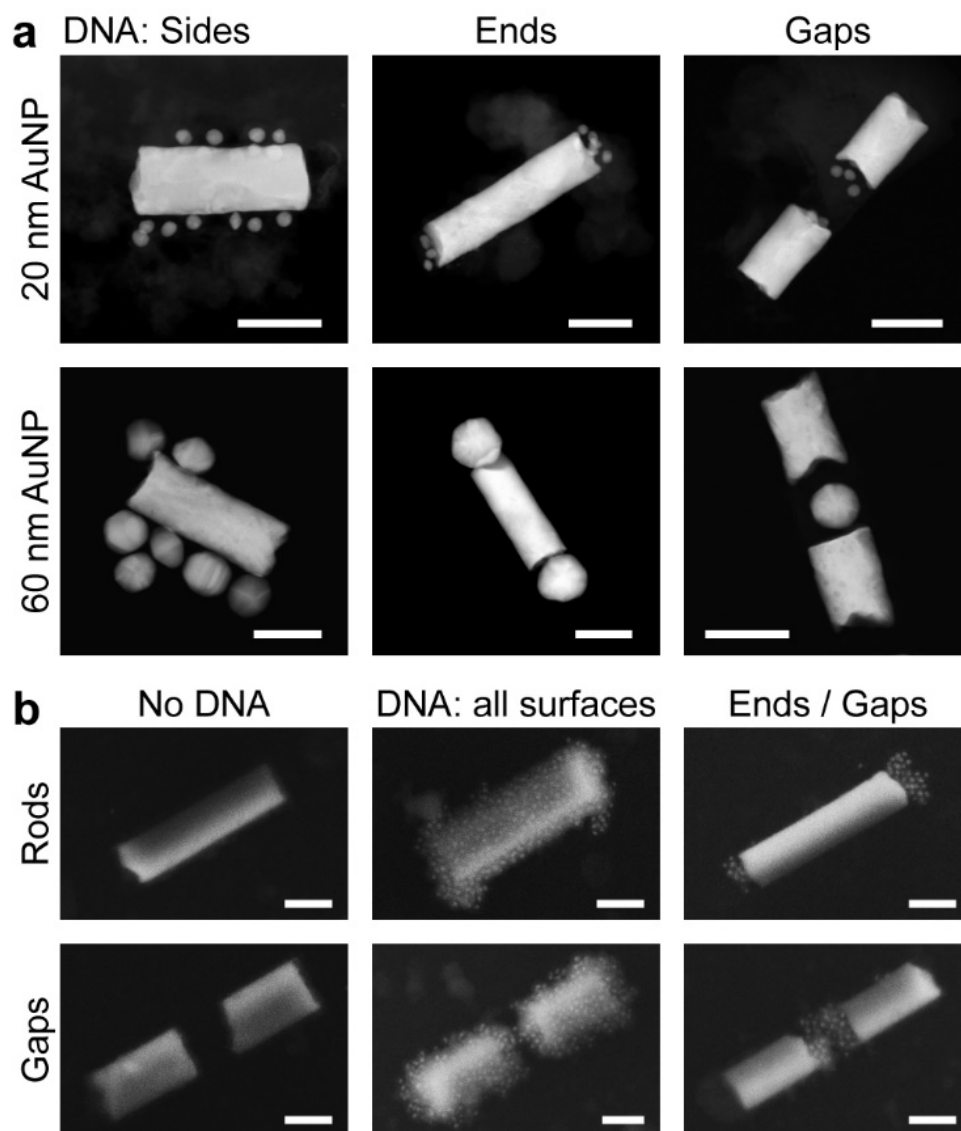


Figure 2.5. Electron micrographs showing the DNA-directed assembly of spherical Au nanoparticles onto the selectively modified Au nanorods and nanogaps. The assemblies are shown in two ways: (a) assemblies in solution (dark-field STEM) and (b) on a substrate (SEM). (a) As expected, the spherical particles with complementary DNA strands are preferentially adsorbed onto the designated DNA-functionalized surfaces. (b) Asymmetric functionalization can be performed after the nanorods are cast onto a SiO₂ substrate. Stepwise assembly of 20 nm spherical particles (two layers) show clear discrimination among un-functionalized, non-selectively functionalized, and selectively functionalized (from left to right) nanorods/nanogaps. The assembled structures are embedded in silica before imaging. Additional micrographs can be found in the Supporting Information. Scale bars: (a) 100 nm and (b) 200 nm.

room temperature to passivate the exposed Au surfaces with the SAM as described above. After being washed in ethanol and water, the chips were soaked in 3% aqueous FeCl_3 for 5 min and the sacrificial Ni capping layers were removed. The SiO_2 sheath deposition can be skipped here because the dimer structure stays intact after the removal of the sacrificial Ni segment due to its physical adsorption onto the substrate. The newly exposed Au surfaces were functionalized with 3'-propylthiol-terminated DNA in an aqueous 10 mM PBS with 1.0 M NaCl. Two layers of 20 nm spherical Au nanoparticles were selectively and sequentially assembled onto the DNA-modified Au rods or gaps via a stepwise growth method.³⁰⁻³¹ Scanning electron micrographs of silica-embedded¹⁰¹ samples showed that the nanoparticle clusters are localized only on the targeted DNA-functionalized surfaces (on the rod ends or in the gaps, **Figure 2.5b**, additional images in **Appendix A**).

These proof-of-concept examples illustrate the power of combining templated approaches with DNA programmable assembly methods for orthogonally controlling nanostructure functionalization. When one considers the broad range of materials and geometric structures that can be synthesized and used in such methodologies,^{18-20, 22, 95-96} the techniques described will allow researchers to rapidly construct assemblies of nanostructures with interesting chemical and physical properties for possible applications in catalysis, molecular detection, therapeutics, and optics (e.g. one-dimensional nanocavities). This methodology also has the potential to serve as a new testbed for fundamental optoelectronic studies of nanoparticle assemblies and is a valuable expansion of programmable DNA-mediated techniques.

2.4 Charge Transport through DNA Strands

The selective passivation method could be applied to the OWL-based nanocircuitry fabrication (**Figure 2.6a,b**), to solve the problem of leakage current through the environment. Specifically, Au-Ni-Au trisegment nanowires are synthesized via templated electrochemical deposition (described in previous sections) through AAO membrane with 55 nm pore diameters. After the removal of Ag layers and the template, the nanowires were dispersed in solution, and then were cast onto a Si chips with thermal oxide (500 nm thick) and pre-patterned electrodes. The nanowire-incorporated circuits are completed by connecting the each of a Au dimer to patterned electrodes. Then, before etching Ni segments, all of the exposed Au surfaces except for the gap faces were passivated by the formation of SAM in ethanolic solution of 10 mM MHA, as described in the previous section. Then, the chip was washed thoroughly with ethanol and water, and the sacrificial Ni segments were etched by 3% FeCl₃, which opened the gap surfaces between the Au dimers. The device with pristine Au gap surfaces were dipped in 10 μM DNA solution, (36-mer C and D, **Table 2.2**) with 0.5 M NaCl, 10 mM PB (pH 7.6), and 0.01% sodium dodecyl sulfate (SDS). The DNA sequence was designed in such manner that the strands were duplexed in the saline with the phosphorothioate-terminated 3'-ends, whose length is about 12 nm and conformation is supposedly linear (persistence length of duplex DNA \approx 40 nm).¹⁰²⁻¹⁰³

The measurement was carried out with a drop of saline solution on top of the chip in an effort to maintain the duplex formation of DNA. Although a significant reduction in the background signal was observed (\sim nA range), the signals from the DNA-bridged devices were still too low to be measured with the OWL-based devices, since the background current through empty gap devices was still high and device-to-device variation was larger (**Figure 2.6c**). It was

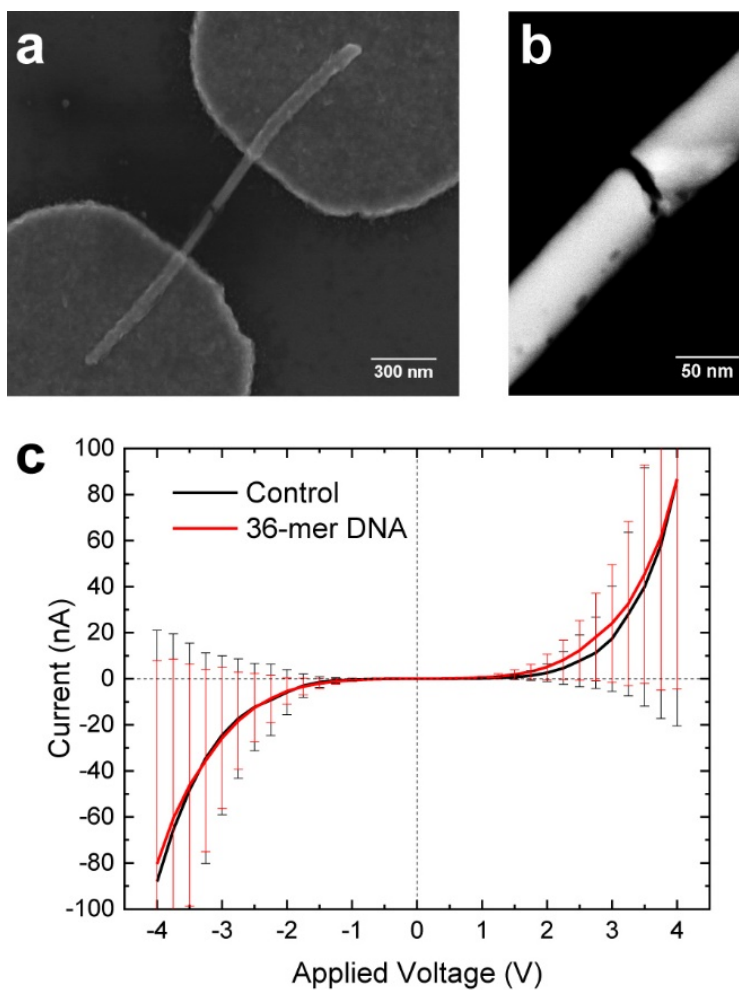


Figure 2.6. (a) A SEM micrograph for an OWL-generated molecular transport junction bridged with DNA. Scale bar: 300 nm. (b) A STEM micrograph of a gapped nanowire in the same batch, showing ~10 nm gap spacing. Scaler bar: 50 nm. (c) The I-V characteristics measured and averaged from more than 10 devices for each sample (control: empty gaps).

probably caused by leakage current and tunneling across the gaps. It was also a problem that the DNA-junction formation was not assured by measuring the electrical conductivity.

2.5 Charge Transport through DNA-Assembled Superlattices

To address the problem, a new design of OWL-based device architecture accommodating DNA-nanoparticle superlattices was attempted (**Figure 2.7a**). Such design confirms the presence of DNA within the OWL gap from the presence of localized nanoparticle superlattices interconnected by DNA duplexes. Although nanoparticles assembled within the gap, the assembly disbanded when the device was washed to remove excess salt crystals, which may interfere with electrical measurements (**Figure 2.7b**). The disassembly is due to the dehybridization of cooperative DNA bonds in the absence of NaCl. To maintain a DNA-interconnected structure, we adopted post-assembly chemical treatments such as silica-embedding¹⁰¹ and intercalation of DNA duplexes.¹⁰⁴⁻¹⁰⁵

In this experiment, multi-segmented Au-Ni-Au nanowires 270 nm in diameter were electrochemically grown in the pores of AAO membranes. The wires were then dispersed into solution with the dissolution of the Ag backing layer and AAO membrane and were subsequently cast onto a thermal oxide silicon wafer with predefined electrodes. Both ends of the nanowires were connected to isolated electrodes by e-beam lithography. The exposed Au surfaces were passivated with a 10 mM MHA solution (in ethanol) for 5 h. After successful passivation of the exposed Au surfaces, the Ni segment was etched with a 3% FeCl₃ aqueous solution (5 min) to expose the gap faces of the Au nanorods. Upon exposure, the pristine Au surfaces were functionalized with thiol-modified DNA (thiol-modified type A, in **Table 2.2**). Au nanoparticle superlattices were grown selectively in the gap region by iterative attachment of particles

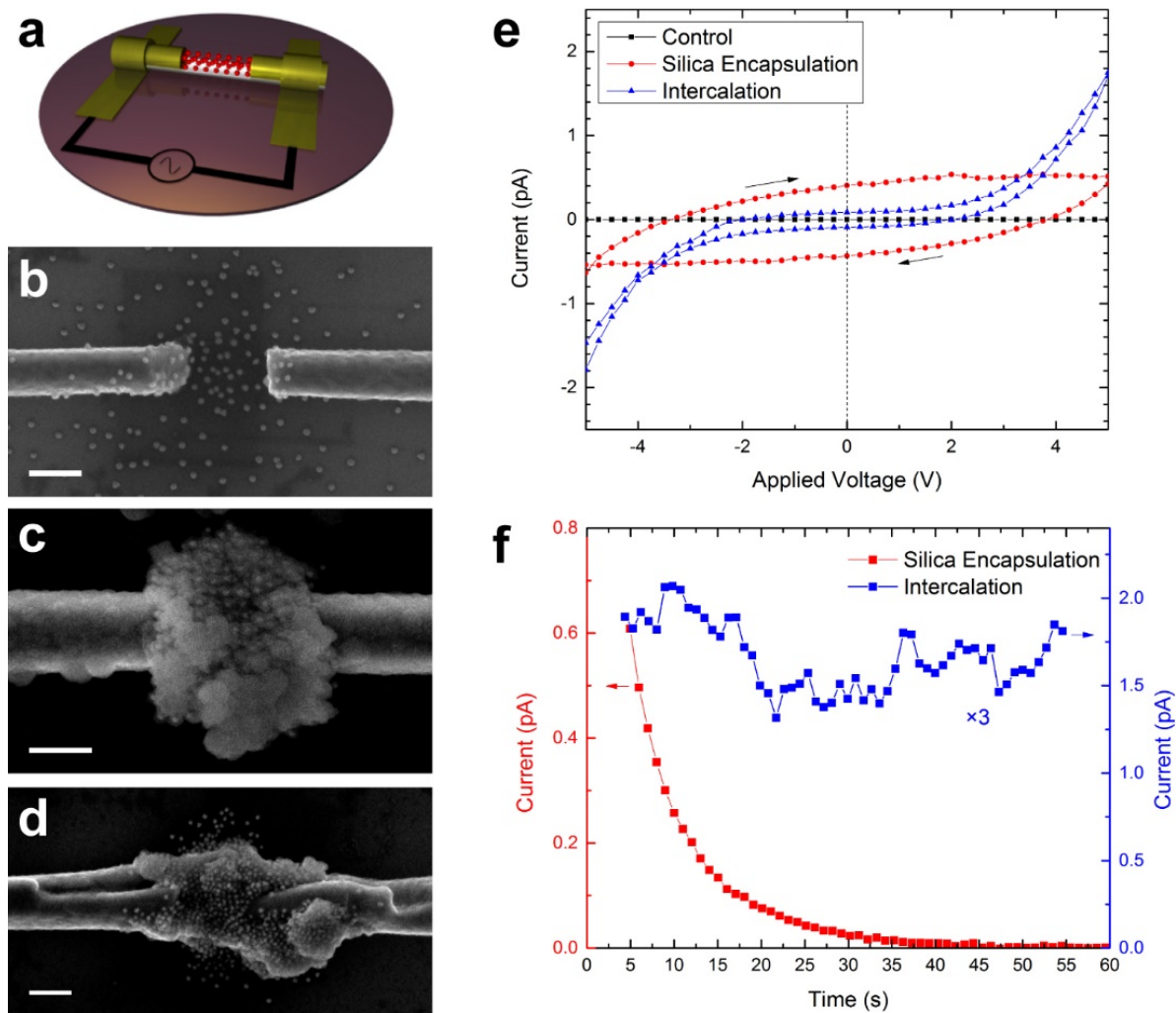


Figure 2.7. (a) A schematic illustration for a new design where an OWL-generated nanogap is filled with DNA-assembled nanoparticle superlattices. (b) Even though the designed structure was formed as designed, the superlattices disassembled with a brief dip-washing in water. Thus, stabilization methods were employed to retain such structure in the gap for measurement, (c) silica encapsulation and (d) RuII-complex intercalation. All scale bars in (b-d) are 100 μm . (e) I-V characteristics of samples in (b-d). (f) The temporal responses of the current flow with constant voltage at 5 V.

functionalized with DNA having complementary sequences, using literature precedures.^{30, 35} To perform measurements of the superlattices, two post-assembly treatments were attempted to facilitate solid state measurements (**Figure 2.7c,d**).

First, a silica embedding method was used.¹⁰¹ In this method, an ammonium-functionalized silane was introduced where the positively-charged ammonium group electrostatically associates with the negatively-charged DNA backbone. Triethoxysilane (TES) was then introduced and precipitated as silica around the initiator-carrying ammonium salt. As expected, the silica encapsulation kept the localized superlattice from being shattered and it was able to bring the structure to solid state to observe under scanning electron microscope (SEM). While the silica imparts structural control to the DNA nanoparticle systems, the state of the DNA within the silica is not known. This prompted us to find a method in which the stabilization of the structural DNA duplexes is better known in order for us to reliably measure the conductivity of the interconnecting DNA.

To do this, we looked to small molecule intercalators to staple DNA-mediated nanoparticle superlattices. As a case study, we used $[\text{Ru}(\text{dipyrido}[2,3\text{-}a:3',2'\text{-}c]\text{phenazine})(\text{N-N})_2]^{2+}$ -based small molecules (**Figure 2.8**).¹⁰⁵ These small molecules interact with double-stranded DNA by the insertion of flat,

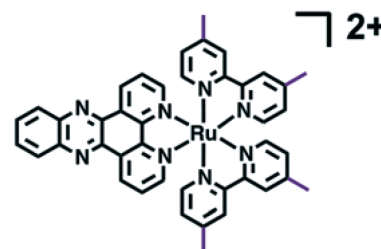


Figure 2.8 Molecular structure of Ru^{II} intercalator complex.

electron rich dipyrido phenazine (dppz) ligand into adjacent DNA bases, subsequently strengthening the π -stacking interaction of bases. The overall positive charge of Ru^{II} -based small molecules induced favorable electrostatic interaction with the negatively charged phosphate backbone, which further increased DNA binding affinity. Using small angle X-ray scattering (SAXS) and SEM, it has also been shown that the intercalation of these molecules effectively

stabilizes the DNA duplex such that Au nanoparticle superlattice stays intact with the exclusion of NaCl, while maintaining the overall structure. The incorporation of small molecules was also expected to be advantageous because these molecules promote relatively strong and orientation-sensitive π -stacking interactions which are commonly attributed to the electron transfer through DNA duplexes.

For intercalation by the Ru complex ion, the assembled superlattice devices were incubated in an aqueous solution at 40 μM Ru^{II} intercalator and 0.5 M NaCl for at least 12 hours. After sufficient time for equilibrium, the devices were washed in 40 μM intercalator solution 5 times to remove excess NaCl, followed by incubation in 40 μM intercalator solution for 12 hours at room temperature. This procedure stabilized the DNA-nanoparticle superlattices in the absence of NaCl. Fluorescence titration assay of free DNA suggests that binding affinity of Ru^{II} complexes increases at lower NaCl concentration.¹⁰⁶ Thus, incubation in 40 μM Ru^{II} solution without NaCl is expected to result in higher degree of intercalation. This argument was well corroborated with ΔT_m measured for DNA-nanoparticle superlattices that are unintercalated, intercalated in solution at 40 μM Ru intercalator and 0.5M NaCl, and intercalated in 40 μM Ru intercalator solution with no salt.¹⁰⁷ Indeed, in **Figure 2.7d**, we see the successful preservation of interconnected nanoparticles within the OWL gap.

Electrical measurements were subsequently carried out in a vacuum cell ($\sim 10^{-5}$ Torr) to minimize effects from ambient humidity and air. The I-V characteristics of three different samples were plotted in **Figure 2.7e**. No measurable current was detected from the untreated sample after washing. This was expected because the dip-washing resulted in the dehybridization of DNA duplexes and eventually the disassembly of DNA-NP superlattices. Measurable signals were detected from both silica-embedded and intercalator-inserted superlattices but with different

characteristics. The dual sweep more strongly contrasts the difference where the silica-embedded sample showed a large hysteresis compared to that of the intercalator-inserted superlattices. The hysteresis with such shape is characteristics of capacitors, where the current was induced as a response to $\Delta V/\Delta t$. This assumption was proved to be valid by the temporal response which clearly shows exponential decay of current over time (**Figure 2.7f**). Meanwhile, the current from the intercalator-inserted superlattices was stable ~ 1.7 pA at 5 V bias. The bulk resistivity can be approximated to be $\sim 2 \times 10^6 \Omega \cdot \text{m}$, a value which sits between bulk semiconductors and insulators. Although these experiments were unable to isolate the contribution to the charge transport by DNA duplexes, the measurements revealed possible solid-state electronic applications of the DNA-interconnected superlattices.

2.6 Conclusions

Although the OWL-based DNA-interconnected nanocircuitries turned out to be not ideal to define the conductivity of DNA strands and nanoparticle superlattices, many valuable outcomes were discovered. Nanostructures synthesized by a templated method can be asymmetrically functionalized with DNA, easily by unveiling the covering materials orthogonally without additional efforts to masking them. The construction of nanogap junctions bridged by nanoparticle superlattices inspired for the incorporation of such structures into device architectures.

2.7 Experimental

2.7.1 Materials and Instruments

AAO templates were purchased from Synkera and Whatman. A PVD 75 instrument (Kurt J. Lesker Company) was used for Ag and SiO_2 deposition during OWL methodology and for Cr

and Au for electrode patterns. Electroplating solutions were purchased from Technic Inc. (Techni Silver Cylless® II RTU for Ag, Orotemp 24 RTU for Au, and Nickel Sulfamate RTU for Ni). NaOH, FeCl₃, acetone, and MHA were purchased from Sigma-Aldrich. An Oligreen® assay kit was purchased from Life Technologies. Citrate-capped spherical Au nanoparticles with diameters of 20 nm and 60 nm, respectively, were purchased from Ted Pella. Milli-Q® water was used in aqueous solutions and washing. Electron micrographs were taken by Hitachi SU8030 FE-SEM and HD2300 FE-STEM. FEI Quanta SEM was used for electrode patterning by e-beam lithography.

The electrical measurements were carried out by a Keithley 4200 SMU coupled with a ST-500 Probe Station by Janis Research Company Inc.

2.7.2 Synthesis and Characterization of DNA

All oligonucleotides used in this work synthesized on a MerMade 12 automated oligonucleotide synthesizer (BioAutomation) with reagents from Glen Research. Oligonucleotides were synthesized with 5' trityl group and purified with reverse-phase high-performance liquid chromatography (HPLC; Agilent), followed by standard deprotection procedures.²⁵ Matrix-assisted laser desorption ionization time-of-flight mass spectrometry (MALDI-TOF; AutoFlex-III, Bruker) was used to validate the synthesis and purification processes by checking the molecular weight of the oligonucleotides. The OligoAnalyzer tool (Integrated DNA Technologies) was used to predict the extinction coefficient and molecular weight of each DNA strand. The absorption at $\lambda = 260$ nm (Cary 5000 UV-vis spectrophotometer; Varian) was used to quantify the synthesized DNA strands.

The DNA design for the crystallization of PAEs in this work follows the literature.¹⁵ Briefly, Au nanoparticles were functionalized with one of two single-stranded 3'-propylthiol-modified “anchor” strands. To each of the “anchor” strands, we hybridized a second “linker” strand. Specific sequences used in this work are listed in **Table 2.2**.

Table 2.2. DNA sequences used in this study.

Thiol-modified DNA strands	DNA Sequences (5' → 3')
A	TCA ACT ATT CCT ACC TAC (Spacer 18) ₂ -SH
B	TCC ACT CAT ACT CAG CAA (Spacer 18) ₂ -SH
Linker strands	DNA Sequences (5' → 3')
A self-complementary linker	GTA GGT AGG AAT AGT TGA (Spacer 18) ₁ GCG C
A linker	GTA GGT AGG AAT AGT TGA (Spacer 18) ₁ TTC CTT
B linker	TTG CTG AGT ATG AGT GGA (Spacer 18) ₁ AAG GAA
Conductivity Experiments	DNA Sequences (5' → 3')
36-mer C	TCA ACT ATT CCT ACC TAC TCC ACT CAT ACT CAG CAA*
36-mer D	TTG CTG AGT ATG AGT GGA GTA GGT AGG AAT AGT TGA*

*3'-ends of the 36-mer C and D are terminated with phosphorothioate.

“Spacer 18” refers to the six ethylene glycol units with modified phosphoramidites, which were manufactured by Glen Research.

2.7.3 Electrochemical Synthesis of Nanorods

AAO templates with pore diameter of 35 nm (SM35-50-25) were submerged in 0.5 M NaOH (aq) for 3 min to widen and refine the pores. Whatman Anodisc® templates were used to synthesize the thicker rods used for substrate assemblies. First, a 250 nm thick Ag layer was deposited on one side of the template by e-beam physical vapor deposition. Ag, Ni, or Au was electrodeposited in the nanopores in a three-electrode system with the AAO/Ag as the working electrode, a Pt mesh as the counter electrode, and an Ag/AgCl reference electrode. While the length of each segment was controlled by the amount of charge, the applied potentials were -980 mV for Au and -900 mV for Ag and Ni.

2.7.4 DNA Functionalization

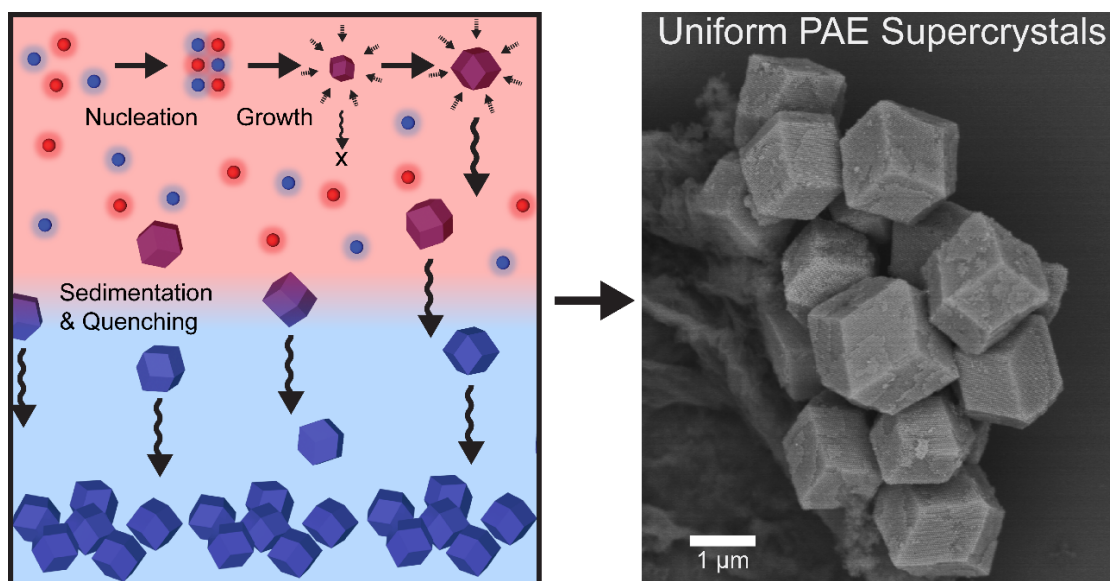
10 mL of citrate-capped nanoparticles (either 20 nm or 60 nm in diameter) were first incubated with 10 optical density (OD) of DNA for more than 3 h at room temperature. Then, PB (pH 7.6) and SDS (Sigma Aldrich) were added to the solution, and aqueous 2 M NaCl was added gradually over 3 h for final concentrations of PB, SDS, and NaCl, to become 10 mM, 0.01%, and 0.5 M, respectively.

The electrochemically synthesized nanorods and nanogaps have clean surfaces, free of surfactants. Therefore, the nanostructures were directly incubated in a PB (pH 7.6) solution containing 5 OD of thiol-modified DNA A (Table S1), 1.0 M NaCl, and 0.01% SDS after removal of the masking materials (AAO or Ni).

2.7.5 DNA Loading Density on Spherical Particles

For this calculation, the Au nanoparticles were dissolved in 25 mM KCN (aq.) at 70 °C for 1 h. The number of DNA strands was measured with an Oligreen® assay, where the fluorescent signal was calibrated linearly by standard solutions of known concentrations of DNA with the same sequence. The concentration of the particles was measured by ICP-OES and TEM analysis, for the concentration of $\text{Au}(\text{CN})_2^-$ ions and the mass of individual particles, respectively. Comparing the concentration of Au atoms in solution to the number of atoms in a single particle, the concentration of the particles could then be extracted. The concentrations of particles and DNA were then used to calculate the average loading density of thiol-modified DNA on an Au nanoparticle.

Chapter 3 Uniformity Control over Colloidal Single Crystal Formation



Portions of this chapter have been published¹⁰⁸ in *Nano Letters*, **2018**, *18*, 6022.
Co-authors of this work: Jessie C. Ku, Jae-Hyeok Lee, Mark C. Hersam, Chad A. Mirkin
Copyright 2019 American Chemical Society

3.1 Summary

With the advent of DNA-directed methods to form “single crystal” nanoparticle superlattices, new opportunities for studying the properties of such structures across many length scales now exist. These structure-property relationships rely on the ability of one to deliberately use DNA to control crystal symmetry, lattice parameter, and microscale crystal habit. Although DNA-programmed colloidal crystals consistently form thermodynamically favored crystal habits with a well-defined symmetry and lattice parameter based upon well-established design rules, the sizes of such crystals often vary substantially. For many applications, especially those pertaining to optics, each crystal can represent a single device, and therefore size variability can significantly reduce their scope of use. Consequently, a new method was developed based upon the density difference between two layers of solvents to control nanoparticle superlattice formation and growth. In a top aqueous layer, the assembling particles form a less viscous and less dense state, but once the particles assemble into well-defined rhombic dodecahedra superlattices of a critical size, they sediment into a higher density and higher viscosity sublayer that does not contain particles (aqueous polysaccharide), thereby arresting growth. As a proof-of-concept, this method was used to prepare a uniform batch of Au nanoparticle (20.0 ± 1.6 nm in diameter) superlattices in the form of 0.95 ± 0.20 μm edge length rhombic dodecahedra with bcc crystal symmetries and a 49 nm lattice parameter (cf. 1.04 ± 0.38 μm without the sublayer). This approach to controlling and arresting superlattice growth yields structures with a three-fold enhancement in the polydispersity index.

3.2 Background

Nanoparticles are becoming to nanotechnologists what atoms are to chemists, and many methods have emerged for assembling them into periodic and highly crystalline structures.^{1-3, 13, 15-16, 109-116} To control colloidal crystallization, bonding strategies have relied on the use of electrostatics,^{4, 117-120} small molecule coordination chemistry,¹²¹⁻¹²² polymer spacers,¹²³⁻¹²⁴ and high-information content oligomers, such as DNA and variants of it.^{15-16, 109} Oligonucleotides are particularly attractive because of their length, which can be matched with the size of the particle building blocks and chosen based upon the desired nanoparticle separation, the large number of possible programmable interaction pairs, and the persistence length of duplex architectures, which allows one to control bonding directionality over relatively large length scales.¹ Such flexibility has allowed us and others to synthesize over 500 colloidal crystals spanning approximately 33 different symmetries^{16-17, 24-26, 125-126} with lattice parameters deliberately varied from 25 nm to a few μm .^{16, 127} In addition, powerful design rules¹⁶ have been developed for controlling crystal symmetries that are independent of particle composition and size.^{18, 127} Therefore, once a strategy has been developed to generate a particular crystal, the particle composition can be independently tuned. In other words, in this type of chemistry, bonding is independent of “atom” identity. Consequently, one can deliberately achieve crystallization of a vast number of nanoparticle building blocks, simply as a function of particle size and shape, and by taking into account the types of oligonucleotides immobilized on their surfaces.

Recent advances have even provided *microscale* geometric control over DNA-assembled colloidal crystals by two different approaches: substrate surface growth (the equivalent of epitaxial growth)³⁰ and thermodynamically controlled crystallization in solution.²⁷ For the solution case, with an A-B complementary (size ratio = 1:1) PAE system where one set of particles are

functionalized with A-type DNA linker strands and the other set with complementary B-type DNA linkers, a bcc superlattice¹⁵⁻¹⁶ with a rhombic dodecahedron microscopic geometry, the Wulff polyhedron, will form.²⁷ In addition to realizing many bcc crystals with the characteristic rhombic dodecahedron shape, we have shown that cube-shaped particle building blocks yield cube-shaped crystals and rhombic dodecahedra particle building blocks yield octahedron-shaped microcrystals.²⁸

The realization that DNA-programmable assembly allows one to control the structure of crystalline matter on multiple length scales has led to a variety of interesting discoveries, especially in the field of optics.⁹⁻¹⁰ Indeed, being able to control microscopic crystal geometry allows one to decouple nanoscale and mesoscale optical effects¹⁰ and has led to the synthesis of photonic crystals,⁹ directional microcavity emitters,¹¹ and “alloy” superlattices.¹³ The ability to make well-formed single crystal structures with microscopic rhombic dodecahedra allows one to systematically uncover the roles of the dimension of microcrystals,¹⁰ lattice parameters,⁹⁻¹⁰ and nanoparticle size and anisotropy³⁴ in controlling optical properties and has opened the door for using such crystals as plasmonic optical cavities, waveguides, visible-light metamaterials, and optical circuitry.¹²⁸⁻¹³⁰

Although DNA-programmable assembly allows one to realize highly ordered structures that would be difficult, if not impossible, to make using other methods, control over microscopic and larger length scale features is limited. For example, if one uses complementary PAEs with 20-nm Au cores to form colloidal crystals with a bcc lattice, the variation in single crystal size can be enormous (i.e., for a mean crystal size of 1 μm there is typically a polydispersity index (PDI) \sim 0.15, which corresponds to an \sim 0.4 μm standard deviation). If one is to use such colloidal crystals, either to create functional devices or simply as building blocks themselves to create larger

superstructures, strategies must be developed to assemble and isolate them as more uniform entities with PDI values approaching 0.01.¹³¹ Methods for improving uniformity are especially needed in the case of optical devices where a particular geometry may be desired for a given response, but where differences in crystal edge length can lead to radically different optical outputs.¹⁰

3.3 Colloidal Crystallization and Density Layers

For a new method for growing and isolating microscopic colloidal crystals, a deeper perspective on the crystallization process and the source of polydispersity was needed. In the growth of single-crystalline PAE microcrystals via slow cooling, PAEs nucleate and assemble into their thermodynamically favored state. Importantly, as the microcrystals grow, they reach a critical size at which point gravitational forces overcome stabilizing Brownian motion, and the microcrystals begin to sediment from solution (**Figure 3.1a**). However, the microcrystals remain reactive for further growth and coalescence, a major contributor to size and shape polydispersity (**Figure 3.1b**). Based on this thought experiment, we took inspiration from biological techniques to separate macromolecules in order to develop a density gradient approach involving a high density and high viscosity aqueous polysaccharide solution layered below a low density PAE growth solution designed to collect the superlattices as they form and sediment into the high viscosity layer (**Figure 3.1c-d**).

The theoretical background for the hypothesized size uniformity of sedimenting particles is based upon the competitive effects of gravity and Brownian motion on the colloidal stability and sedimentation of superlattices. The relative strength of the gravitational energy to the thermal

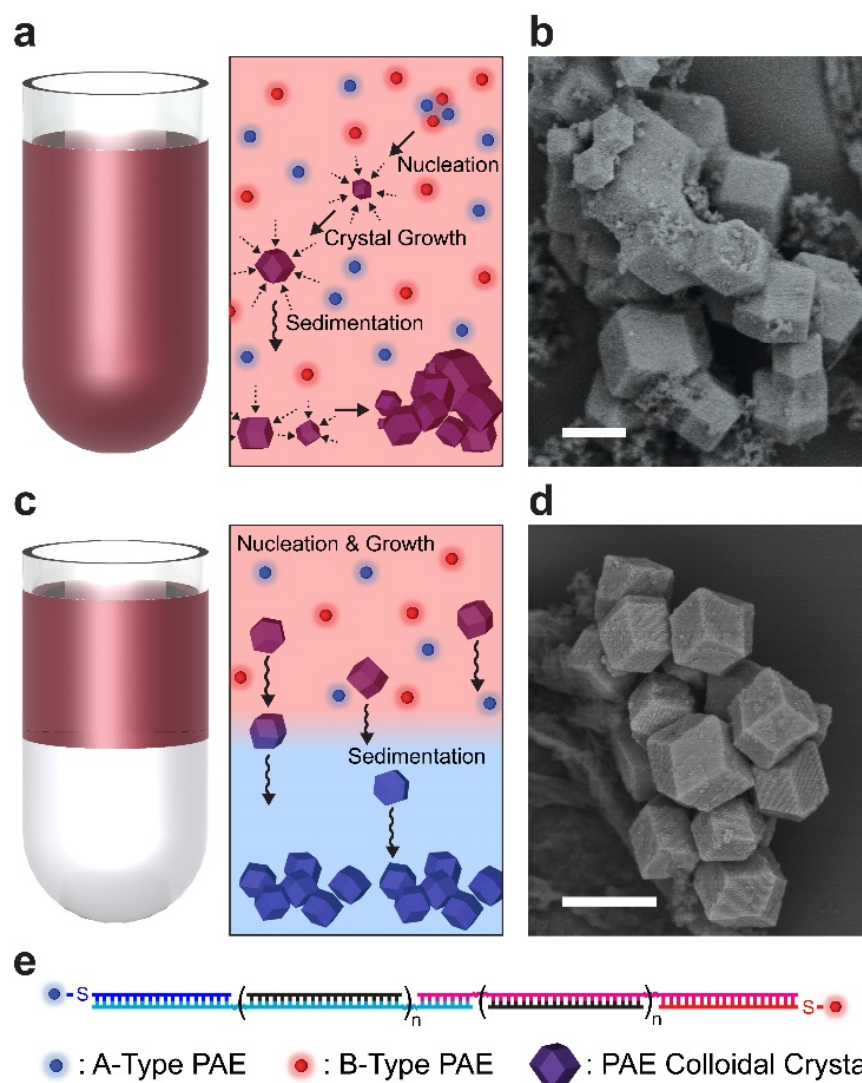


Figure 3.1. Schematics and SEM images comparing the standard crystallization process of nanoparticle superlattices and a method to enhance uniformity. (a) Schematics of the current slow-cooling method where faceted rhombic dodecahedra may continue to grow as they sediment out of solution. (b) A representative scanning electron micrograph of rhombic dodecahedra synthesized by the current slow cooling method, where the sizes of the microcrystals vary, and coalescent crystals are frequently observed. (c) Schematics of proposed incorporation of a quenching sublayer to realize more uniform colloidal crystals. (d) A scanning electron micrograph of the microcrystals collected from the viscous sublayer shows improved uniformity in size and shape. e. Legends for the schematics, describing the PAE system used in this study: the blue and red circles represent A and B PAEs, respectively, which hybridize to each other by DNA anchor strands functionalized on particles and linker strands connecting PAEs together (Table 3.6). The number of modular units (n) controls the length of DNA linkers and lattice parameters of the resulting superlattices. Schemes are not drawn to scale. Purple rhombic dodecahedra represent the assembled microcrystals. Scale bars: 2 μm .

energy can be described by the dimensionless Peclet number (Pe).¹³² In an ideal case of a spherical object with a radius of a , Pe can be expressed as:

$$Pe = \frac{\frac{4}{3}\pi\Delta\rho g a^4}{k_B T} \quad (3.1)$$

where $\Delta\rho$ is the difference in density between the spherical object and the solution, g is the gravitational acceleration, and $k_B T$ is the thermal energy as the product of Boltzmann constant, k_B , and the temperature, T . If we assume that the object begins sedimenting at a certain value of Pe , the critical size of sedimentation can be described by:

$$a = \left(\frac{3 Pe k_B T}{4\pi\Delta\rho g} \right)^{\frac{1}{4}} \propto \left(\frac{T}{\Delta\rho} \right)^{\frac{1}{4}} \quad (3.2)$$

Hence, in principle, the size of a settling microcrystal at the initial moment of sedimentation is expected to be consistent because the crystallization temperature and the density of the superlattice are considered constant in a given PAE system.

3.4 Materials Selection for Density Layers

In order to choose suitable materials for each layer, a series of preliminary experiments were carried out. Sucrose solution, a well-known density gradient media, was studied first; two 0.5 M NaCl solutions, one containing free PAEs without linkers and the other suspended bcc microcrystals, were slowly added on top of saturated aqueous sucrose (17 g per 10 mL of water). As expected, the free PAEs (red colloids), did not penetrate the sucrose sublayer (**Figure 3.2a**, left), while the microcrystals sedimented through the top layer and eventually into the sucrose solution, where they disassembled as observed by a change in color (turns red, **Figure 3.2a**,

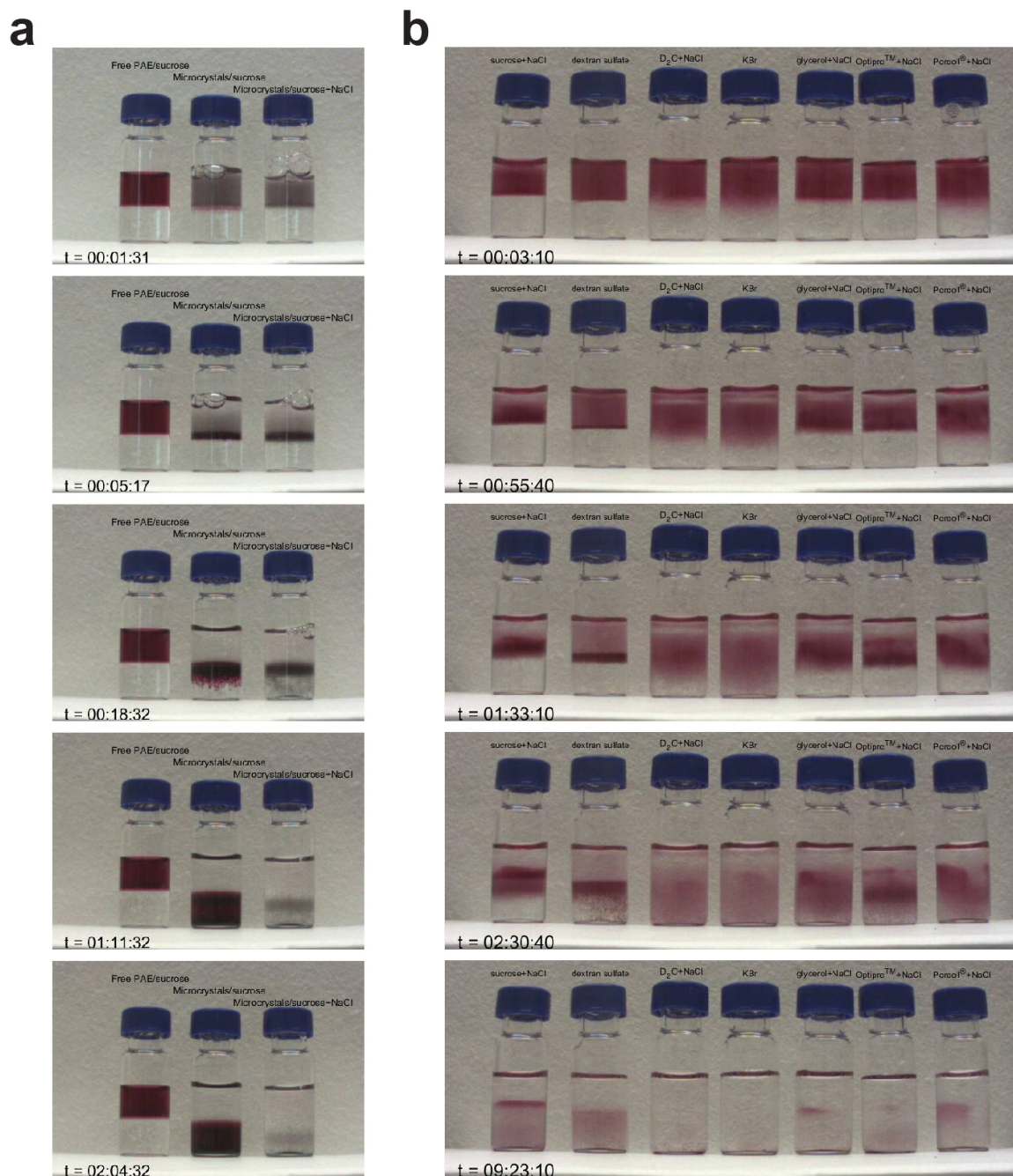


Figure 3.2. (a) Density layers built with free PAE solution without linkers/saturated sucrose solution (left), microcrystal suspension/saturated sucrose solution (middle), and microcrystal suspension/saturated sucrose solution with 0.5 M NaCl (right). (b) Same PAE solutions mixed with linkers were added on top of different density gradient media on the bottom, saturated sucrose solution with NaCl, 10% dextran sulfate, 0.5 M NaCl in D₂O, 0.5 M KBr, 50% glycerol with NaCl, 2:3 diluted Optiprep™ with NaCl, 2:3 diluted Percoll® with NaCl, from left to right. The time stamps in (a) and (b) are in format of hh:mm:ss.

middle). The dissolution of the crystals resulted from the lack of salt in the sublayer, and with the addition of 0.5 M NaCl to the sucrose solution, no dissolution occurred (**Figure 3.2a**, right).

A similar method was used to identify a material for the dense sublayer where 7 different density gradient aqueous solutions (all frequently used in centrifugation separation methods) were prepared: sucrose (saturated), dextran sulfate (10% w/v), D₂O (100%), KBr (0.5 M), glycerol (50%), Optiprep™ (2:3 diluted), and Percoll® (2:3 diluted) (**Figure 3.2b**, left to right). NaCl (0.5 M) was added to each solution to supply ionic strength for DNA hybridization, except for the dextran sulfate and KBr solutions (these contain a sufficient amount of salt). Then, PAE solutions without DNA linkers were gently placed on top of each density gradient solution, followed by the addition of DNA linkers ($n = 1$, **Table 3.6**) to initiate PAE aggregation at $t = 0$. After observing the aggregation and sedimentation processes, dextran sulfate was identified for the high-density sublayer as the density barrier was retained and minimal.

3.5 Results and Discussions

3.5.1 Observation of Colloidal Crystal Formation and Sedimentation

In order to verify our hypothesis, we synthesized PAE colloidal crystals in two different batches, with and without the quenching solution beneath the growth solution (**Figure 3.3**). To visualize the slow cooling process, we built a bath containing ~11 L of water where the temperature was precisely controlled (0.01 °C) by an immersion circulator. Then, a growth solution containing 5 nM each of A and B PAEs (20 nm Au core and DNA linkers with one modular unit ($n = 1$), **Figure 3.1e** and **Table 3.6**) with 0.5 M NaCl and 10 mM PB (pH 7.6) was slowly and carefully loaded on top of the dextran sulfate solution (density = $1.058 \text{ g}\cdot\text{cm}^{-3}$ at 25 °C and viscosity = $8.98 \text{ mPa}\cdot\text{s}$ at 20 °C) in a test tube submerged in the water bath.

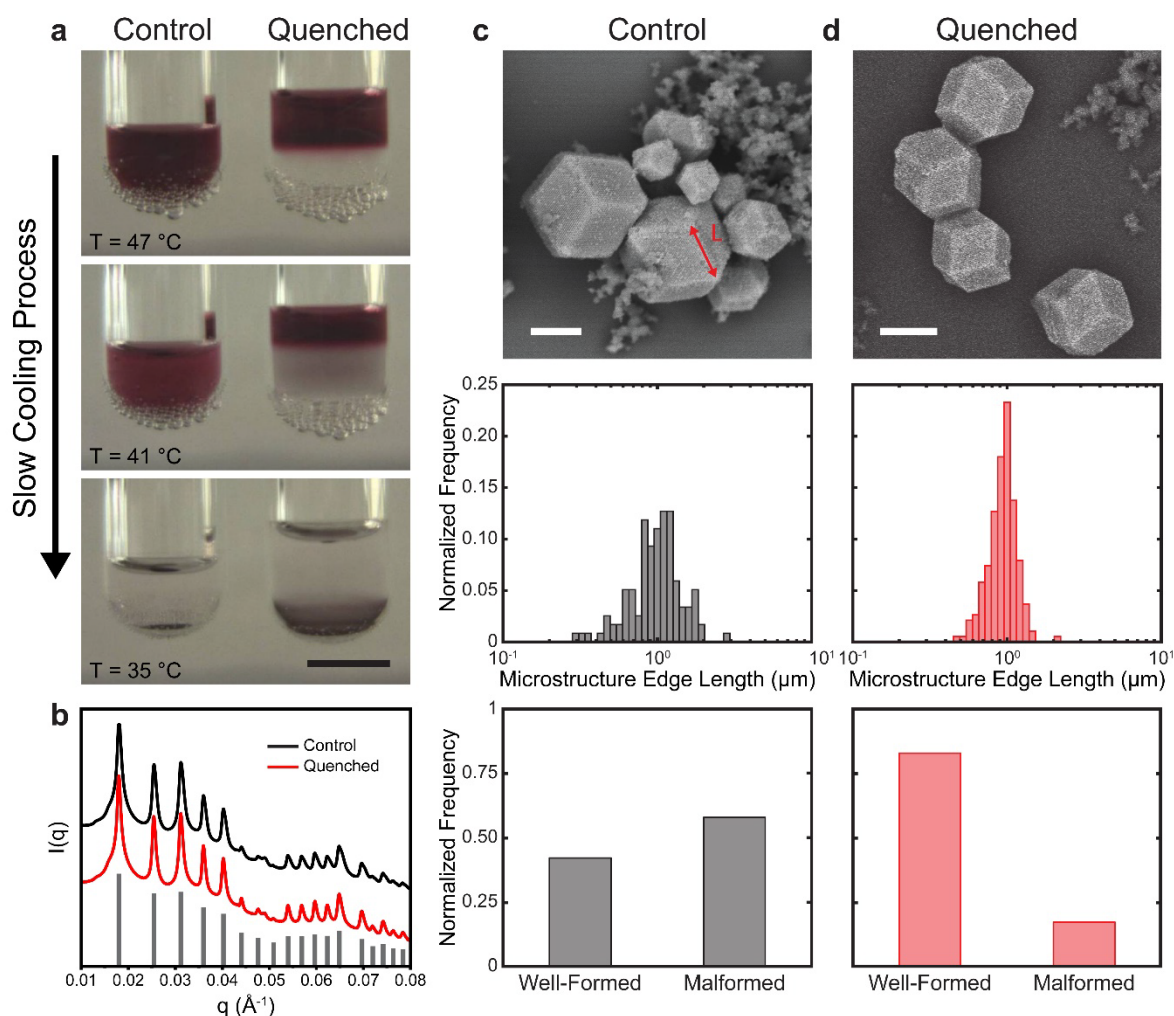


Figure 3.3. Control and quenched superlattices and their size distributions. (a) Optical images of the growth solution of PAEs at different stages of the slow cooling process. As the temperature is decreased at $0.01\text{ }^{\circ}\text{C}\cdot\text{min}^{-1}$ through the melting temperature ($\sim 41\text{ }^{\circ}\text{C}$), the PAEs assemble and sediment out of solution. (b) Radially averaged one-dimensional SAXS data (semi-logarithmic scale) confirms identical bcc lattice symmetry and lattice parameters (gray bars) for the control (black) and quenched (red) samples. (c) A representative scanning electron micrograph of the control sample (top) with its size distribution (middle, semi-logarithmic scale) and frequency of well-formed superlattices (bottom). In the SEM images, the excess silica that forms during the encapsulation process can be observed around the rhombic dodecahedral microcrystals. The red line in the SEM image denotes a characteristic edge length, L . (d) The same information as in c for quenched samples. Scale bars: (a) 1 cm and (c, d) 1 μm .

An identical PAE solution without the quenching sublayer was prepared in another test tube as a control sample. It is important to note that the concentration of Na^+ in the 10% dextran sulfate solution is approximately 0.55 M, supplying sufficient ionic strength without additional electrolytes to maintain DNA hybridization and prevent the settling PAE crystals from disassembling. Both samples were slow cooled in the water bath at a rate of $0.01\text{ }^\circ\text{C}\cdot\text{min}^{-1}$ through the melting temperature (T_m). In agreement with our hypothesis, the colloidally stable free PAEs, which can be visually identified as red, do not penetrate the density barrier during the cooling process, whereas the colloidal crystals (dark gray suspension) drop through the quenching layer as they form and reach a critical sedimentation size (**Figure 3.3a**). The density barrier moves upwards over the crystallization process, a consequence of the decrease in osmotic pressure in the top layer, as the PAE colloids crystallize and sediment. This effect is especially pronounced when superlattice assembly and purification are studied as a function of initial PAE concentration as discussed in a later section. Verified by SAXS (**Figure 3.3b**), the two samples have identical bcc lattice symmetries and parameters which indicates that this simple modification of the crystallization process does not affect the nanoscale form of the PAE colloidal crystals.

3.5.2 Size Uniformity

Microcrystal size characterization was carried out via SEM (Appendix B). Here, the as-synthesized PAE colloidal crystals were transferred to the solid-state by embedding them in silica.¹⁰¹ Once embedded, they retain their crystal structure out of the aqueous NaCl solution, and therefore, can be dropcast onto a Si wafer. The samples were then imaged by SEM, and the characteristic edge lengths (L , one such length illustrated in **Figure 3.3c**) of the rhombic dodecahedra were measured from these micrographs, considering various orientations of the

rhombic dodecahedra and their projection angles. The presence of excess silica, a byproduct from encapsulation process, should be noted. Since the individual PAEs can be resolved under SEM, the microcrystals are distinguishable from the silica debris. To quantify the size uniformity of these microcrystal populations, measured edge lengths for the control and quenched samples were binned (**Figure 3.3c,d**, middle). From these histograms, the distribution of the control sample synthesized without the sublayer results in a mean L of 1.04 μm with a PDI of 0.13. In contrast, the quenched sample has a similar mean L of 0.95 μm but a much improved PDI of 0.044. The size distribution of quenched microcrystals is consistent among the five batches assembled within the same nanoscale form and conditions (mean L between 0.95 and 1.03 μm and PDI between 0.032 and 0.046, **Table 3.1**), demonstrating that the synthesis of PAE crystals with reproducible microscale form is achieved using this method. Under both conditions, smaller, sub-200 nm superlattices were observed, although they occurred more frequently in the control system (the single-phase growth solution). The smaller microcrystals in the quenched samples may persist due to adsorption onto sedimenting microcrystals that carry them into the quenching layer. Because most of these smaller aggregates are not well-formed rhombic dodecahedra and obscured by excess silica, they were not included in the analysis.

Table 3.1. Statistical data for the mean size and PDI of PAE microcrystals (20 nm Au and n = 1 DNA) in different batches.

Batch number	1	2	3	4	5
Counts	189	93	79	128	185
Mean Size (L, μm)	0.95	1.03	0.99	1.01	0.98
PDI	0.044	0.032	0.041	0.038	0.046

3.5.3 Shape Uniformity and Mobility in Viscous Solution

Empirically, the result of the density-based quenching can also be visualized with fewer instances in which superlattices grow into each other when the dextran sulfate layer is present (**Figure 3.1b,d** and **Appendix B**). Qualitative inspections of the micrographs show a larger population of fused and misshapen (malformed) microcrystals in the control samples. It is also informative to include a complementary histogram (**Figure 3.3b-c**, bottom) in which well-formed and malformed superlattices are counted. Here, conjoined or asymmetric microcrystals are categorized as “malformed,” as are non-rhombic dodecahedral microcrystals. From this result, we see that the yield of well-constructed Wulff polyhedral microcrystals improved from 42% (114 total counts) of the imaged population for the control case to 83% (181 total counts) for the quenched samples. This reveals that the denser sublayer effectively quenches inter-crystal interactions and coalescence. The enhancement in the shape uniformity can be attributed to the higher viscosity in the collection layer, as it retards the mobility of colloids, and thus suppresses the undesired post-sedimentation growth and coalescence.

To examine the assembly kinetics in a viscous solution, the decay in extinction at $\lambda = 520$ nm, the localized surface plasmon resonance wavelength of Au nanoparticles, was monitored by UV-vis spectroscopy for 6 h at room temperature (**Figure 3.4**). The normalized extinction at $\lambda = 520$ nm can be approximated as the fraction of unbound free PAEs.^{1, 133} In this experiment, a PAE solution without linkers was prepared, containing 0.25 nM each of complementary A and B PAEs (**Table 3.6**) in 0.5 M NaCl. In the other sample, dextran sulfate was added (5% w/v) to an identical PAE solution for higher viscosity. At $t = 0$, the monitoring was started with the addition of the linker strands. The PAEs in the regular 0.5 M NaCl solution fully assemble within an hour, whereas it takes over 6 h for the PAEs in the viscous media to assemble. Using the Avrami equation,¹³⁴ the

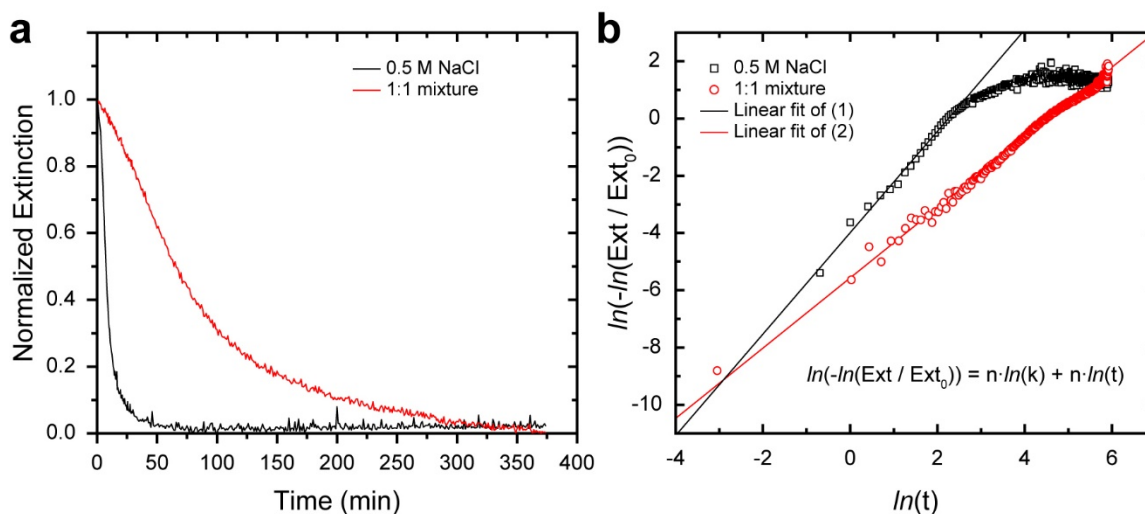


Figure 3.4. (a) Time-dependent extinction decay (at $T = 25\text{ }^{\circ}\text{C}$) of PAEs at $\lambda = 520\text{ nm}$ in a 0.5 M NaCl solution (black) and the same PAEs in 1:1 mixture of 0.5 M NaCl solution and 10% w/v dextran sulfate solution, i.e. 0.25 M NaCl and 5% w/v dextran sulfate (red). At $t = 0$, the linker strands are added so that the PAEs hybridize and are brought into proximity. (b) Same data plotted based upon Avrami theory. The linear fit (least squares method) at the earlier stage of each sample provides the values to calculate the rate constants of the decay.

Table 3.2. Avrami fit of each data and the rate constant from **Figure 3.4**.

	Slope, n	Intercept, $n \cdot \ln(k)$	Rate constant, $k = \exp\left(\frac{\text{Intercept}}{\text{Slope}}\right) (\text{min}^{-1})$	Viscosity, η @ $25\text{ }^{\circ}\text{C}$ (mPa·s)
0.5 M NaCl	1.77 ± 0.04	-3.99 ± 0.06	0.105 ± 0.003	0.96
1:1 mixture of buffer and dextran sulfate 10% w/v	1.23 ± 0.01	-5.57 ± 0.03	0.0107 ± 0.0005	8.24

time-resolved extinction can be described as a plot of $\ln(-\ln(Ext/Ext_0))$ vs. $\ln(t)$ (**Figure 3.4b**).¹³³ From this approximation with the linear fit of the data, the rate constant in each solution can be extracted and quantitatively compared. The rate constant in the dextran sulfate solution is 10 times smaller than in the control sample (**Figure 3.4b** and **Table 3.2**). Indeed, the reduced rates of binding in the dextran sulfate solution results from its higher viscosity, which is inversely proportional to diffusivity as derived from the Stokes-Einstein relationship.

3.5.4 Effect of PAE Concentration on the Size Distribution of Microcrystals

The dextran sulfate sublayer pushes the density barrier upwards as the crystals sediment, resulting in a contraction of the growth solution (**Figure 3.3a**). This is due to the osmotic pressure difference between the top and bottom layers. The volume contraction buffers the decrease in the concentration of PAEs in the growth solution that occurs due to crystallization and subsequent sedimentation. To support this conclusion, another experiment was carried out where the initial total PAE concentration in the top layer was deliberately varied (2, 5, 10, and 20 nM), while the sublayer composition was kept the same (**Figure 3.5**), where it was observed that the degree of volume contraction decreased with increasing PAE concentration. For the 2, 5, and 10 nM samples in **Figure 3.5**, the density barrier moved upward whereas in the 20 nM sample, some colloidal PAEs moved to the dextran sulfate solution, from which we could assume that the osmotic pressure of the 10% w/v dextran sulfate solution is between those of 10 and 20 nM PAE growth solutions. The density barrier expansion turned out to lead to greater superlattice size uniformity for varying initial PAE concentrations (**Table 3.3**). For control samples without quenching sublayers, the mean sizes of the resulting microcrystals increased substantially as function of increasing PAE concentration. Without the sublayer, the excess PAEs at high concentrations resulted in overgrown

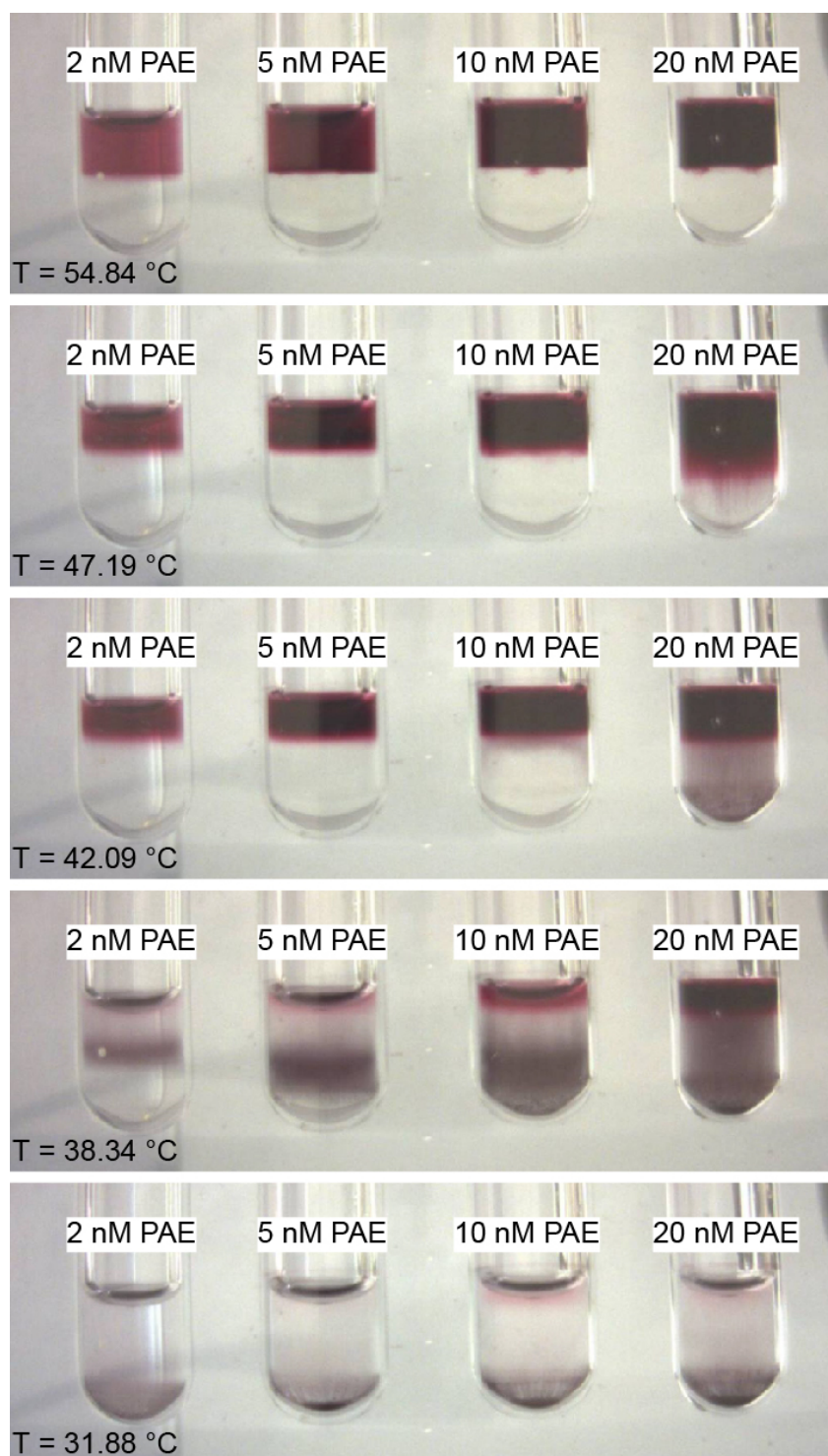


Figure 3.5. Observation of the crystallization process (cooling rate $0.01\text{ }^{\circ}\text{C}\cdot\text{min}^{-1}$) with the dextran sulfate sublayer, and the concentrations of PAE in the growth solutions are varying from 2 nM to 20 nM, from left to right.

microcrystals, while low concentrations resulted in smaller crystals due to a limited PAE supply, both of which contribute to non-uniformity in terms of isolated crystals. With the use of the dextran sulfate sublayer, the concentration-dependence of mean size was significantly reduced for the 5, 10, and 20 nM PAE concentrations. The 2 nM PAE sample resulted in much smaller microcrystals with a relatively high PDI value compared to the higher PAE concentration samples (0.71 μm with PDI of 0.063). The volume contraction in this sample may not be sufficient to overcome the changing PAE concentration that accompanies superlattice formation and sedimentation.

Table 3.3. Concentration-dependent microcrystal size distributions for 20 nm Au and $n = 1$ DNA system.

Initial PAE concentration in growth solution	Control				Quenched			
	Counts	Mean Size (L, μm)	Standard Deviation (σ , μm)	PDI	Counts	Mean Size (L, μm)	Standard Deviation (σ , μm)	PDI
2 nM	165	0.64	0.26	0.16	163	0.71	0.18	0.063
5 nM	115	0.77	0.29	0.14	148	0.97	0.19	0.038
10 nM	159	1.10	0.36	0.11	185	0.98	0.21	0.046
20 nM	228	1.07	0.36	0.12	240	1.01	0.22	0.046

3.5.5 Other PAE Systems

When considering the effect of sedimentation on microcrystal size, the density difference between the microcrystal and background medium may be the most useful variable to change the critical size of these microcrystals (**Eqn. 3.2**). One approach would be to use PAEs that assemble into superlattices of varying volume fractions of Au by tuning the DNA linker length. For the same 20 nm Au nanoparticles with a systematic DNA design, where length is controlled by the number of modular units ($n = 0, 1, \text{ or } 2$, **Table 3.6**), the volume fractions of Au in the crystal lattices were calculated from SAXS data and found to vary from 12.5 to 3.1% (**Table 3.4** and **Table 3.7**). With a density of $19.32 \text{ g}\cdot\text{cm}^{-3}$ for Au and $1 \text{ g}\cdot\text{cm}^{-3}$ for water, the approximated density of the assembled

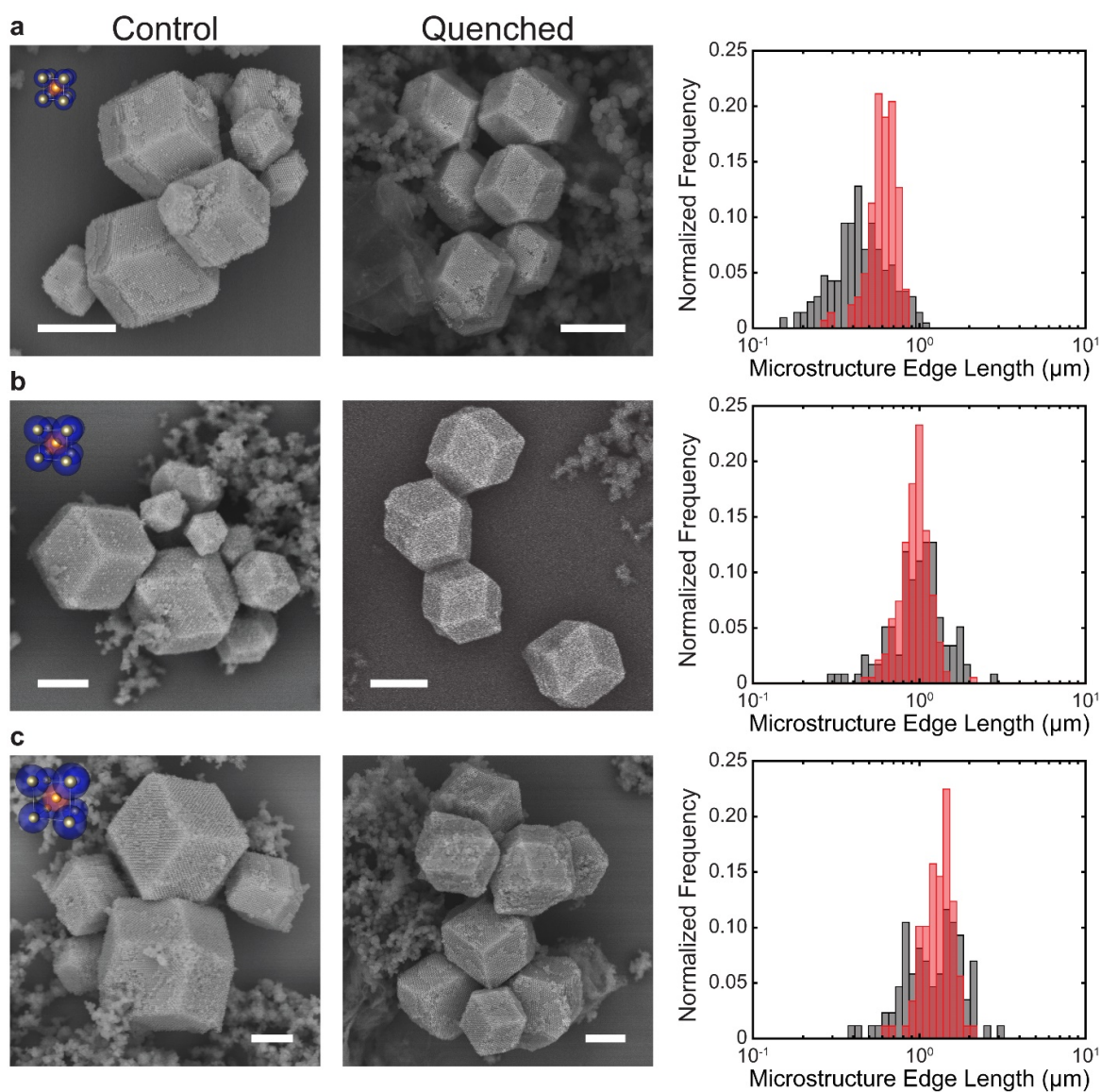


Figure 3.6. Microcrystal size distributions with varying lattice parameters. (a) Representative SEM images (left: control, right: quenched) and histogram of microcrystal edge lengths for 20 nm Au nanoparticles and $n = 0$ DNA (highest Au volume fraction sample). The excess silica from the encapsulation process can be observed around the microcrystals. The control sample is represented with gray bars, and the quenched samples with red bars in the histogram. (b, c) Same data as in (a) for $n = 1$ and 2 samples (decreasing Au volume fractions), respectively. All scale bars: 1 μm .

crystals in solution varies from 3.3 to 1.6 g·cm⁻³. The size distribution of microcrystals and representative SEM images for each sample are presented in **Figure 3.6a-c (Table 3.5)**. In addition to the improved size uniformity for all three PAE crystals through the quenching method, we observe from these results that the average microcrystal size increases with increasing DNA length (decreasing Au fraction), thus supporting that the improvement in uniformity was indeed based on sedimentation-based quenching.

Table 3.4. Calculated Au volume fractions and densities of superlattices depending on n.

Number of Modular Units, n	Volume Fraction of Au (%)	Approximated Density, ρ (g·cm⁻³)
0	12.5	3.3
1	6.96	2.3
2	3.10	1.6

Furthermore, this method is amenable to assemblies of PAEs of various core sizes and compositions (**Figure 3.7**). When different sizes of nanoparticles (10 nm or 40 nm) were used for the microcrystal formation, the uniformity of quenched samples consistently improved, namely the PDI dropped from 0.14 to 0.03 for smaller PAEs (10 nm Au cores with n = 0 DNA linker) and from 0.082 to 0.031 for larger PAEs (40 nm Au cores with n = 2 DNA linker), from control to quenched samples, respectively (**Figure 3.7a-b, Table 3.5**). The generality of this process was observed by utilizing PAEs with spherical Ag cores (n = 1 DNA) where an improvement from in PDI from 0.11 to 0.037 was realized (**Figure 3.7c, Table 3.5**). As the improved uniformity of these crystals relies on the sedimentation of nanoparticle assemblies, this method can be extended to a variety of systems including anisotropic nanoparticle assemblies with different crystal habits.²⁸

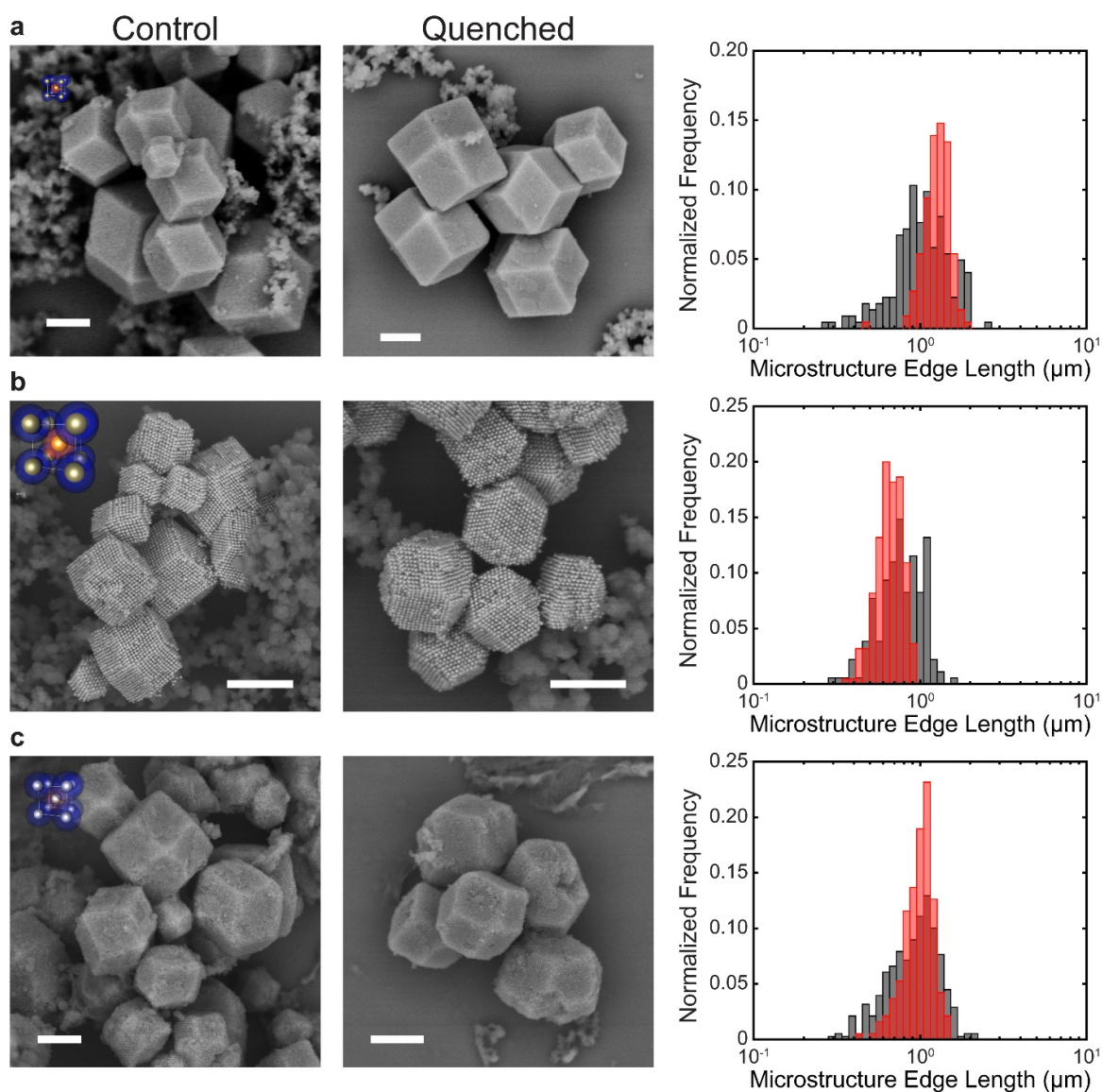


Figure 3.7. Microcrystal size distributions for 10 nm Au, 40 nm Au, and 20 nm Ag nanoparticle assemblies. This quenching technique can be extended to DNA nanoparticle superlattices of varying nanoparticle sizes and compositions. The SEM micrographs of control (left) and quenched (middle) samples, and the histograms (right, gray: control, red: quenched) are represented for (a) 10 nm in diameter Au nanoparticles ($n = 0$ DNA), (b) 40 nm in diameter Au nanoparticles ($n = 2$ DNA), and (c) 20 nm in diameter Ag nanoparticles ($n = 1$ DNA). The excess silica from the encapsulation process can be observed around the microcrystals. All scale bars: 1 μm .

Table 3.5. Tabulated microcrystal size distributions.

Sample	Control				Quenched			
	Counts	Mean Size (L, μm)	Standard Deviation (σ , μm)	PDI	Counts	Mean Size (L, μm)	Standard Deviation (σ , μm)	PDI
20 nm Au n = 0 DNA	211	0.48	0.19	0.16	142	0.61	0.11	0.032
20 nm Au n = 1 DNA	118	1.04	0.38	0.13	189	0.95	0.20	0.044
20 nm Au n = 2 DNA	87	1.29	0.40	0.16	89	1.32	0.26	0.040
10 nm Au n = 0 DNA	190	1.08	0.38	0.14	152	1.27	0.22	0.030
10 nm Au n = 1 DNA	169	1.49	0.57	0.15	223	1.69	0.37	0.047
40 nm Au n = 1 DNA	156	0.58	0.19	0.10	186	0.47	0.095	0.040
40 nm Au n = 2 DNA	182	0.69	0.20	0.082	220	0.57	0.10	0.031
20 nm Ag n = 1 DNA	379	0.96	0.32	0.11	190	1.00	0.19	0.037

3.6 Conclusions

This work is important for two main reasons. First, it provides a general and effective method for arresting crystal growth and significantly narrowing crystal size distributions, and second, it is independent of particle size, composition, and shape,^{18, 21, 28, 127} and therefore, should be extendable to a wide variety of crystal types. Consequently, researchers who are interested in using colloidal crystals to realize important structure-function relationships now have a tool to prepare crystals with uniform size. This level of size control will be essential for many applications, especially in the area of optics.

3.7 Experimental

3.7.1 Materials and Instruments

Spherical Au nanoparticles were purchased from BBI and Ag nanoparticles were purchased from NanoXact. Oligonucleotides were synthesized using an MM48 Automated Oligonucleotide Synthesizer with reagents from Glen Research. Chemicals including NaCl, NaH₂PO₄ and Na₂HPO₄ for pH buffer, SDS, and dextran sulfate sodium salt (from Leuconostoc spp., MW ~ 500,000) were purchased from Sigma Aldrich. Hitachi SU8030 FE-SEM was used for imaging.

The sequence design, synthesis, and purifications of DNA were carried out in a similar manner as discussed in the previous chapter. The sequences used in this study is in **Table 3.7**.

Table 3.6. DNA sequences used in this study.

Thiol-modified DNA strands (for Au nanoparticles)	DNA Sequences (5' → 3')
A anchor	TCA ACT ATT CCT ACC TAC (Spacer 18) ₂ – SH
B anchor	TCC ACT CAT ACT CAG CAA (Spacer 18) ₂ – SH
Dithiol serinol-modified DNA strands (for Ag nanoparticles)	DNA Sequences (5' → 3')
A anchor	TCA ACT ATT CCT ACC TAC (Spacer 18) ₂₀ – DTS
B anchor	TCC ACT CAT ACT CAG CAA (Spacer 18) ₂₀ – DTS
Linker strands	DNA Sequences (5' → 3')
A linker (n = 0, 1, or 2)	GTA GGT AGG AAT AGT TGA (Block modular unit) _n (Spacer 18) TTT CCT T
B linker (n = 0, 1, or 2)	TTG CTG AGT ATG AGT GGA (Block modular unit) _n (Spacer 18) AAG GAA A
Block strands	DNA Sequences (5' → 3')
Block modular unit	(Spacer 18) TTA CTG AGC AGC ACT GAT TT
Block duplex for linkers strands	AAA TCA GTG CTG CTC AGT AA

“Spacer 18” refers to the six ethylene glycol units with modified phosphoramidites, which were manufactured by Glen Research.

3.7.2 Preparation of PAEs and Their Hybridization

3'-propylthiol-terminated DNA anchor strands (Table S1) were added to the citrate-capped Au nanoparticle solution. For Ag nanoparticles, dithiol serinol-terminated DNA strands were used.

The solution was then salt-aged up to 0.5 M NaCl to maximize DNA loading on the nanoparticles. After an overnight incubation, the DNA-functionalized nanoparticles were washed three times with 0.5 M NaCl to remove excess DNA by centrifugation. Respective DNA linkers were then hybridized to the nanoparticles in equivalence (Table S1, 250, 600, and 1200 linkers/particle for 10, 20, and 40 nm nanoparticles, respectively) forming PAEs. Small portions sampled from each of the A and B PAEs with complementary sticky ends were added together to induce hybridization, and the temperature-dependent extinction of the mixed nanoparticle systems was monitored from which the T_m was derived. The hybridization process was carried out in aqueous 0.5 M NaCl with 10 mM PB (pH 7.6) and 0.01% SDS.

3.7.3 Preparation of PAE Microcrystals

A thermocycler (ProFlex PCR System, ThermoFisher) or a water bath equipped with an immersion circulator (AC200, ThermoFisher) was used to slowly cool the PAE solution starting 5 °C above T_m (measured from temperature-dependent extinction) to room temperature at a ramp rate of 0.1 °C every 10 min. Control samples of just the A-B PAEs in 0.5 M NaCl solution were used. To implement the density barrier filtering of these microcrystals, a 10% w/v dextran sulfate solution ($\rho = 1.058 \text{ g}\cdot\text{cm}^{-3}$) was placed beneath the same volume of PAE solution.

3.7.4 Silica Encapsulation of Microcrystals

Upon cooling down to room temperature, the samples were removed from the growth vials and cleaned of excess dextran sulfate (for cases in which it was used) by two rounds of centrifugation. The superlattices were then suspended in a 0.5 M NaCl solution to which N-trimethoxysilylpropyl-N, N, N-trimethylammonium chloride was first added, and triethoxysilane

was added 20 min later. The solution was shaken for over 12 h in a temperature-controlled mixer at 700 rpm, after which the samples were resuspended in water.

3.7.5 Characterization Methods

SEM: PAE microcrystals suspended in water were dropcast onto Si wafers and then imaged with SEM (Hitachi SU-8030 FE-SEM). Quartz PCI software was used to measure the edge lengths of the rhombic dodecahedra from the micrographs. The PDI value was calculated from the standard deviations (σ) and mean size (\bar{L}) for each sample, by $\text{PDI} = \left(\frac{\sigma}{\bar{L}}\right)^2$.

SAXS: These experiments were conducted at the Dow-Northwestern-Dupont Collaborative Access Team (DND-CAT) beamline of the Advanced Photon Source (APS) at Argonne National Laboratory. All of the experiments were conducted with an X-ray wavelength of 1.24 Å (10 keV). The sample angle was calibrated with a silver behenate standard, and two sets of slits were used to define and collimate the beam. Samples were prepared in a 1.5 mm quartz capillary (Charles Supper Company, Inc.) and placed into the sample stage. Exposure times varied from 0.1 to 0.5 s, and scattered radiation was detected with a CCD area detector. One-dimensional radially averaged SAXS data presented with scattering intensity, $I(q)$, as function of the scattering vector, q , was obtained by an azimuthal average of two-dimensional scattering patterns.

$$q = \frac{4\pi \sin \theta}{\lambda} \quad (3.3)$$

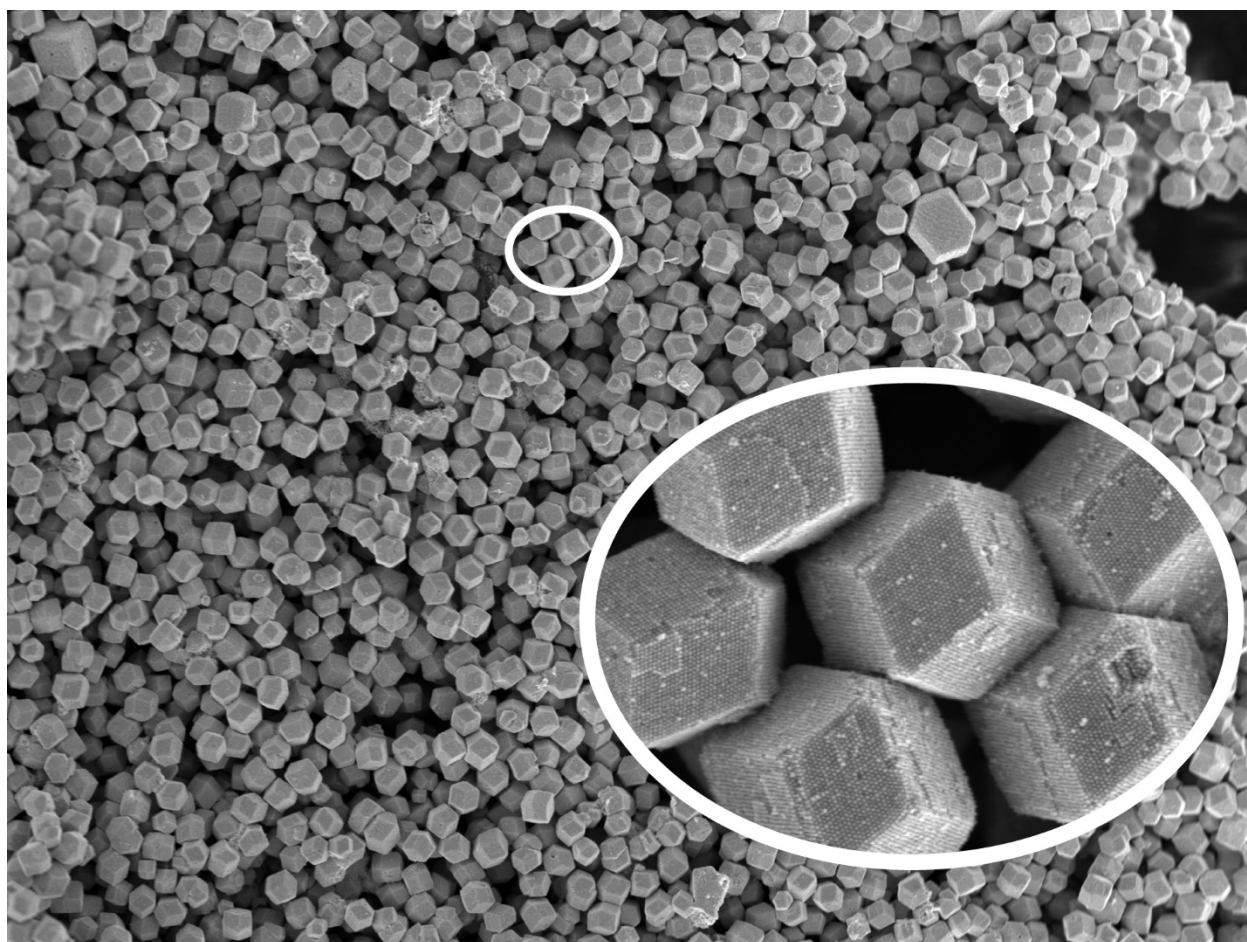
where θ is half of the scattering angle and λ is the wavelength of X-ray radiation. Scattering from the solution, capillary, and DNA were assumed to be negligible due to the orders of magnitude difference in the scattering associated with the Au nanoparticles. The space group assignment ($Im\bar{3}m$ for bcc and $Fm\bar{3}m$ for fcc lattices) and interparticle spacing were determined by comparing

the positions of experimental diffraction peaks to the predicted peaks. The structural parameters of these systems are tabulated in **Table 3.8**.

Table 3.7. Lattice parameters from the SAXS data and calculated Au volume fraction in each microcrystal sample.

Sample	Space Group	Lattice parameter, a = b = c (Å)	Volume fraction of Au (%)
10 nm Au, n = 0 DNA	Im-3m (bcc)	300.84	3.85
10 nm Au, n = 1 DNA	Im-3m (bcc)	419.13	1.42
20 nm Au, n = 0 DNA	Im-3m (bcc)	406.03	12.5
20 nm Au, n = 1 DNA	Im-3m (bcc)	493.75	6.96
20 nm Au, n = 2 DNA	Im-3m (bcc)	646.30	3.10
40 nm Au, n = 1 DNA	Im-3m (bcc)	670.25	22.3
40 nm Au, n = 2 DNA	Im-3m (bcc)	816.48	12.3

Chapter 4 Stabilization of DNA-Engineered Colloidal Crystals



Portions of this chapter have been published¹³⁵ in *Advanced Materials*, doi: 10.1002/adma.201805480.
Co-authors of this work: Sarah S. Park, Chad A. Mirkin
Copyright 2019 John Wiley & Sons, Inc.

4.1 Summary

A post-synthetic method for stabilizing colloidal crystals programmed from DNA has been developed. The method relies on Ag^+ ions to stabilize the particle-connecting DNA duplexes within the crystal lattice, essentially transforming them from loosely bound structures to ones with very strong interparticle links. Such crystals do not dissociate as a function of temperature like normal DNA or DNA-interconnected superlattices, and they can be moved from water to organic media or the solid state, and stay intact. The Ag^+ -stabilization of the DNA bonds is accompanied by a nondestructive $\sim 25\%$ contraction of the lattice, and both the stabilization and contraction are reversible with the chemical extraction of the Ag^+ ions, by AgCl precipitation with NaCl . This synthetic tool is important, since it allows scientists and engineers to study such crystals in environments that are incompatible with structures made by conventional DNA programmable methods and without the influence of a matrix like silica.

4.2 Background

DNA-mediated colloidal crystal engineering is emerging as one of the most powerful ways to deliberately generate and tailor crystal composition, lattice parameter, and habit.^{1, 15-16, 19, 27-28, 125, 136-137} However, such structures are held together by relatively weak linkages that are sensitive to the environment (salt concentration, solvent, and temperature). As a consequence, they typically must be embedded in a matrix, such as silica, before they can be manipulated and studied in the solid state.¹⁰¹ In this chapter, we report a new post-synthetic approach to increase the stability of DNA-interconnected colloidal crystals.

From recent studies, it has been shown that the thermal stability of duplexed oligonucleotides can be increased by the insertion of Ag^+ ions in between the nucleobases.^{106, 138-}

¹⁴⁰ Specifically, Ag^+ ions replace the hydrogen bonds between the base pairs and form coordinate covalent bonds between Ag^+ ions and heterocyclic N atoms. In contrast with other metal ions which form one specific metallo base pair (e.g. $\text{G-Au}^{3+}\text{-C}$ and $\text{T-Hg}^{2+}\text{-T}$),¹⁴¹⁻¹⁴² Ag^+ is less specific and results in a variety of metallo base pairs such as $\text{C-Ag}^+\text{-C}$, $\text{C-Ag}^+\text{-T}$, $\text{C-Ag}^+\text{-A}$, $\text{G-Ag}^+\text{-G}$, $\text{G-Ag}^+\text{-C}$, and $\text{T-Ag}^+\text{-T}$ and is, therefore, a candidate to fully metallize DNA duplex strands.^{107, 139, 143-145} These findings inspired us to explore how Ag^+ -stabilization of DNA could be used to stabilize colloidal crystals made from DNA and DNA-modified nanoparticles, or PAEs,² and potentially eliminate the need for a stabilizing matrix to work with such systems in non-aqueous environments or the solid state.

4.3 Results and Discussions

4.3.1 Stability in Pure Water and in the Solid State

To test our hypothesis, colloidal single crystals of PAEs were synthesized using methods described in the literature for making bcc structures.^{27, 108} Specifically, complementary A and B type PAEs (spherical Au nanoparticles with 20 nm diameters, DNA sequences in **Table 4.3**) were mixed together and slowly cooled in pH-buffered saline (0.5 M NaCl). Through this process, the PAEs crystallize into superlattices and eventually form rhombic dodecahedral (RD) microcrystals. After Cl^- anions were removed by repeated solution exchange with 0.5 M NaClO_4 (aq) to avoid any precipitation with Ag^+ , the RDs were dispersed in 0.5 M AgNO_3 solution, where excess Ag^+ ions compared to the DNA base pairs were present. At this stage, the effect of Ag^+ -stabilization can be observed with the naked eye, since the dark suspension of RDs immediately becomes less opaque upon redispersion (**Figure 4.1b**). This change is caused by the contraction of the DNA particle interconnects, resulting in a reduction of the visible light scattering cross-section of the

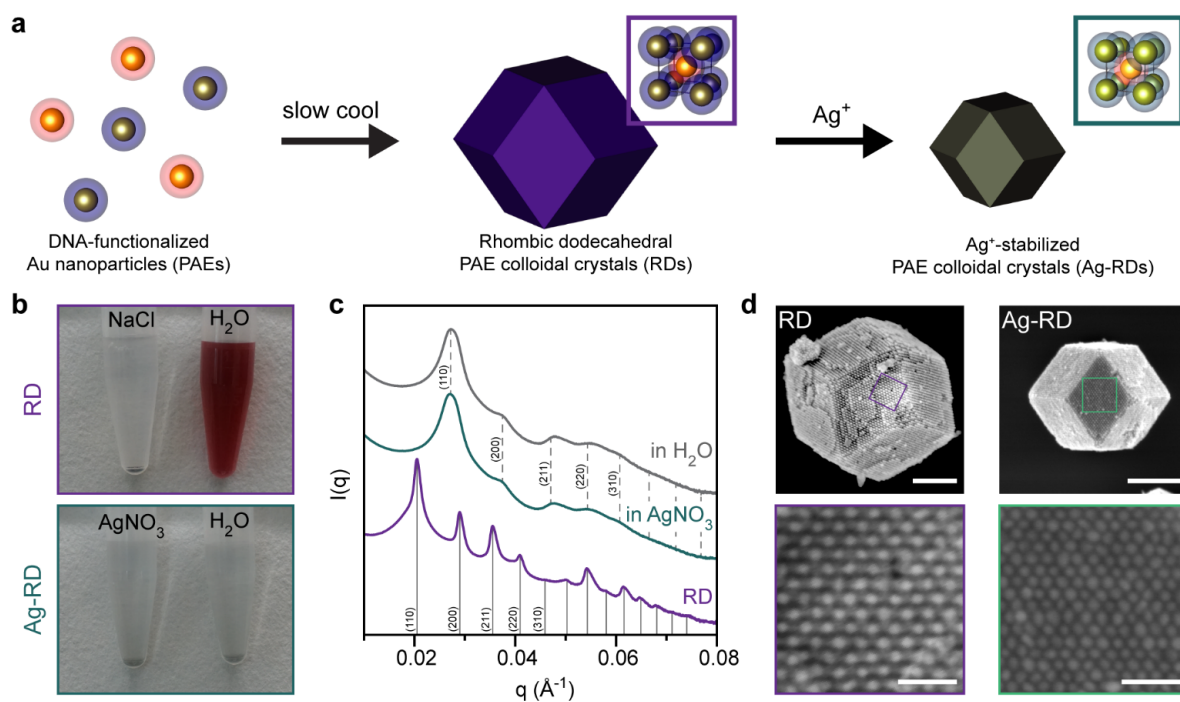


Figure 4.1. (a) Schematic illustrating the synthesis of Ag⁺-stabilized PAE crystals (Ag-RDs). (b) In contrast to unmodified PAE crystals (RDs), which are stable in 0.5 M NaCl but dissociate upon resuspension in pure water, Ag-RDs are stable in water. (c) Radially-averaged one-dimensional SAXS patterns show lattice contraction upon the transformation into Ag-RDs (green) by transferring RDs (purple) to 0.5 M AgNO₃. Ag-RDs are stable in unsalted water (grey). The first five peaks in each pattern were assigned to bcc lattices. (d) SEM micrographs (bottom: high resolution images of (110) facets from the corresponding squares) confirm the nondestructive contraction of RD to Ag-RD while maintaining crystallinity. Scale bars: (top) 500 nm and (bottom) 100 nm.

crystals. SAXS confirms this contraction with peak-shifts to higher q , a consequence of the decrease in lattice parameter (a 25% reduction, **Table 4.2**). This contraction occurs due to a shortening of the metallo-DNA duplex, compared to the metal-free form, which has been crystallographically characterized.¹³⁹ The peak broadening in SAXS that accompanies the Ag^+ addition can be attributed to an increase in lattice strain and reduction in domain size, both of which result from the volume contraction of the colloidal crystals (**Figure 4.1c**).¹⁴⁶⁻¹⁴⁷ SEM also shows that the RDs retain their rhombic dodecahedron crystal habit and bcc lattice symmetry (**Figure 4.1d**). Importantly and remarkably, the Ag^+ -stabilized PAE crystals (Ag-RDs) can be transferred to pure water without them disassembling, something not possible with untreated DNA-interconnected RDs, which disassemble into colloidal suspensions of particles, as evidenced by the formation of a red colloid with a UV-vis signature at 520 nm associated with dispersed 20 nm diameter Au nanoparticles (**Figure 4.1b**).

The structural stability of Ag-RDs in pure water was further verified by SAXS, which showed no peak shift (**Figure 4.1c**). Also, after three cycles of washing with pure water and drying, the lattice symmetry and microscale crystal habit of the Ag-RDs were not significantly affected by the Ag^+ ion-induced transition to the solid state, as evidenced by SEM (note that unlike silica matrix embedding, there is no evidence of impurity-based precipitates, **Figure 4.1d**). Note that an additional 15% reversible decrease in lattice parameters is observed by SAXS with this dehydration process (therefore in total, a 36% contraction from the as-synthesized RDs, **Figure 4.6a** and **Table 4.2**). We attribute the dehydration-induced shrinkage to the polyethylene glycol (PEG) units in the DNA; only a 3.2% contraction, upon dehydration, was observed in the Ag^+ -ion stabilized PAE crystals without the PEG units in the anchor strands (**Table 4.2**). The mean edge lengths of the rhombic dodecahedra PAE crystals, post-stabilization, were measured by solid-state

SEM; for silica-embedded samples,¹⁰¹ the average was determined to be $0.93 \pm 0.16 \mu\text{m}$, while for Ag-RDs, it was determined to be $0.61 \pm 0.09 \mu\text{m}$. These microscopic contraction values correspond well with the lattice parameter changes determined by SAXS (i.e. a 34% decrease for the rhombic dodecahedron edge lengths in SEM and a 36% decrease in the lattice parameters as measured by SAXS, **Table 4.2**).

4.3.2 Molecular Level Characterizations

Further studies were carried out to determine how the addition of Ag^+ enhances the stability of DNA and PAE crystals. The materials analyses, including circular dichroism (CD; **Figure 4.2**), X-ray photoelectron spectroscopy (XPS; **Figure 4.3**), and ICP-OES (**Table 4.1**), complementarily substantiate that Ag^+ ions chemically bind to the DNA. For example, upon Ag^+ addition, conformational changes of the DNA can be observed by CD spectroscopy, as evidenced by the formation of negative bands around 275 nm.¹³⁸⁻¹⁴⁰ In addition, XPS shows a shift of the N 1s peak (N–C–O and N–C=O) to a lower binding energy (401 to 399 eV), a consequence of the increase in the electron density at the N atoms binding to Ag^+ ions.¹⁴⁸

Specifically in ICP-OES, it was found that no excess Ag^+ ions bind to the DNA duplexes; the Ag/base pair values do not exceed 0.45 even if a large excess of Ag^+ was used (**Table 4.1**). This result indicates that, on average, only one or less Ag^+ ion is attached to each base pair, but there still must be a nucleobase-dependence (for example, Ag^+ ions are not likely to bind to A bases). Considering ~60% of A-T contents in the DNA design, arithmetically, most of the C-G pairs may be transformed as metallo base-pairs, whereas the A-T pairs may remain in the Watson-Crick conformation, and minimal amount of Ag^+ may be bound to the backbone.

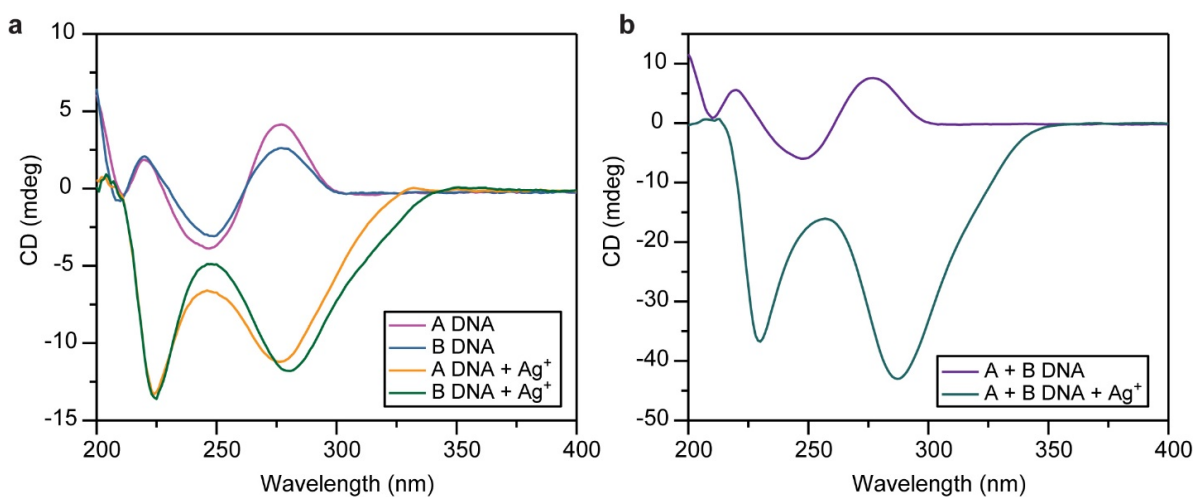


Figure 4.2. CD spectra of (a) A DNA (anchor + linker), B DNA, A DNA with Ag⁺, and B DNA with Ag⁺, and (b) mixture A DNA and B DNA with and without Ag⁺.

Table 4.1. Comparison of mass and molar contents of Ag per base pair from ICP-OES.

Initial Ag (equiv. to base pair)	Measured Ag (equiv. to base pair)	Standard Deviation
0	0.001	0.0007
0.25	0.251	0.0066
0.5	0.393	0.0020
2.5	0.435	0.0069
5	0.319	0.0082
10	0.290	0.0068
200	0.288	0.0543

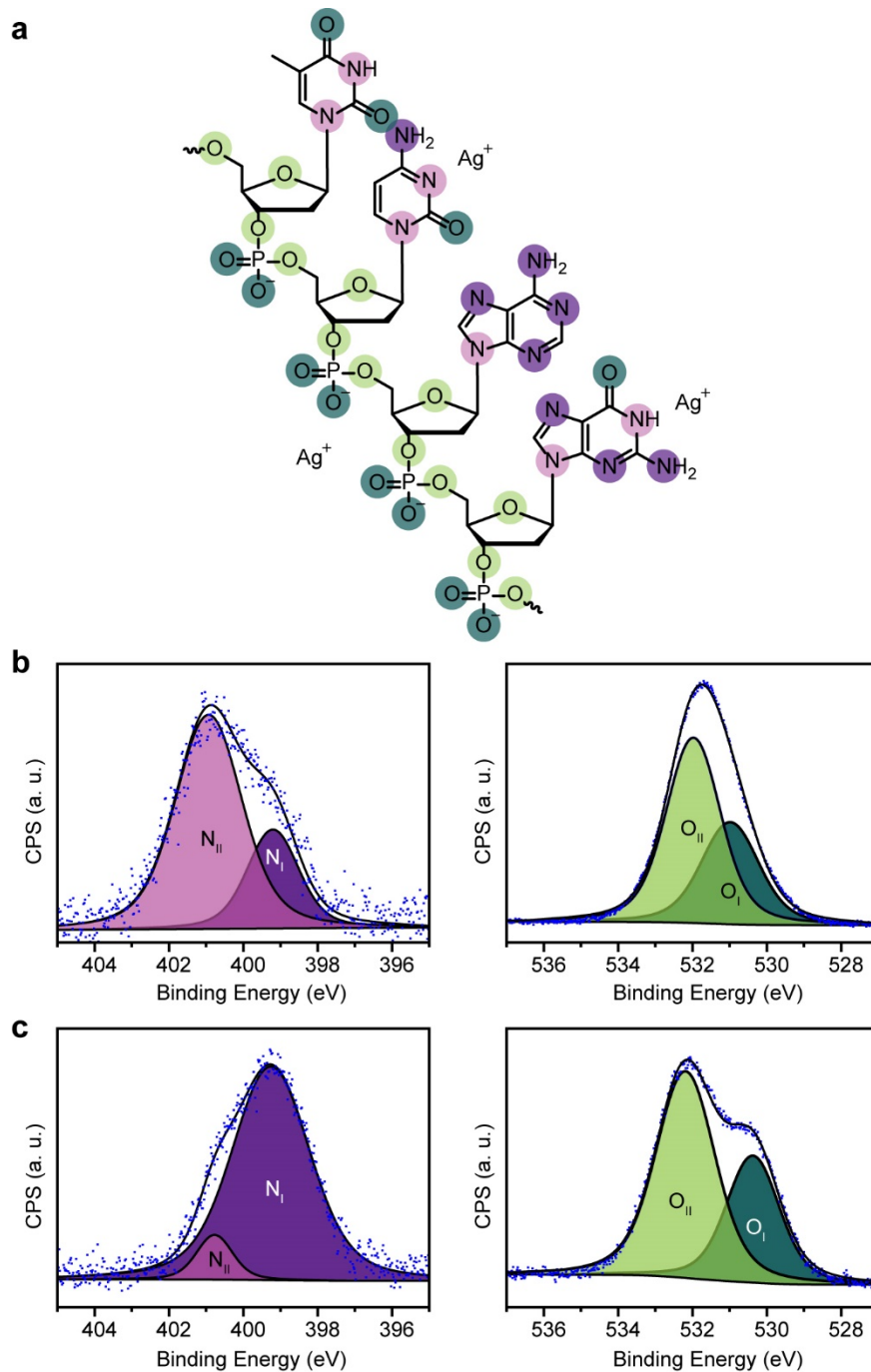


Figure 4.3. (a) Schematic representation of a DNA strand (TCAG). Color representation is correlated to the peak fittings. (b) XPS spectra of RDs at N 1s core level peaks (left) and O 1s core level peaks (right) before Ag^+ -stabilization. (c) Same data for Ag -RDs.

For the XPS analysis, according to Volkov et al.,¹⁴⁸ the core level N 1s peaks of DNA can be decomposed into two peaks depending on their chemical states: N atoms near O (N3 atoms in T or C, and N1 atom in G, N_{II} in the spectrum, **Figure 4.3**) and the others (N_I). Similar to the literature, as a result of the Ag⁺ addition to PAE crystals, an increase in the relative intensities of N_I was observed, suggesting that Ag⁺ binds to a fraction of the heterocyclic N_{II} sites and the peak shifts to N_I. The changes in O peaks possibly indicate that Ag⁺ ions are also adsorbed to the phosphate backbone, but it is difficult to deconvolute them from the background signals from adsorbents on the substrate and to derive a decisive conclusion.

4.3.3 Thermal and Chemical Stability

Not only does Ag⁺ stabilize PAE crystals in pure water, but it also prevents their thermal dissociation. As previously reported, Ag⁺-coordinated base pairs are orders of magnitude stronger than canonical Watson-Crick base pairing.¹³⁸ Indeed, this results in substantially increased DNA bond stability within the crystals. Variable-temperature UV-vis spectroscopy and SAXS confirm this increased stability in water (**Figure 4.4a**). Note that while the untreated RDs melt at 45.5 °C (FWHM \approx 2.5 °C) in aqueous 0.5 M NaCl, the Ag-RDs show no evidence of melting from room temperature to 90 °C (**Figure 4.4a**). Similarly, SAXS confirms that the Ag-RDs show no change in lattice structure in water at 90 °C, whereas the bcc SAXS pattern for the untreated RDs disappears at and above 50 °C. Note the RDs maintain their Wulff shape after heat treatment at 90 °C in water for 1 h (**Figure 4.4a** inset), and even in the solid state after being heated to 200 °C for 5 h (**Figure 4.5**).

Remarkably, the crystalline Ag-RDs were stable in aqueous media over the 5 – 11 pH range and in many organic solvents (acetone, ethanol, and isopropyl alcohol, **Figure 4.4b**), as evidenced

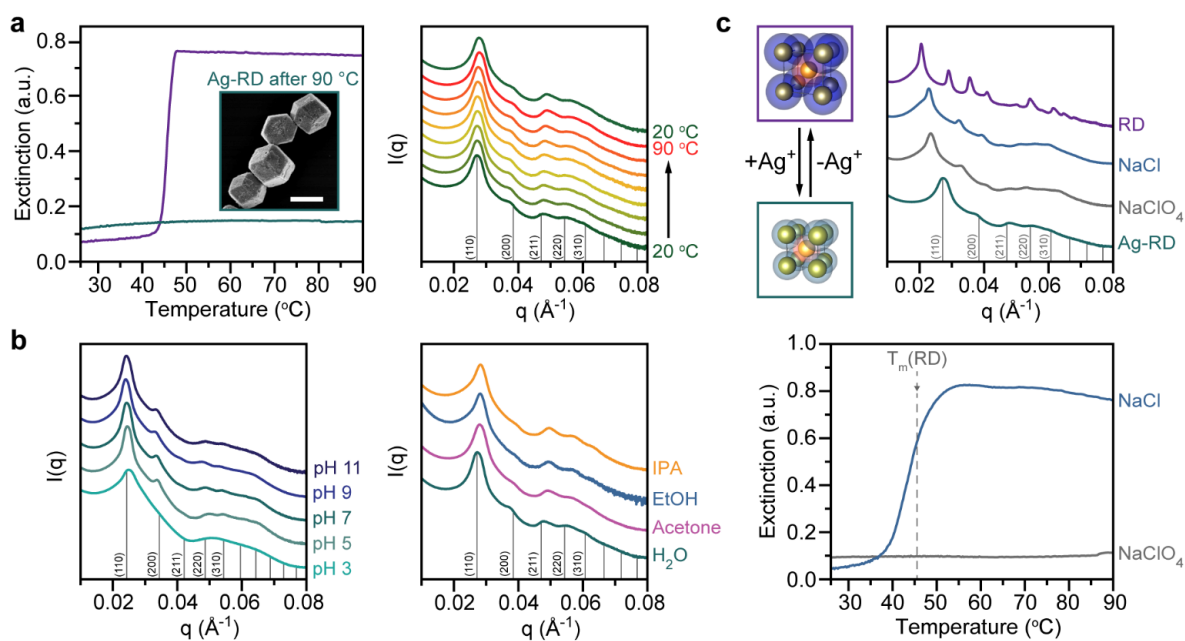


Figure 4.4. (a) Melting curves (left) measured by variable-temperature UV-vis spectroscopy for RDs composed of 20 nm spherical Au nanoparticles suspended in 0.5 M NaCl (purple), and Ag-RDs in water (green). An inset SEM image confirms that the Ag-RDs maintain the Wulff shape after heating at 90 °C. SAXS patterns (right) for Ag-RDs in water do not change over the range of 20 – 90 °C. Scale bar: 1 μm . (b) Ag-RDs can be transferred into variety of pH solutions (left), and acetone (pink), ethanol (blue), isopropyl alcohol (yellow, right) while maintaining their symmetry and lattice parameters. (c) SAXS patterns (top) and variable-temperature UV-vis spectroscopy (bottom) show the reverse reaction from Ag-RD to RD by transferring to 0.5 M NaCl solution. By comparison with NaClO_4 , Cl^- is indeed responsible for the Ag^+ elimination.

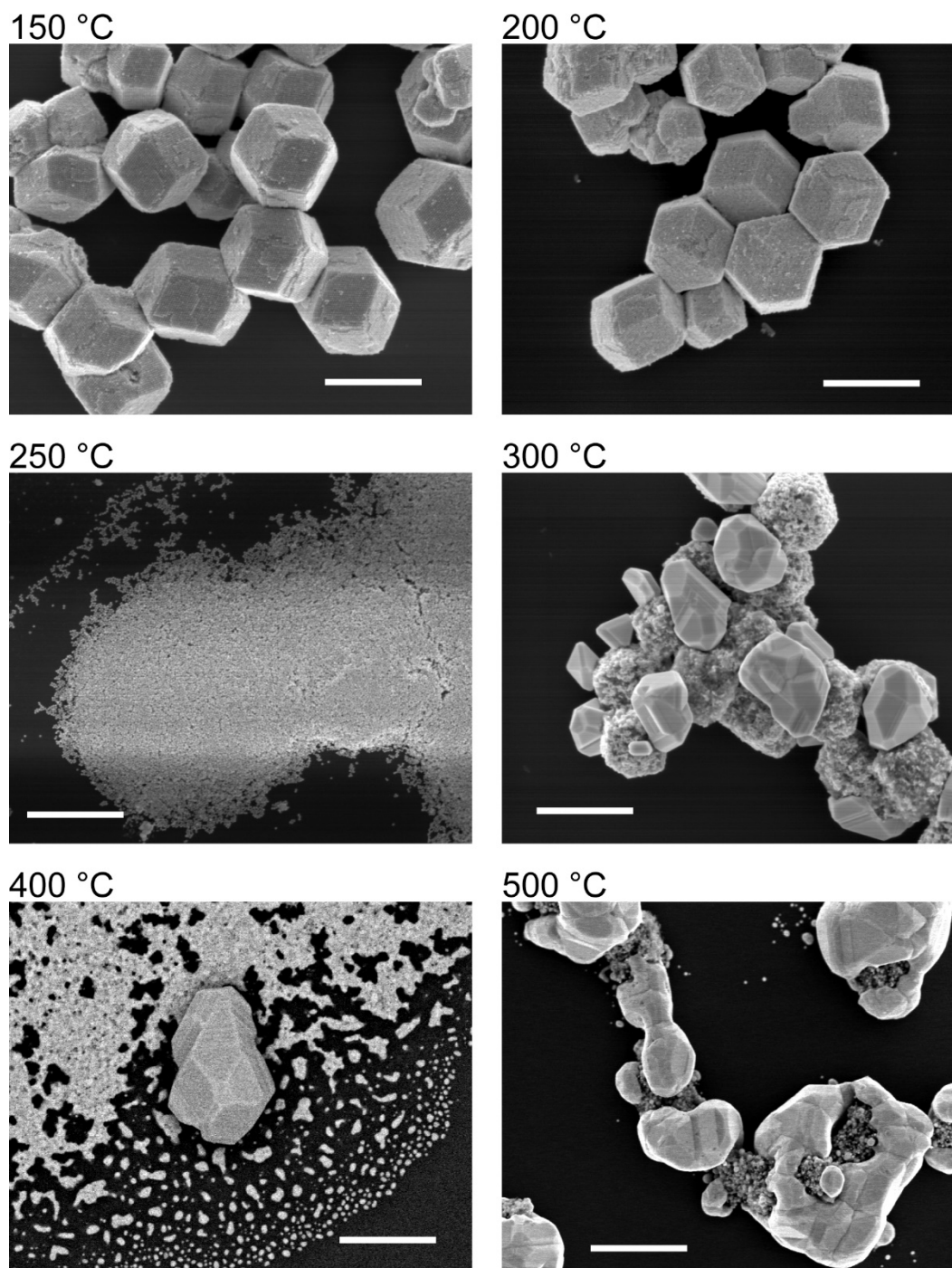


Figure 4.5. SEM images of Ag-RDs after being heated in the solid state under air for 5 h on Si wafers. The Ag-RDs remain intact up to 200 °C. Above 250 °C, the Ag-RDs start breaking and sintering. All scale bars: 1 μm .

by SAXS. The effect of changes in pH were negligible above pH 5, but some peaks broadened at pH 3. At a pH below the pKa of the imino N3 group in cytosine (4.2),¹⁴⁹ H⁺ effectively competes with Ag⁺ for the binding sites (N atoms) in the nucleotide bases.¹⁵⁰ The robust nature and thermal stability of Ag-RDs in the solid state (**Figure 4.5**) will be important as these structures become the basis for device components,^{9, 128} where they must be compatible with conventional lithographic procedures, including heat treatment and exposure to various types of photoresists (organic) and developers (typically basic solutions).¹⁵¹

4.3.4 Reversibility

The reversibility of the Ag⁺-stabilization of PAE crystals was tested by a Cl⁻-induced AgCl precipitation reaction. After two cycles of washing and resuspension in 0.5 M NaCl, SAXS peaks of the Ag-RDs shift to lower q , closer to the peak positions of the original RDs (**Figure 4.4c**), which proves the expansion of the bcc crystal lattices. Importantly, the solution remains colorless indicating that the superlattices do not dissociate during Ag⁺ ion extraction. However, the lattices post-extraction do melt with T_m of 44 °C (FWHM = 8 °C), the value expected for Ag⁺-free PAE crystals. The reversible contraction and expansion by the addition and extraction of Ag⁺ can be repeated at least three times (**Figure 4.6b**). To better understand this recovery process, a control sample was prepared with the Ag-RDs washed and re-dispersed in 0.5 M NaClO₄, which contains the same amount of Na⁺ ions but anions that do not react with the Ag⁺ in the superlattices. A similar but relatively modest shift of the SAXS peaks to lower q was observed, but interestingly, such crystals do not thermally decompose, even at 90 °C (**Figure 4.4c**).

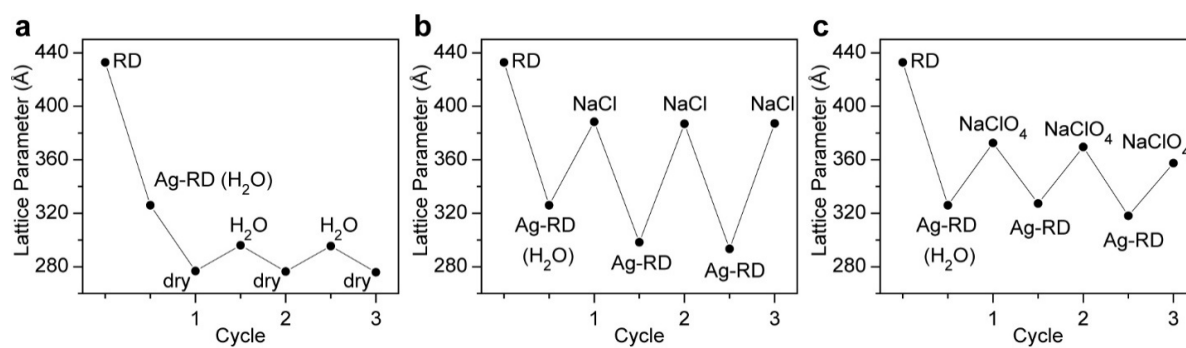


Figure 4.6. Change in lattice parameters as a function of (a) dehydration, (b) addition of 0.5 M NaCl, and (c) addition of 0.5 M NaClO₄ over three cycles. The lattice parameters were calculated from SAXS measurements.

4.3.5 Other PAE Systems

To test the generality of the Ag^+ -stabilizing process, we studied PAE superlattices with different lattice parameters, symmetries, and core sizes. Specifically, we examined three different PAE systems: (1) one with a bcc lattice symmetry but greater lattice spacing (**Table 4.2**), (2) one with a fcc lattice symmetry, and (3) a bcc superlattice composed of smaller PAEs (10 nm diameter core). All three cases, consistent with the earlier results, showed the conservation of lattice symmetries with reduced lattice parameters, and could be stably transferred into water without salt, and eventually to the solid state for SEM (**Figure 4.7**). Furthermore, by combining this method with density-based filtering,¹⁰⁸ it is possible to obtain a large batch of uniform and pure colloidal crystals in powder form (**Figure 4.8**).

4.4 Conclusions

In conclusion, we have developed a general method for stabilizing colloidal crystals made with DNA by integrating Ag^+ ions into their DNA bonds. Crystals treated in this manner can be studied and manipulated in media and at temperatures typically incompatible with such materials, and therefore, this technique will increase the scope of their utility, especially in the areas of optics, catalysis, electronics, and other applications where the pristine crystal habit and crystal symmetry are critical for device performance.^{9, 12, 115, 128, 152}

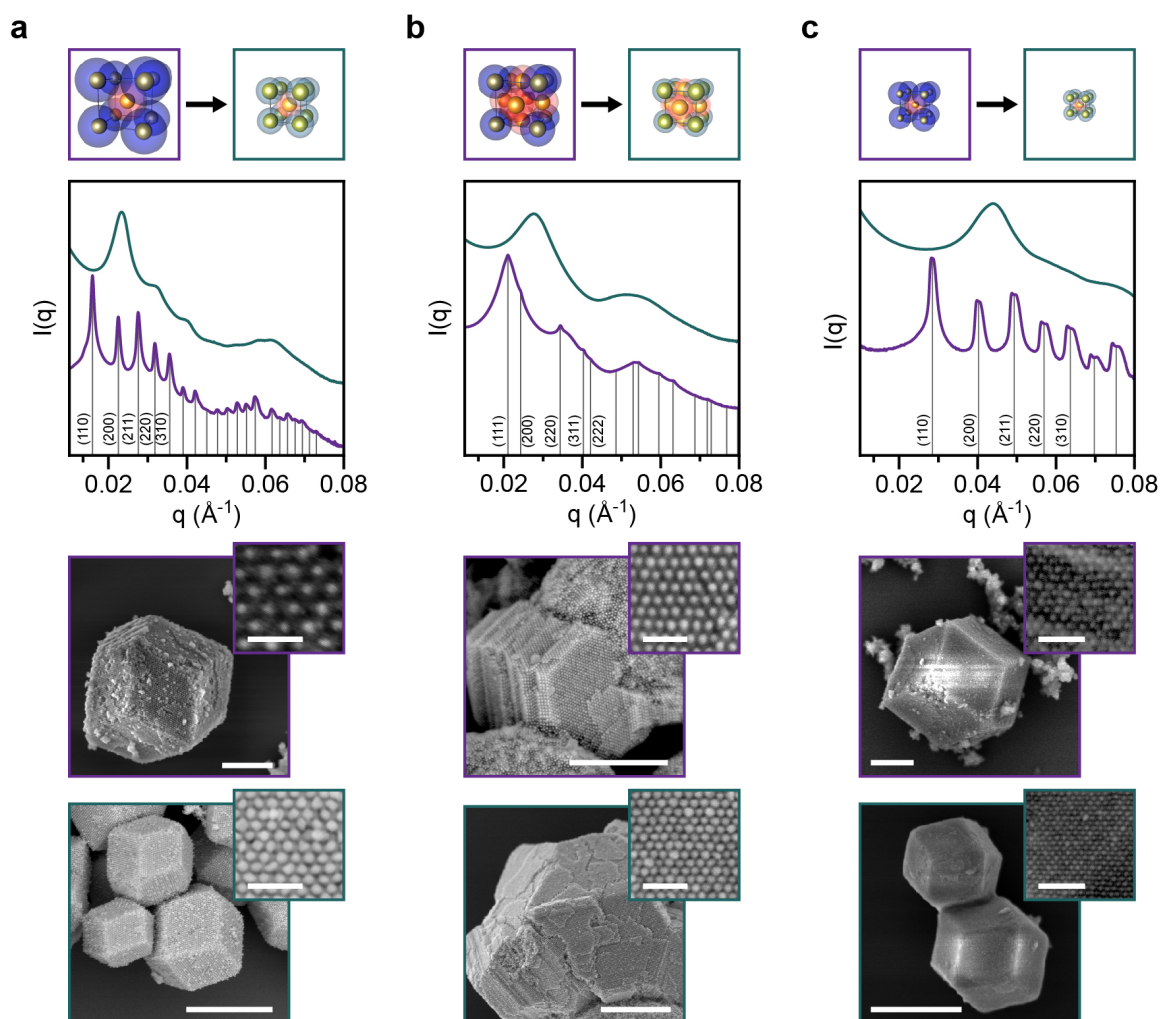


Figure 4.7. Schematics for the unit cells, radially averaged one-dimensional SAXS patterns, and SEM images of untreated PAE crystals (purple) and Ag⁺-stabilized PAE crystals (green). (a) bcc superlattice of 20 nm nanoparticles with longer DNA linkers (**Table 4.3**), (b) fcc superlattice of 20 nm nanoparticles, and (c) bcc superlattice of 10 nm nanoparticles. Scale bars: 1 μm and 100 nm for insets.

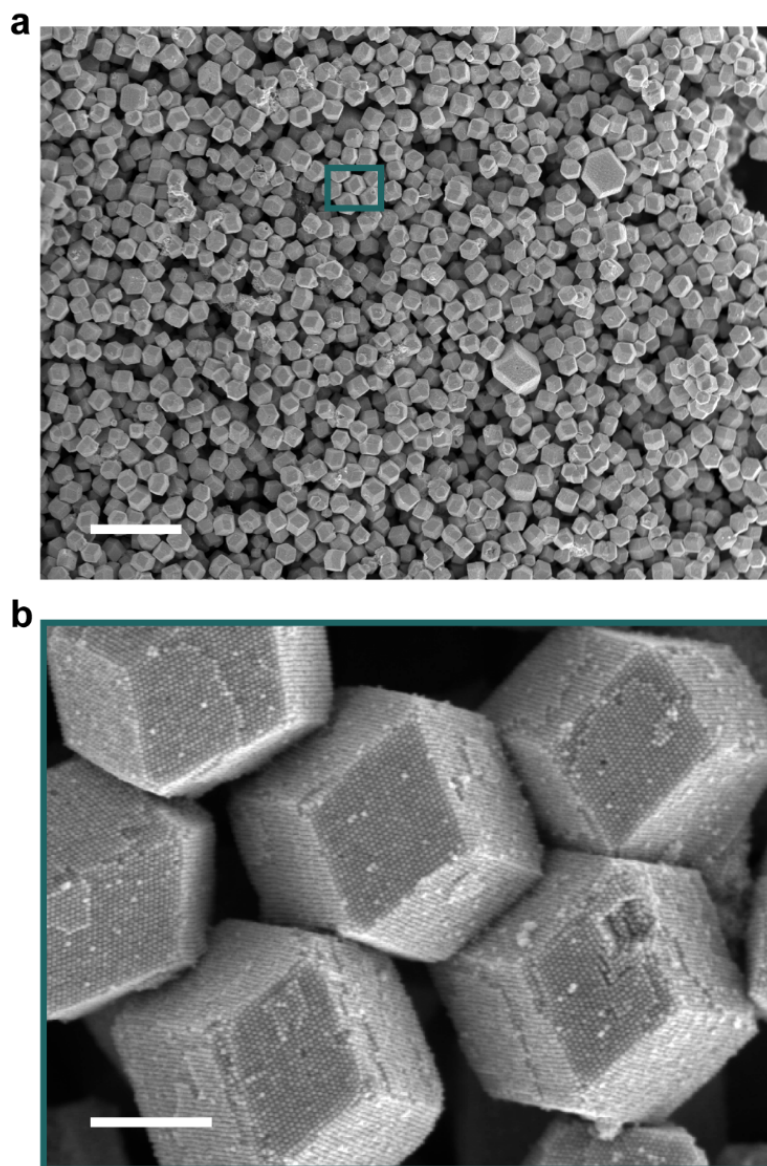


Figure 4.8. (a) Large-scale synthesis (> mg) of rhombic dodecahedral PAE crystals in uniform and pure powder form. (b) A magnified image of the highlighted area in panel a. Scale bars: (a) 5 μm and (b) 500 nm.

Table 4.2. Experimental conditions and lattice parameters determined from SAXS.

Particle size (nm)	DNA	Ag ⁺	Solution	Space group	Lattice parameter (Å)
20	Normal A-B	no	NaClO ₄	<i>Im</i> $\bar{3}$ <i>m</i>	432.97
20	Normal A-B	no	acetone	<i>Im</i> $\bar{3}$ <i>m</i>	284.58
20	Normal A-B	no	IPA	<i>Im</i> $\bar{3}$ <i>m</i>	282.56
20	Normal A-B	no	ethanol	<i>Im</i> $\bar{3}$ <i>m</i>	282.13
20	Normal A-B	no	pH3	N/A	N/A
20	Normal A-B	no	pH5	<i>Im</i> $\bar{3}$ <i>m</i>	431.46
20	Normal A-B	no	pH7	<i>Im</i> $\bar{3}$ <i>m</i>	431.27
20	Normal A-B	no	pH9	<i>Im</i> $\bar{3}$ <i>m</i>	433.86
20	Normal A-B	no	pH11	N/A	N/A
20	Normal A-B	no	NaClO ₄	<i>Im</i> $\bar{3}$ <i>m</i>	435.32
20	Normal A-B	no	dry	N/A	N/A
20	Longer A-B	no	NaClO ₄	<i>Im</i> $\bar{3}$ <i>m</i>	557.95
20	Self-complementary	no	NaClO ₄	<i>Fm</i> $\bar{3}$ <i>m</i>	517.26
10	Normal A-B	no	NaClO ₄	<i>Im</i> $\bar{3}$ <i>m</i>	312.12
20	Normal A-B	yes	AgNO ₃	<i>Im</i> $\bar{3}$ <i>m</i>	326.20
20	Normal A-B	yes	H ₂ O	<i>Im</i> $\bar{3}$ <i>m</i>	327.23
20	Normal A-B	yes	acetone	<i>Im</i> $\bar{3}$ <i>m</i>	316.01
20	Normal A-B	yes	IPA	<i>Im</i> $\bar{3}$ <i>m</i>	314.05
20	Normal A-B	yes	EtOH	<i>Im</i> $\bar{3}$ <i>m</i>	314.68
20	Normal A-B	yes	pH3	<i>Im</i> $\bar{3}$ <i>m</i>	353.56
20	Normal A-B	yes	pH5	<i>Im</i> $\bar{3}$ <i>m</i>	361.28
20	Normal A-B	yes	pH7	<i>Im</i> $\bar{3}$ <i>m</i>	362.73
20	Normal A-B	yes	pH9	<i>Im</i> $\bar{3}$ <i>m</i>	369.31
20	Normal A-B	yes	pH11	<i>Im</i> $\bar{3}$ <i>m</i>	364.90
20	Normal A-B	yes	NaCl	<i>Im</i> $\bar{3}$ <i>m</i>	388.44
20	Normal A-B	yes	NaClO ₄	<i>Im</i> $\bar{3}$ <i>m</i>	373.06
20	Normal A-B	yes	dry	<i>Im</i> $\bar{3}$ <i>m</i>	276.65
20	Longer A-B	yes	H ₂ O	<i>Im</i> $\bar{3}$ <i>m</i>	381.63
20	Self-complementary	yes	H ₂ O	<i>Fm</i> $\bar{3}$ <i>m</i>	390.29
10	Normal A-B	yes	H ₂ O	<i>Im</i> $\bar{3}$ <i>m</i>	201.6
20	anchors without PEG	no	NaClO ₄	<i>Im</i> $\bar{3}$ <i>m</i>	390.08
20	anchors without PEG	yes	AgNO ₃	<i>Im</i> $\bar{3}$ <i>m</i>	317.61
20	anchors without PEG	yes	H ₂ O	<i>Im</i> $\bar{3}$ <i>m</i>	316.06
20	anchors without PEG	yes	dry	<i>Im</i> $\bar{3}$ <i>m</i>	306.05

4.5 Experimental

4.5.1 Materials

Au nanoparticles were purchased from BBI via Ted Pella, Inc., and reagents for DNA synthesis were purchased from Glen Research. Chemicals, including NaCl, AgNO₃, NaClO₄, NaH₂PO₄, Na₂HPO₄, and SDS were purchased from Sigma-Aldrich. Milli-Q® water was used in all aqueous solutions.

The sequence design, synthesis, and purifications of DNA were carried out in a similar manner as discussed in the previous chapter. The sequences used in this study is in **Table 4.3**.

Table 4.3. DNA sequences used in this work.

DNA Description	DNA Sequence (5' to 3')
A Anchor	TCA ACT ATT CCT ACC TAC (Spacer 18) ₂ – (CH ₂) ₃ SH
A Linker	GTA GGT AGG AAT AGT TGA (Spacer 18) TTT CCT T
B Anchor	TCC ACT CAT ACT CAG CAA (Spacer 18) ₂ – (CH ₂) ₃ SH
B Linker	TTG CTG AGT ATG AGT GGA (Spacer 18) AAG GAA A
Long A Linker	GTA GGT AGG AAT AGT TGA (Spacer 18) TTA CTG AGC AGC <u>ACT GAT TT</u> (Spacer 18) TTT CCT T
Long B Linker	TTG CTG AGT ATG AGT GGA (Spacer 18) TTA CTG AGC AGC <u>ACT GAT TT</u> (Spacer 18) AAG GAA A
Self-Complementary A Linker	GTA GGT AGG AAT AGT TGA (Spacer 18) GCG C
Duplexer for Block modular unit	AAA TCA GTG CTG CTC AGT AA

“Spacer 18” refers to the six ethylene glycol units with modified phosphoramidites, which were manufactured by Glen Research.

4.5.2 Functionalization of Nanoparticles with DNA

Au nanoparticles were functionalized with 3'-propylthiol-terminated oligonucleotides using literature procedures.⁹⁸ Briefly, thiolated oligonucleotides (Table S1) were treated with a 100 mM solution of dithiothreitol (DTT) in 0.17 M PB (pH = 8) for 1 h to deprotect the thiol terminals. Residuals from the deprotection reaction and excess DTT were removed with NAPTM-

10 size exclusion columns (GE Healthcare). 30 mL of a commercial stock solution of citrate-capped 20 nm nanoparticles was incubated with these DNA (30 OD) for 3 h at room temperature. PBS (pH = 7.4) and SDS were added to the solution, and aqueous 2 M NaCl was added gradually over 3 h until the final concentrations of PB, SDS, and NaCl were 10 mM, 0.01%, and 0.5 M, respectively. After 12 h, each nanoparticle solution was centrifuged (21,000 rcf) three times to remove excess DNA, with the supernatant removed each time. The particles were resuspended in 1 mL of 0.01 M PBS (pH = 7.4), 0.5 M NaCl, and 0.01 wt % SDS. The concentration of each particle solution (A and B) was approximately 500 nm, quantified by UV-vis spectroscopy using known extinction coefficients for Au particles from the Ted Pella, Inc.

4.5.3 Superlattice Assembly

Rhombic dodecahedral PAE colloidal crystals (bcc lattice symmetry) were assembled by slowly cooling a solution of A- and B-type DNA-functionalized nanoparticles (5 nm each) with the respective DNA linker strands (3 μ M each, Table S1), 0.01 M PB (pH = 7.4), 0.5 M NaCl, and 0.01 wt% SDS. A density-based filtering method was used to enhance the uniformity of the PAE crystals;¹⁰⁸ a 10% w/v dextran sulfate aqueous solution ($M_r = 500000 \text{ g mol}^{-1}$, $\rho = 1.058 \text{ g cm}^{-3}$) was placed beneath the same volume of the PAE solution before the slow-cooling process. During the slow-cooling, the density barrier keeps the free PAEs in the top layer from diffusing into the heavier dextran sulfate solution, and the sublayer captures only the sedimenting PAE crystals and quenches their growth.

4.5.4 Preparation of PAE Crystals Stabilized with Ag⁺

The assembled superlattices were washed three times with aqueous 0.5 M NaClO₄ containing 0.01 wt % SDS (this solution does not form precipitates with Ag⁺ cations). To stabilize the microcrystals, 0.5 M aqueous AgNO₃ was rapidly added to the tube containing the superlattices, and the mixture was incubated for 12 h at room temperature to ensure complete reaction. Alternatively, qualitatively similar results could be obtained by heating at 90 °C for 5 min, instead of waiting for 12 h. Finally, the Ag⁺-stabilized superlattices were washed three times with water, prior to exposing them to different conditions.

4.5.5 Silica Encapsulation of PAE Crystals

Prior to developing the method reported herein, a sol-gel process was used for embedding PAE crystals in silica.¹⁰¹ Such structures can be imaged by SEM without significantly perturbing them. We prepared the matrix-embedded structures for comparison purposes with the Ag⁺-stabilized architectures. Briefly, 400 μL aliquots of PAE crystal samples were diluted with 0.01 M PB (pH = 7.4), 0.5 M NaCl, and 0.01 wt % SDS to a total 1 mL volume. 2 μL of *N*-trimethoxysilylpropyl-*N,N,N*-trimethylammonium chloride (50% in methanol, Gelest, Inc.) was added, and the vessel was placed on a shaker at 700 rpm for 20 min. Then, 4 μL of triethoxysilane (Sigma-Aldrich) was added, and the solution was placed on a shaker (700 rpm) for 12 h at room temperature. The samples were washed three times and the silica-encased structures were collected each time by centrifugation (10 s, 10000 rpm), followed by removal of the supernatant and resuspension in 1 mL nanopure water.

4.5.6 Characterization Methods

SEM and SAXS: Very similar methods and experimental parameters were used as described in the previous chapter.

Variable-temperature UV-vis experiments: For melting experiments, 1 mL of each sample (total PAE concentration = 1 nM) was loaded in a quartz cuvette with a small cavity at the bottom for a magnetic stir bar. UV-vis spectra were collected at 520 nm for the Au nanoparticles and 260 nm for the DNA on a Varian Cary 5000 UV-vis spectrometer, with the sample stage being heated from 25 to 65 °C (or to 90 °C for Ag⁺-stabilized crystals) at 0.1 °C min⁻¹. The temperature was regulated with a Peltier heat pump attached to a six-cell holder, and the samples were tightly capped and continuously stirred throughout the experiment to facilitate thermal diffusion and to ensure the suspension of assemblies in the beam path.

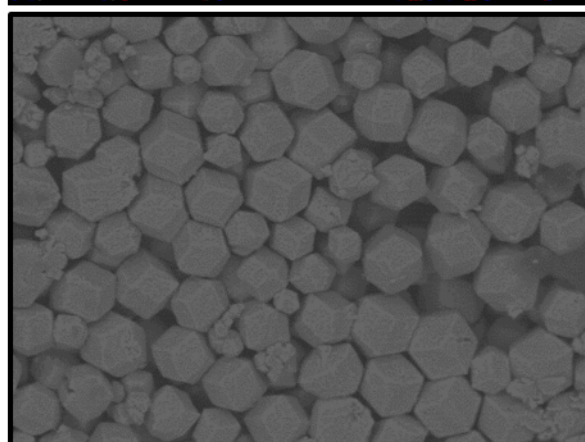
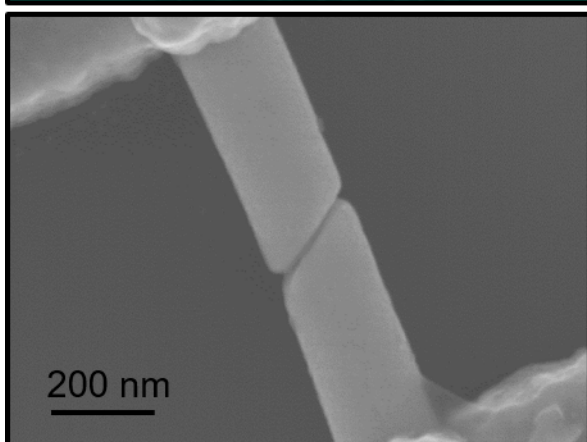
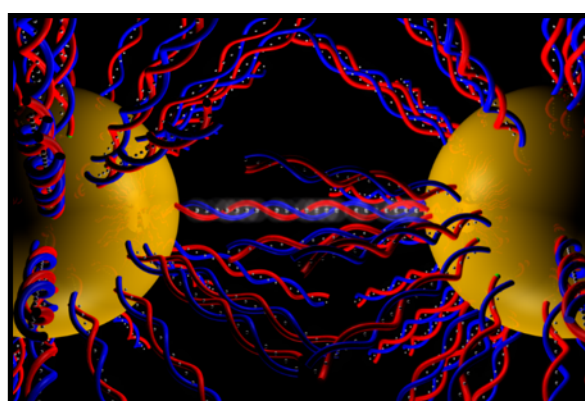
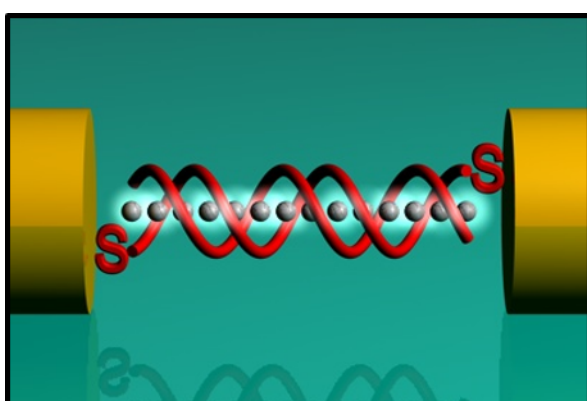
ICP-OES: The P, Ag, and Au content in the DNA was quantitatively measured by ICP-OES (iCAP 7600, Thermo Scientific) at the NU Quantitative Bio-element Imaging Center (QBIC). After the addition of AgNO₃ aqueous solution and incubation at 90 °C for 5 min, the samples were purified by NAPTM-5 size exclusion columns to remove the residual Ag⁺ ions and other smaller entities. Then, the Ag⁺-incorporating DNA samples were digested by sonication in concentrated acid solution (HNO₃ and HCl) for 1 h, followed by incubation at 55 °C for 12 h. Before the measurement, the samples were diluted so the acid concentration was 3% HNO₃ and 2% HCl. Standards were prepared from analytical standard solutions purchased from Sigma-Aldrich.

CD: CD spectra of the free DNA strands with or without Ag⁺-stabilization were recorded between $\lambda = 200 - 400$ nm on Jasco J-1700 circular dichroism spectrometer at room temperature. The samples were prepared as aqueous solutions with 10 μ M of the DNA in 5 mM 3-(*N*-morpholino)propanesulfonic acid (MOPS) buffer (pH = 7.0) and 2 mM NaCl (or NaClO₄ for

samples containing silver), and either 0 or 4 equivalents of AgNO_3 to the number of base pairs was added to each sample. The measurements were performed after incubation at $90\text{ }^\circ\text{C}$ for 5 min and cooling down to room temperature over 1 h.

XPS: XPS (ESCALAB 250Xi, Thermo Scientific) was carried out on PAE crystals. Ag^+ -stabilized PAE crystals were prepared following the method described above, and a control sample without Ag^+ was washed with $0.5\text{ M NH}_4\text{CH}_3\text{COO}$ three times. Each sample was dropcast onto a highly oriented pyrolytic graphite (HOPG) substrates, and dried under vacuum for 24 h, before the XPS measurements.

Chapter 5 Metallo-DNA as Conductive Interconnects for Nanoparticles



5.1 Summary

Despite being a decent (virtually ideal) structural surface ligands for nanoparticle assembly, DNA has been overlooked as device components for electronics and photocatalysis, mainly due to the relatively poor charge transport behavior. In this chapter, the techniques introduced in the previous chapters are combined to synthesize and electrically characterize Ag^+ -mediated DNA and colloidal crystals, to examine the possibility for the Ag^+ -DNA complexes to become conductive nanoparticle interconnects as molecular wires. The Ag^+ -mediated DNA and colloidal crystals exhibited orders of magnitude higher electric conductance than their unmetallized counterparts.

5.2 Background

5.2.1 Nanoparticle-Based Devices

Pioneered by Murray and Kagan,¹⁵³ the self-assembly of mono-, binary-, and tertiary-nanoparticle superlattices^{7, 118, 154-156} has drawn a huge attention and pointed towards nanoparticle-based optical and electronic devices. The two-dimensional superlattices can be characterized as metallic conductors, semiconductors, or insulators depending on the type of nanoparticle building blocks, and the combination of such layers enabled the realization of functioning devices such as field-effect transistors composed only of nanoparticles and their ligands.¹¹⁵ Upon the discussion throughout the previous chapters regarding the DNA-based methods that have demonstrated superior attributes for programmed nanoparticle assemblies and colloidal crystallization, the question arises: how such structures of great structural programmability can be used for applications in electronics and photocatalysis.

There have been attempts to realize nanoparticle-based optoelectronic and photocatalytic devices by means of DNA-mediated approach. In typical systems, researchers co-assembled two

different types of semiconducting nanoparticles with by DNA-based strategies (but not specifically in periodic structures), such that the photoexcitation of the one component enhances the catalytic activities of the other part, for example, water splitting or CO₂ reduction.¹⁵⁷⁻¹⁶¹ However, although the binary system exhibited enhanced catalytic activities, they found that the charge and energy transports through DNA was not so efficient as they initially designed. This could be improved by the incorporation of charge hopping sites, suggesting that the conductive structural scaffolding would become the ideal device architectures for these applications. This finding highlights the importance of charge transport efficiency through DNA for the DNA-assembled superstructures to be used in the fields.

5.2.2 Metal-DNA Complexes

Metallization of DNA strands has been studied based on the motivations of building conductive molecular or nanostructures. Since the earlier works in late 1990s and early 2000s,^{41, 162-163} researchers have fully metallized DNA strands where metallic nanowires with diameters of few tens of nanometers can be synthesized.¹⁶⁴⁻¹⁶⁵ These nanowires were indeed metallic conductors exhibiting high electric and thermal conductivities that are comparable to the values for bulk metals,¹⁶⁴ but could not be categorized as molecular wires due to the dimensions similar to the sizes of colloidal nanoparticles. As mentioned in the previous chapter, the formation of metallo DNA complex compounds has been of vast attention recently, featuring the formation of metal-nucleobase complex compounds, and for specific cases, linear ionic chains in the DNA via metallophilic (e.g. argentophilic) interactions.^{145, 166} Due to the relatively short inter-metal distances in the ranges of 2 – 3 Å and possible band formation, these systems are promising to become the bases for molecularly thin conductive wires.¹⁶⁷

A recent literature studied Pd-mediated DNA strands between Au nanoparticles to demonstrate such idea. The authors built Au nanoparticle dimers interconnected by DNA and reinforced the DNA with Pd²⁺ ions (some of the samples were further reduced to metal nanoclusters).¹⁶⁸ Optical properties of such dimer, namely localized surface plasmon, was used as a measure of interparticle charge conduction as the plasmonic coupling is highly dependent upon the conductivity of particle-connecting media. It was inferred in the study that the reduced metallic nanoclusters (or in their complex ion state) can be hopping sites that promote the charge conduction between nanoparticles. A similar effect can be expected in the Ag⁺-mediated DNA systems and Ag⁺-stabilized colloidal crystals introduced in the previous chapter.

5.3 Results and Discussions

5.3.1 Conductivity of Ag-DNA Measured by Nanogap Devices

To directly measure the conductivity of Ag⁺-DNA, we constructed OWL-based molecular junctions interconnected by DNA as described in Chapter 2 (**Figure 5.1a**). Briefly, Au-Ni-Au nanowires (100 nm diameter) were synthesized with templated electrochemical methods, with the thickness of the sacrificial Ni layer being ~10 nm. The nanowires were then released into suspension, washed, and then, spread by dropcast onto a thermally oxidized Si chip (oxide thickness = 500 nm) with prepatterned Au/Cr electrodes. E-beam lithography was used to connect the wires to the electrodes. The Au surfaces were passivated with the formation of MHA SAM in 10 mM ethanolic MHA ethanolic for 12 h. The Ni layers were removed in 3% aqueous FeCl₃ for 3 h, and the formation of open circuit was confirmed electrically. The chip with broken junctions was then incubated at room temperature for 12 h in 0.5 M NaCl solution (10 mM PB pH 7.6) containing 10 μM DNA with both 3'-propylthiol and 5-hexylthiol termini (37-mer, **Table 5.1**).

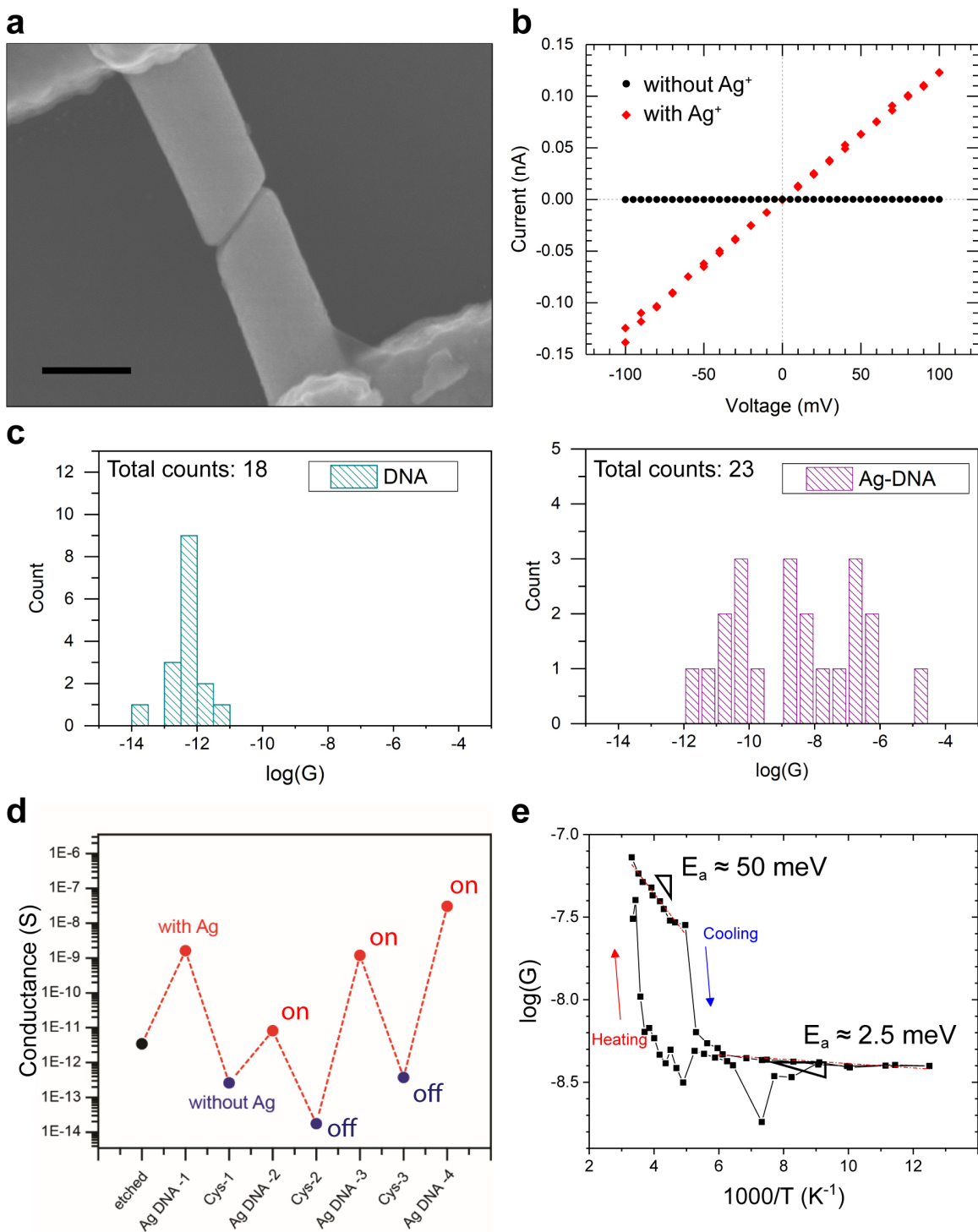


Figure 5.1. (a) A representative SEM micrograph for gapped device. (b) I-V characteristics of a DNA-interconnected device with/without Ag^+ . Scale bar: 200 nm (c) Binned conductivity (\log) data, without Ag^+ (extraction by cysteine, left) and with Ag^+ (right). (d) On-off switching of conductance by Ag^+ -mediation and extraction. (e) Arrhenius plot (Eqn 5.2) recorded by variable-temperature I-V measurement.

The sequence was designed from 12-mer sequence reported to form arrays of linear Ag^+ chains in the core of DNA double helices, where the three repeating units of the 12-mer is self-complementary with six C-C mismatches. These C-C mismatches were supposed to initiate Ag^+ -insertion as reported in literature. Then, the chip was washed three times with saline solution to remove nonspecifically adsorbed DNA strands and incubated at 90 °C for 5 min in 10 mM aqueous AgNO_3 to form Ag^+ -mediated DNA in the molecular junctions. The incubation batch was slowly cooled to room temperature and the chip was washed with water and dried with N_2 .

The electrical measurement was carried out under vacuum ($\sim 10^{-6}$ Torr) after 12 h of storage in the vacuum probe station. 11 devices out of 14 (remaining of which formed short circuits or gave no detectable signal) showed linear I-V characteristics with varying conductance values. For example, the current flow through one of the gap devices was measured to be ~ 0.15 nA at 0.1 V with a linear I-V characteristics, giving conductance values of 1.6×10^{-9} S from the slope (**Figure 5.1b**). The device-to-device variation was perhaps caused by the number of bridging strands, variation in gap spacings, and/or the yield of Ag^+ -DNA formation. To verify the effect of Ag^+ , Ag^+ ions were extracted from the DNA strands by chelating Ag^+ ions in 10 mM cysteine solution. The conductance of this device was significantly reduced to 2.6×10^{-13} S, and the on-and-off switching with orders-of-magnitude changes in conductance by the insertion and extraction of Ag^+ was observed. The conductance values of the 11 devices were recorded during the switching and binned to highlight the increase in conductance (**Figure 5.1c,d**).

For further characterization, variable-temperature I-V characteristics was measured in a temperature-controlled cryogenic probe station from 300 K to 80 K, and then back to 300 K. The temperature dependence data was formulated into Arrhenius plot (**Figure 5.1e**):

$$G = A \exp\left(-\frac{E_a}{kT}\right) \quad (5.1)$$

and

$$\log(G) = -\frac{\log(e) \cdot E_a}{k} \cdot \frac{1}{T} + \log(A) \quad (5.2)$$

where G is the conductance, T is the temperature, E_a is the activation energy, k is the Boltzmann constant, and A is a constant. The plot showed two linear regions with different slopes from which the activation energies for charge conduction were calculated to be ~ 50 meV at high temperature range (200 – 300 K) and ~ 2.5 meV at low temperature range (80 – 200 K, **Figure 5.1e**). This suggests different charge transport mechanisms at high and low temperature ranges. A hysteresis at the high temperature range between heating and cooling curves was found, and this was possibly due to breakage or mechanical fracture induced by thermal contraction of nanowires during cooling or desorption of adsorbents.

5.3.2 Conductivity of Ag-Mediated Colloidal Crystals

The conductivity measurement of DNA-interconnected Au nanoparticles, namely colloidal crystals, is another method conjecture of DNA charge transport, as discussed in Chapter 2. For this measurement, a pellet press was built, where a sample is placed in between two steel rods which serve as electric leads for a two-point-probe measurement (**Figure 5.2a**). In such design, the only current path is through the sample. Samples in powder forms are put into a soda-lime glass tube whose inner diameter is the same as the outer diameters of the steel rods (2.00 mm), and clamped gently from both sides during measurements. After measurements, the dimensions of the pellets were measured by optical microscopy.

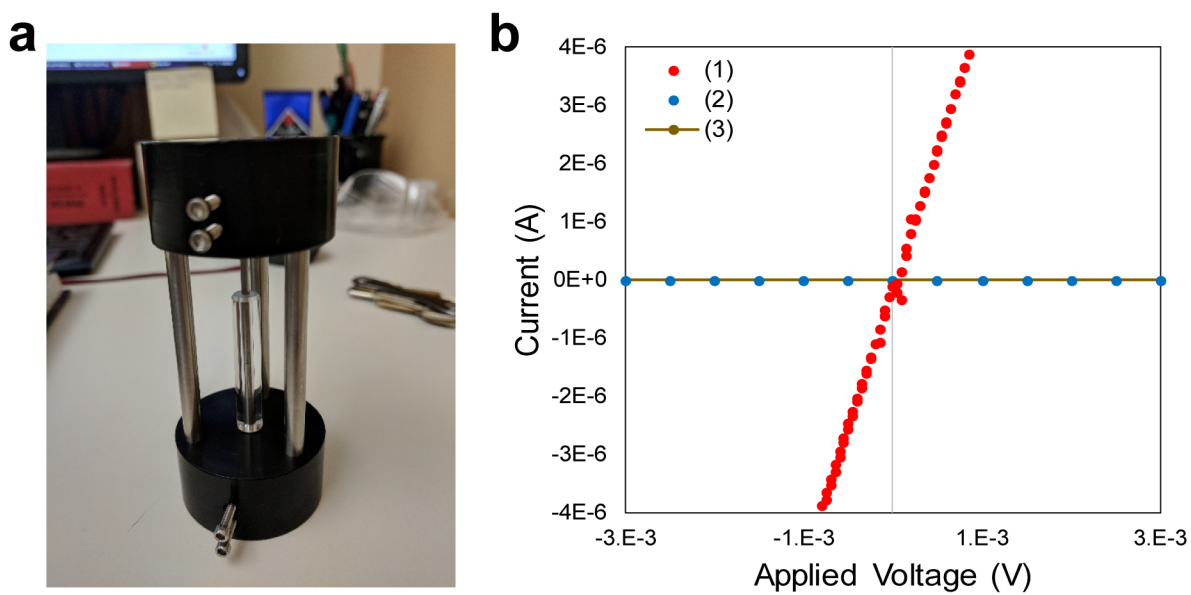


Figure 5.2. (a) A photograph of the pellet press used for the conductivity measurements of powder samples in this study. (b) I-V characteristics for (1) Ag^+ -mediated crystals without PEG spacers in DNA, (2) unmetallized PAE crystals, and (3) Ag^+ -mediated crystals with PEG spacers in DNA (**Table 4.4**).

The conductivities of rhombic dodecahedral colloidal crystal samples with bcc lattice symmetries were measured in this study. The colloidal crystals were prepared in the same manner as described in Chapter 4. In a typical experiment, PAEs with 20 nm Au cores were functionalized with 3'-propylthiol-terminated DNA strands without PEG spacers by salt aging procedure and mixed with respective linker strands ($n = 0$ DNA) in 0.5 M NaCl solution with 0.01 M PB and 0.01% SDS (**Table 5.1**). Then, the growth solution was slowly cooled from $T_m + 5$ °C to room temperature at a rate of 0.01 °C·min⁻¹ in a temperature-controlled water bath. The synthesized PAE crystals were collected and washed three times with 0.5 M NaClO₄ aqueous solution with 0.01% SDS. After the removal of the supernatant, 0.5 M aqueous AgNO₃ was quickly added to the crystals and incubated in dark for 12 h. The Ag⁺-mediated colloidal crystals were washed with pure water for three times and dried under vacuum. It is noteworthy that the pellet conductivity measurements require large quantity of powder samples and the synthesis steps were scaled up to obtain at least 1 mg of product.

First, we tested the effect of Ag⁺-mediation onto the conductivity of colloidal crystals. For the measurement, Ag⁺-mediated PAE colloidal crystals with 20 nm Au nanospheres and DNA anchor strands without PEG spacers were synthesized with $n = 0$ linkers (**Table 5.1**). The I-V characteristics of this sample exhibited clear linear characteristics, giving conductance of 4.75×10^{-3} S (**Figure 5.2b**). Two control samples prepared: the identical colloidal crystals without Ag⁺-treatment, and Ag⁺-mediated colloidal crystals with PEG spacers near the thiol anchors (**Table 5.1**). The currents through the control samples were almost negligible as compared to the experimental group, resulting in conductance values of 1.5×10^{-10} S and 1.8×10^{-10} S, respectively (**Figure 5.2b**). Although there is no evidence for retaining crystalline form for the first control sample (Chapter 4) and the effect of residual NaCl from drying is not clear, the low conductivity

of the second control sample may be the contrast between Ag⁺-DNA and unmetallized DNA, emphasizing the enhanced conductivity by Ag⁺-insertion. The second control is important because it demonstrates the importance of spatial distance from the conductive nanoparticle core to the Ag⁺-DNA, as the PEG in the anchor region virtually forms insulating layers around the cores.

The effect of interparticle distances was also experimented by varying the length of DNA linkers. PAE colloidal crystals with 20 nm Au cores were synthesized with different linker strands ($n = 0, 1, \text{ or } 2$, **Figure 5.3a** and **Table 5.1**), treated with Ag⁺, and prepared in powder forms as described above. The face-to-face interparticle distances were calculated from lattice parameters obtained by SAXS. The electric conductivities dropped exponentially with increasing interparticle distances (**Figure 5.3b**), from $1.4 \text{ S}\cdot\text{m}^{-1}$ ($n = 0$) to 8.5×10^{-4} ($n = 1$) and $1.1 \times 10^{-5} \text{ S}\cdot\text{m}^{-1}$ ($n = 2$). This result confirms that the Ag⁺-DNA in between Au nanoparticles is not as conductive as metals, and may suggest hopping charge transport mechanism rather than band conduction model because the latter would result in an inversely proportional relationship between the conductance and length.

More drastic change was observed with the core sizes. In this experiment, 10, 15, 20, 30, 40, 50, 60 and 80 nm Au nanoparticles were functionalized with, and assembled into crystal lattices with the same DNA system (**Figure 5.4a**). The conductivity of the Ag⁺-mediated PAE crystals with each core was observed to increase exponentially with increasing core diameter (**Figure 5.4b**), starting from $3.9 \times 10^{-7} \text{ S}\cdot\text{m}^{-1}$ for 10 nm core and hitting the upper limit ($\sim 15 \text{ S}\cdot\text{m}^{-1}$), for core diameters larger than 30 nm. The measurements for highly conductive samples was limited by the contact resistances of the measurement system. This can be explained by the number of charge transport through the Ag⁺-DNA interconnects. The Ag⁺-DNA strands connecting two particles can be viewed as parallel resistors, and the arrays of these Ag⁺-DNA-interconnected particles can be viewed as a series of the parallel resistors. In this case, along charge transport path

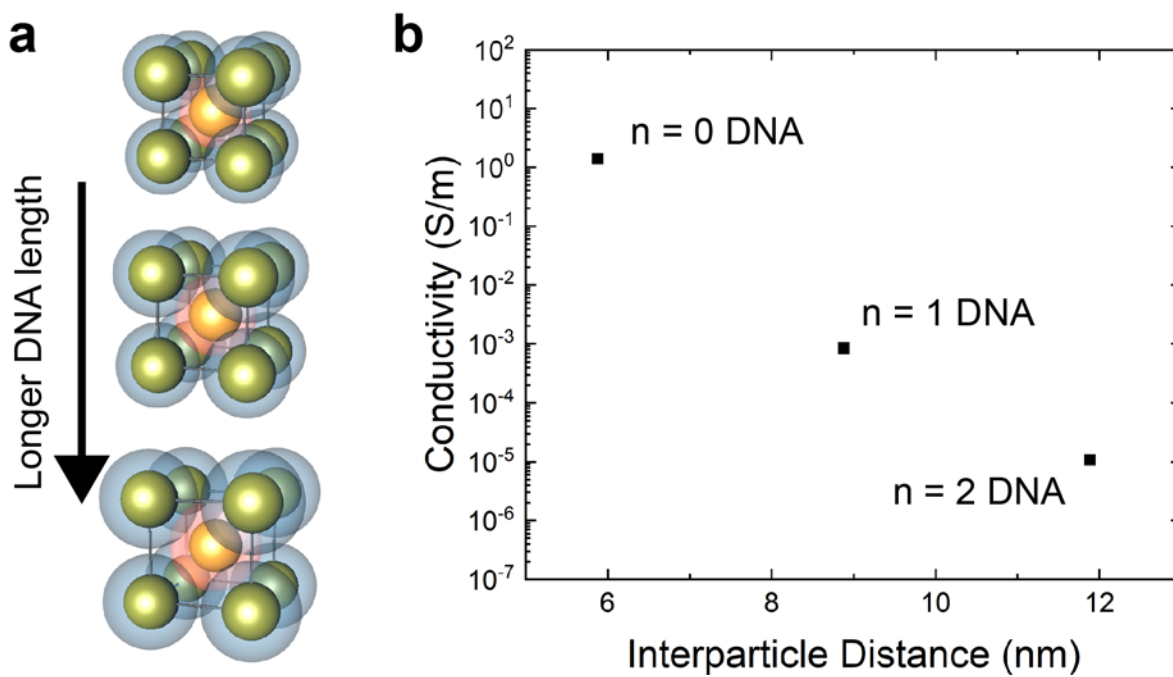


Figure 5.3. (a) Schematic diagram for bcc PAE crystal lattices with increasing interparticle distance (DNA length), $n = 0, 1,$ and 2 (**Table 5.1**) from top to bottom, respectively. The schemes were drawn to scale with the values from SAXS. (b) The measured conductivity plotted versus the interparticle distance for each sample.

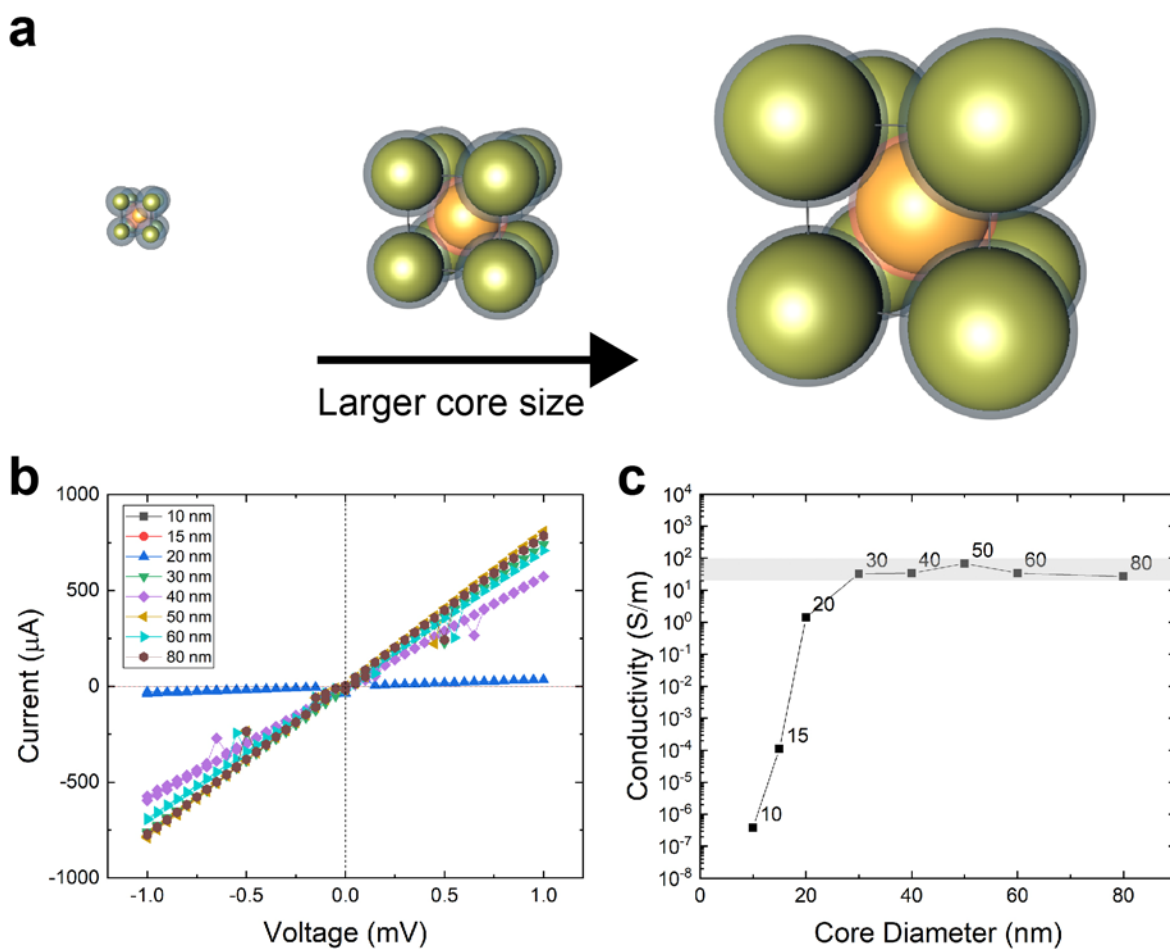


Figure 5.4. (a) Schematic diagram for bcc PAE crystal lattices with increasing core diameters, 10 nm, 40 nm, and 80 nm from left to right. The schemes were drawn to scale with reference values from SAXS. (b) I-V characteristics for all of the samples and (c) conductivity plotted versus the core diameters of each sample. The shaded area in (c) indicates the upper measurement limit of our setup mainly due to contact resistance.

over a microscopic length, the great number of strands in the parallel resistors is expected in larger particle systems, and the number of series resistors (interparticle charge transport) through the path must be inversely proportional to the lattice parameters. Both assumptions support the lower conductivity in colloidal crystals with smaller particles.

5.4 Conclusions

The charge transport behavior of Ag⁺-DNA complexes was analyzed by means of two different experimental schemes, OWL-based molecular junctions and Ag⁺-stabilized DNA-assembled colloidal crystals. Although the mechanistic understanding yet needs to be further discovered, the Ag⁺-DNA complexes showed orders of magnitude higher charge transport behaviors observed in both experiments, and thus, such systems as molecular wires and components for nanoparticle-based device architectures and next-generation electronic circuits.

5.5 Experimental

5.5.1 Materials

AAO templates were purchased from Synkera and Whatman. A PVD 75 instrument (Kurt J. Lesker Company) was used for Ag and SiO₂ deposition during OWL methodology and for Cr and Au for electrode patterns. Electroplating solutions were purchased from Technic Inc. (Techni Silver Cylless® II RTU for Ag, Orotemp 24 RTU for Au, and Nickel Sulfamate RTU for Ni). NaOH, FeCl₃, acetone, and MHA were purchased from Sigma-Aldrich. Citrate-capped spherical Au nanoparticles with diameters from 10 nm to 80 nm were purchased from Ted Pella. Milli-Q® water was used in aqueous solutions and washing. FEI Quanta SEM was used for electrode patterning by e-beam lithography and Hitachi SU8030 FE-SEM was used for imaging.

The electrical measurements were carried out by a Keithley 4200 SMU coupled with a ST-500 Probe Station by Janis Research Company Inc.

The sequence design, synthesis, and purifications of DNA were carried out in a similar manner as discussed in the previous chapter. The sequences used in this study is in **Table 5.1**.

Table 5.1. DNA sequences used in this study.

Conductivity Experiments	DNA Sequences (5' → 3')
37-mer	HS– GGA CTC ^{Br} GAC TCC GGA CTC ^{Br} GAC TCC GGA CTC ^{Br} GAC TCC G –SH
Thiol-modified DNA strands	DNA Sequences (5' → 3')
A without PEG	TCA ACT ATT CCT ACC TAC –SH
B without PEG	TCC ACT CAT ACT CAG CAA –SH
A with PEG	TCA ACT ATT CCT ACC TAC (Spacer 18) ₂ –SH
B with PEG	TCC ACT CAT ACT CAG CAA (Spacer 18) ₂ –SH
Linker strands	DNA Sequences (5' → 3')
A linker (n = 0, 1, or 2)	GTA GGT AGG AAT AGT TGA (Block modular unit) _n (Spacer 18) TTT CCT T
B linker (n = 0, 1, or 2)	TTG CTG AGT ATG AGT GGA (Block modular unit) _n (Spacer 18) AAG GAA A
Block strands	DNA Sequences (5' → 3')
Block modular unit	(Spacer 18) TTA CTG AGC AGC ACT GAT TT
Block duplex for linkers strands	AAA TCA GTG CTG CTC AGT AA

“Spacer 18” refers to the six ethylene glycol units with modified phosphoramidites, which were manufactured by Glen Research.

C^{Br} refers to C base modified with Br in the C5 in the pyrimidine (fullname: 5-bromo-2'-deoxycytidine)

5.5.2 Electrochemical Synthesis

First, a 250 nm thick Ag layer was deposited on one side of the AAO templates with pore diameter of 100 nm (SM100-50-25) by e-beam physical vapor deposition and used as the working electrode in a three-electrode electroplating configuration. Ag, Au, Ni, and Au was electrodeposited with respective precursor solution in order, with a Pt mesh as the counter electrode and an Ag/AgCl reference electrode. While the length of each segment was controlled by the amount of charge, the applied potentials were -980 mV for Au and -900 mV for Ag and Ni.

electrode and an Ag/AgCl reference electrode. While the length of each segment was controlled by the amount of charge, the applied potentials were -980 mV for Au and -900 mV for Ag and Ni.

Chapter 6 Conclusion and Future Remarks



“There's Plenty of Room at the Bottom,” is a famous quote by Richard Feynman (at the 1959 American Physical Society meeting), a Nobel Laureate in Physics. During his distinguished career, he presented many inspiring ideas that were only possible if we can manipulate matters in tiny scales. By going small, we can integrate more information into a fixed volume (“the entire *Encyclopædia Britannica* on the head of a pin”). Feynman’s projection has inspired many scientists to reach the “Bottom” and to develop fundamental scientific understandings that drive real-world applications, such as the microscopies that allow us to examine the building blocks of life and integrated circuits that power the computers that have connected the world.

DNA, one of the most information-dense molecules, have been introduced as a key component for “manipulation of matters in tiny scale” since it has been developed and deployed as programmable bonds for nanoparticle assemblies.² Upon the findings of predecessors, my work has been conducted in pursuit of solution-processed device architectures composed of colloidal nanomaterials, which are more scalable than vacuum-involving procedures and controlled by thermal treatments with sharp melting transition.

Specifically, as mentioned in the previous chapters, the DNA-mediated nanoparticle assembly is not constricted to processing nanoparticles composed of noble metals as most examples in this thesis, but it has already been demonstrated that nanoparticles from a variety of materials library can be functionalized and assembled in a similar manner.¹⁸ The next question must be how to make use of them, especially by enabling the charge transport through structural DNA scaffolds in between nanoparticles. For example, it is expected for the superlattices composed of quantum dots to exhibit superfluorescence¹⁶⁹ or thermoelectric effects¹⁷⁰ if the charge and energy transport between the individual building blocks is not obscured, in addition to being semiconducting devices with tunable bandgaps by the core sizes.¹¹⁵ Also, single-particle

architectures for computing will be realized with the development of molecular wires and programmable assembly of smart nanomaterials.

The photocatalytic effects of semiconducting nanostructures and their assemblies have been actively studied for chemical reactions, especially ones to solve important problems such as water splitting or CO₂ reduction. The efficiency can be significantly enhanced with the use of conductive and programmable ligands between the individual building blocks composing the superlattices, as demonstrated by the works pioneered by Cha and others.¹⁵⁷⁻¹⁶⁰ The ideal system consist of periodic lattices for enhanced packing density and materials transport due to its high porosity,¹⁵² while having chemical and thermal robustness (Chapter 4) that allow it to withstand harsh reaction conditions.

The optical properties of the DNA-assembled colloidal single crystals shaped in Wulff polyhedra have been extensively studied,^{9, 34} and given the ability to incorporate photoactive molecules precisely placed interstitial sites in the lattice,¹¹ such structures have great potential for developing optical metamaterials and photonic crystals. The realization of the optical and photonic devices has been advanced within this thesis by developing reliable synthetic methodology (Chapter 3) and stabilization procedures without any perturbation by matrix properties (Chapter 4).

Additionally, the concept of selective functionalization can be extended to functionalize the negative curvatures in nanorings generated by coaxial lithography⁹⁵ (**Figure 6.1a**). This selective functionalization techniques for two-dimensional cavities can be further used to build assembly structures (**Figure 6.1b**) which are hard to realize with any other existing methods.

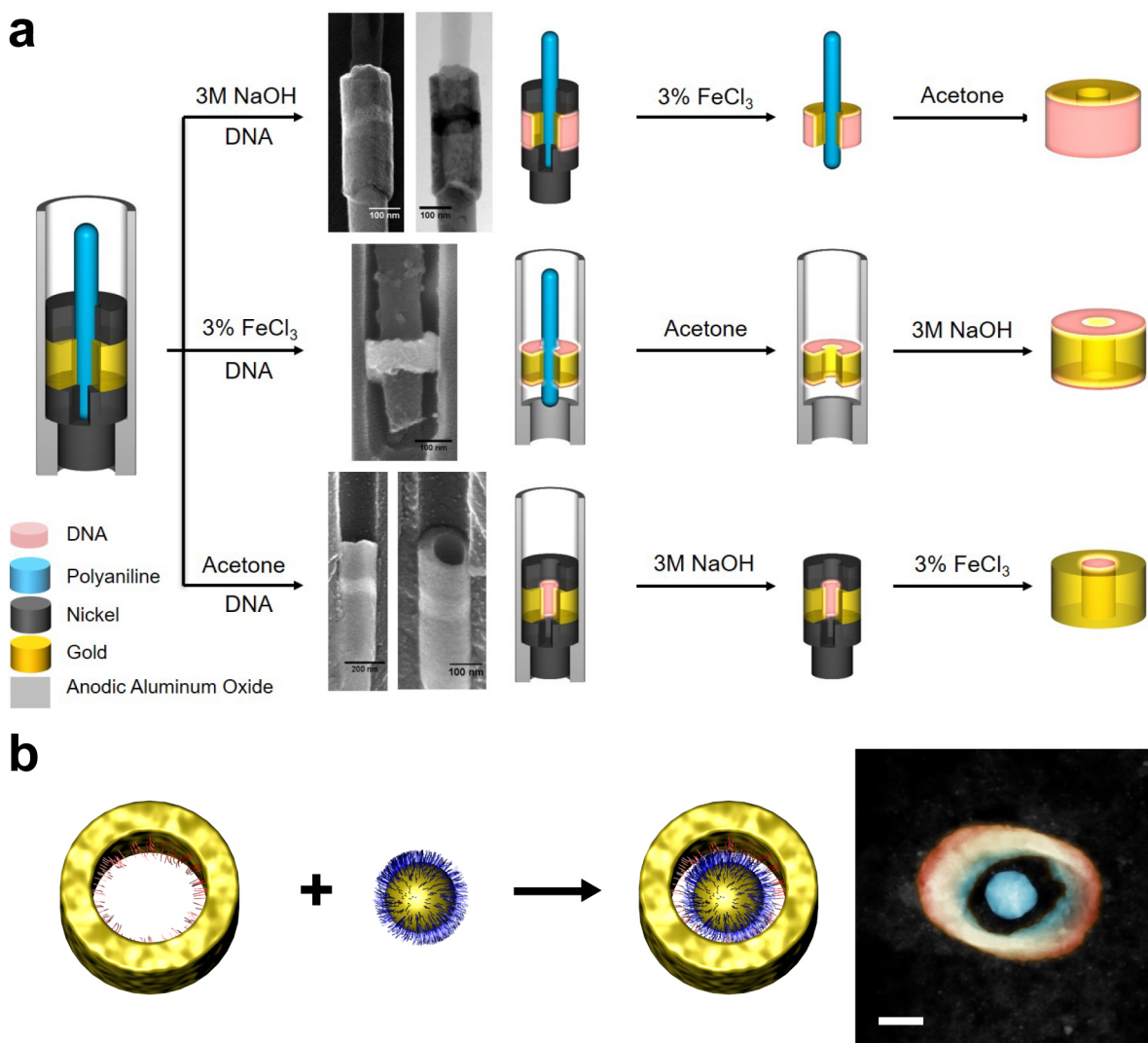


Figure 6.1. (a) Schematic diagrams and respective electron micrographs for selective functionalization of template-synthesized nanoring surfaces, side barrels (top), top and bottom ends (middle), and inner faces (bottom). (b) Assembly of spherical nanoparticles selectively adsorbed and bound into the center of a nanoring. Scale bar: 50 nm.

I would like to conclude this thesis with a favorite quote from a friend who answered my question pertaining to whether our science is really contributing to changing the world and making it a better place.

“We nanoscientists are also changing the world, by one nanometer at a time.”

– Dr. Monica Guan, a former Mirkin Group member

I hope that the work introduced throughout this thesis contributes to the field at least in a small manner and inspires others to pursue similar goals.

References

1. Mirkin, C. A.; Letsinger, R. L.; Mucic, R. C.; Storhoff, J. J., A DNA-based method for rationally assembling nanoparticles into macroscopic materials. *Nature* **1996**, *382*, 607-609.
2. Jones, M. R.; Seeman, N. C.; Mirkin, C. A., Programmable materials and the nature of the DNA bond. *Science* **2015**, *347*, 1260901.
3. Boles, M. A.; Engel, M.; Talapin, D. V., Self-assembly of colloidal nanocrystals: from intricate structures to functional materials. *Chem. Rev.* **2016**, *116*, 11220-11289.
4. Walker, D. A.; Leitsch, E. K.; Nap, R. J.; Szleifer, I.; Grzybowski, B. A., Geometric curvature controls the chemical patchiness and self-assembly of nanoparticles. *Nat. Nanotech.* **2013**, *8*, 676-681.
5. Nie, Z. H.; Petukhova, A.; Kumacheva, E., Properties and emerging applications of self-assembled structures made from inorganic nanoparticles. *Nat. Nanotech.* **2010**, *5*, 15-25.
6. Wang, T.; Zhuang, J. Q.; Lynch, J.; Chen, O.; Wang, Z. L.; Wang, X. R.; LaMontagne, D.; Wu, H. M.; Wang, Z. W.; Cao, Y. C., Self-Assembled Colloidal Superparticles from Nanorods. *Science* **2012**, *338*, 358-363.
7. Dong, A. G.; Chen, J.; Vora, P. M.; Kikkawa, J. M.; Murray, C. B., Binary nanocrystal superlattice membranes self-assembled at the liquid-air interface. *Nature* **2010**, *466*, 474-477.
8. Whitesides, G. M.; Grzybowski, B., Self-assembly at all scales. *Science* **2002**, *295*, 2418-2421.
9. Park, D. J.; Zhang, C.; Ku, J. C.; Zhou, Y.; Schatz, G. C.; Mirkin, C. A., Plasmonic photonic crystals realized through DNA-programmable assembly. *Proc. Natl. Acad. Sci. U. S. A.* **2015**, *112*, 977-981.
10. Ross, M. B.; Ku, J. C.; Vaccarezza, V. M.; Schatz, G. C.; Mirkin, C. A., Nanoscale form dictates mesoscale function in plasmonic DNA-nanoparticle superlattices. *Nat. Nanotech.* **2015**, *10*, 453-458.
11. Park, D. J.; Ku, J. C.; Sun, L.; Lethiec, C. M.; Stern, N. P.; Schatz, G. C.; Mirkin, C. A., Directional emission from dye-functionalized plasmonic DNA superlattice microcavities. *Proc. Natl. Acad. Sci. U. S. A.* **2017**, *114*, 457-461.

12. Sun, L.; Lin, H. X.; Kohlstedt, K. L.; Schatz, G. C.; Mirkin, C. A., Design principles for photonic crystals based on plasmonic nanoparticle superlattices. *Proc. Natl. Acad. Sci. U. S. A.* **2018**, *115*, 7242-7247.
13. Ross, M. B.; Ku, J. C.; Lee, B.; Mirkin, C. A.; Schatz, G. C., Plasmonic Metallurgy Enabled by DNA. *Adv. Mater.* **2016**, *28*, 2790-2794.
14. Bain, C. D.; Whitesides, G. M., Modeling Organic-Surfaces with Self-Assembled Monolayers. *Angew. Chem. Int. Ed.* **1989**, *28*, 506-512.
15. Park, S. Y.; Lytton-Jean, A. K.; Lee, B.; Weigand, S.; Schatz, G. C.; Mirkin, C. A., DNA-programmable nanoparticle crystallization. *Nature* **2008**, *451*, 553-556.
16. Macfarlane, R. J.; Lee, B.; Jones, M. R.; Harris, N.; Schatz, G. C.; Mirkin, C. A., Nanoparticle superlattice engineering with DNA. *Science* **2011**, *334*, 204-208.
17. Lin, H. X.; Lee, S. M.; Sun, L.; Spellings, M.; Engel, M.; Glotzer, S. C.; Mirkin, C. A., Clathrate colloidal crystals. *Science* **2017**, *355*, 931-935.
18. Zhang, C.; Macfarlane, R. J.; Young, K. L.; Choi, C. H. J.; Hao, L. L.; Auyeung, E.; Liu, G. L.; Zhou, X. Z.; Mirkin, C. A., A general approach to DNA-programmable atom equivalents. *Nat. Mater.* **2013**, *12*, 741-746.
19. Wang, Y. F.; Wang, Y.; Zheng, X. L.; Ducrot, E.; Lee, M. G.; Yi, G. R.; Weck, M.; Pine, D. J., Synthetic Strategies Toward DNA-Coated Colloids that Crystallize. *J. Am. Chem. Soc.* **2015**, *137*, 10760-10766.
20. Brodin, J. D.; Auyeung, E.; Mirkin, C. A., DNA-mediated engineering of multicomponent enzyme crystals. *Proc. Natl. Acad. Sci. U. S. A.* **2015**, *112*, 4564-4569.
21. O'Brien, M. N.; Jones, M. R.; Lee, B.; Mirkin, C. A., Anisotropic nanoparticle complementarity in DNA-mediated co-crystallization. *Nat. Mater.* **2015**, *14*, 833-839.
22. Jones, M. R.; Macfarlane, R. J.; Lee, B.; Zhang, J. A.; Young, K. L.; Senesi, A. J.; Mirkin, C. A., DNA-nanoparticle superlattices formed from anisotropic building blocks. *Nat. Mater.* **2010**, *9*, 913-917.
23. Lu, F.; Yager, K. G.; Zhang, Y. G.; Xin, H. L.; Gang, O., Superlattices assembled through shape-induced directional binding. *Nat. Commun.* **2015**, *6*, 6912.
24. Ducrot, E.; He, M.; Yi, G. R.; Pine, D. J., Colloidal alloys with preassembled clusters and spheres. *Nat. Mater.* **2017**, *16*, 652-657.

25. Auyeung, E.; Cutler, J. I.; Macfarlane, R. J.; Jones, M. R.; Wu, J. S.; Liu, G.; Zhang, K.; Osberg, K. D.; Mirkin, C. A., Synthetically programmable nanoparticle superlattices using a hollow three-dimensional spacer approach. *Nat. Nanotech.* **2012**, *7*, 24-28.
26. Liu, W. Y.; Tagawa, M.; Xin, H. L. L.; Wang, T.; Emamy, H.; Li, H. L.; Yager, K. G.; Starr, F. W.; Tkachenko, A. V.; Gang, O., Diamond family of nanoparticle superlattices. *Science* **2016**, *351*, 582-586.
27. Auyeung, E.; Li, T. I.; Senesi, A. J.; Schmucker, A. L.; Pals, B. C.; de la Cruz, M. O.; Mirkin, C. A., DNA-mediated nanoparticle crystallization into Wulff polyhedra. *Nature* **2014**, *505*, 73-77.
28. O'Brien, M. N.; Lin, H. X.; Girard, M.; de la Cruz, M. O.; Mirkin, C. A., Programming Colloidal Crystal Habit with Anisotropic Nanoparticle Building Blocks and DNA Bonds. *J. Am. Chem. Soc.* **2016**, *138*, 14562-14565.
29. Seo, S. E.; Girard, M.; de la Cruz, M. O.; Mirkin, C. A., Non-equilibrium anisotropic colloidal single crystal growth with DNA. *Nat. Commun.* **2018**, *9*, 4558.
30. Senesi, A. J.; Eichelsdoerfer, D. J.; Macfarlane, R. J.; Jones, M. R.; Auyeung, E.; Lee, B.; Mirkin, C. A., Stepwise Evolution of DNA-Programmable Nanoparticle Superlattices. *Angew. Chem. Int. Ed.* **2013**, *52*, 6624-6628.
31. Ku, J. C.; Ross, M. B.; Schatz, G. C.; Mirkin, C. A., Conformal, Macroscopic Crystalline Nanoparticle Sheets Assembled with DNA. *Adv. Mater.* **2015**, *27*, 3159-3163.
32. Hellstrom, S. L.; Kim, Y.; Fakonas, J. S.; Senesi, A. J.; Macfarlane, R. J.; Mirkin, C. A.; Atwater, H. A., Epitaxial Growth of DNA-Assembled Nanoparticle Superlattices on Patterned Substrates. *Nano Lett.* **2013**, *13*, 6084-6090.
33. Wang, M. X.; Seo, S. E.; Gabrys, P. A.; Fleischman, D.; Lee, B.; Kim, Y.; Atwater, H. A.; Macfarlane, R. J.; Mirkin, C. A., Epitaxy: Programmable Atom Equivalents Versus Atoms. *ACS Nano* **2017**, *11*, 180-185.
34. Sun, L.; Lin, H. X.; Park, D. J.; Bourgeois, M. R.; Ross, M. B.; Ku, J. C.; Schatz, G. C.; Mirkin, C. A., Polarization-Dependent Optical Response in Anisotropic Nanoparticle-DNA Superlattices. *Nano Lett.* **2017**, *17*, 2313-2318.
35. Oh, T.; Ku, J. C.; Ozel, T.; Mirkin, C. A., Orthogonal Chemical Modification of Template-Synthesized Nanostructures with DNA. *J. Am. Chem. Soc.* **2017**, *139*, 6831-6834.

36. Eley, D. D.; Spivey, D. I., Semiconductivity of Organic Substances .9. Nucleic Acid in Dry State. *Trans. Faraday Soc.* **1962**, *58*, 411-415.
37. Lewis, F. D.; Wu, T. F.; Zhang, Y. F.; Letsinger, R. L.; Greenfield, S. R.; Wasielewski, M. R., Distance-dependent electron transfer in DNA hairpins. *Science* **1997**, *277*, 673-676.
38. Murphy, C. J.; Arkin, M. R.; Jenkins, Y.; Ghatlia, N. D.; Bossmann, S. H.; Turro, N. J.; Barton, J. K., Long-Range Photoinduced Electron-Transfer through a DNA Helix. *Science* **1993**, *262*, 1025-1029.
39. Fink, H. W.; Schonberger, C., Electrical conduction through DNA molecules. *Nature* **1999**, *398*, 407-410.
40. Porath, D.; Bezryadin, A.; de Vries, S.; Dekker, C., Direct measurement of electrical transport through DNA molecules. *Nature* **2000**, *403*, 635-638.
41. Braun, E.; Eichen, Y.; Sivan, U.; Ben-Yoseph, G., DNA-templated assembly and electrode attachment of a conducting silver wire. *Nature* **1998**, *391*, 775-778.
42. Kasumov, A. Y.; Kociak, M.; Gueron, S.; Reulet, B.; Volkov, V. T.; Klinov, D. V.; Bouchiat, H., Proximity-induced superconductivity in DNA. *Science* **2001**, *291*, 280-282.
43. Xu, B. Q.; Tao, N. J. J., Measurement of single-molecule resistance by repeated formation of molecular junctions. *Science* **2003**, *301*, 1221-1223.
44. Xu, B. Q.; Zhang, P. M.; Li, X. L.; Tao, N. J., Direct conductance measurement of single DNA molecules in aqueous solution. *Nano Lett.* **2004**, *4*, 1105-1108.
45. Wang, K.; Hamill, J. M.; Wang, B.; Guo, C. L.; Jiang, S. B.; Huang, Z.; Xu, B. Q., Structure determined charge transport in single DNA molecule break junctions. *Chem. Sci.* **2014**, *5*, 3425-3431.
46. Artes, J. M.; Li, Y. H.; Qi, J. Q.; Anantram, M. P.; Hihath, J., Conformational gating of DNA conductance. *Nat. Commun.* **2015**, *6*, 8870.
47. Xiang, L. M.; Palma, J. L.; Bruot, C.; Mujica, V.; Ratner, M. A.; Tao, N. J., Intermediate tunnelling-hopping regime in DNA charge transport. *Nat. Chem.* **2015**, *7*, 221-226.
48. Bruot, C.; Xiang, L. M.; Palma, J. L.; Tao, N. J., Effect of Mechanical Stretching on DNA Conductance. *ACS Nano* **2015**, *9*, 88-94.

49. Guo, X. F.; Small, J. P.; Klare, J. E.; Wang, Y. L.; Purewal, M. S.; Tam, I. W.; Hong, B. H.; Caldwell, R.; Huang, L. M.; O'Brien, S.; Yan, J. M.; Breslow, R.; Wind, S. J.; Hone, J.; Kim, P.; Nuckolls, C., Covalently bridging gaps in single-walled carbon nanotubes with conducting molecules. *Science* **2006**, *311*, 356-359.
50. Guo, X. F.; Gorodetsky, A. A.; Hone, J.; Barton, J. K.; Nuckolls, C., Conductivity of a single DNA duplex bridging a carbon nanotube gap. *Nat. Nanotech.* **2008**, *3*, 163-167.
51. Livshits, G. I.; Stern, A.; Rotem, D.; Borovok, N.; Eidelstein, G.; Migliore, A.; Penzo, E.; Wind, S. J.; Di Felice, R.; Skourtis, S. S.; Cuevas, J. C.; Gurevich, L.; Kotlyar, A. B.; Porath, D., Long-range charge transport in single G-quadruplex DNA molecules. *Nat. Nanotech.* **2014**, *9*, 1040-1046.
52. Qin, L. D.; Park, S.; Huang, L.; Mirkin, C. A., On-wire lithography. *Science* **2005**, *309*, 113-115.
53. Qin, L. D.; Jang, J. W.; Huang, L.; Mirkin, C. A., Sub-5-nm gaps prepared by on-wire lithography: Correlating gap size with electrical transport. *Small* **2007**, *3*, 86-90.
54. Chen, X.; Jeon, Y. M.; Jang, J. W.; Qin, L.; Huo, F.; Wei, W.; Mirkin, C. A., On-wire lithography-generated molecule-based transport junctions: A new testbed for molecular electronics. *J. Am. Chem. Soc.* **2008**, *130*, 8166-8168.
55. Banholzer, M. J.; Qin, L. D.; Millstone, J. E.; Osberg, K. D.; Mirkin, C. A., On-wire lithography: synthesis, encoding and biological applications. *Nat. Protoc.* **2009**, *4*, 838-848.
56. Chen, X. D.; Yeganeh, S.; Qin, L. D.; Li, S. Z.; Xue, C.; Braunschweig, A. B.; Schatz, G. C.; Ratner, M. A.; Mirkin, C. A., Chemical Fabrication of Heterometallic Nanogaps for Molecular Transport Junctions. *Nano Lett.* **2009**, *9*, 3974-3979.
57. Chen, X. D.; Braunschweig, A. B.; Wiester, M. J.; Yeganeh, S.; Ratner, M. A.; Mirkin, C. A., Spectroscopic Tracking of Molecular Transport Junctions Generated by Using Click Chemistry. *Angew. Chem. Int. Ed.* **2009**, *48*, 5178-5181.
58. Meng, F. B.; Hervault, Y. M.; Shao, Q.; Hu, B. H.; Norel, L.; Rigaut, S.; Chen, X. D., Orthogonally modulated molecular transport junctions for resettable electronic logic gates. *Nat. Commun.* **2014**, *5*, 3023.
59. Schmucker, A. L.; Barin, G.; Brown, K. A.; Rycenga, M.; Coskun, A.; Buyukcakir, O.; Osberg, K. D.; Stoddart, J. F.; Mirkin, C. A., Electronic and Optical Vibrational Spectroscopy of Molecular Transport Junctions Created by On-Wire Lithography. *Small* **2013**, *9*, 1900-1903.

60. Zheng, G. F.; Chen, X. D.; Mirkin, C. A., Complementary Electrical and Spectroscopic Detection Assays with On-Wire-Lithography-Based Nanostructures. *Small* **2009**, *5*, 2537-2540.
61. Boles, M. A.; Ling, D. S.; Hyeon, T.; Talapin, D. V., The surface science of nanocrystals (vol 15, pg 141, 2016). *Nat. Mater.* **2016**, *15*, 364-364.
62. Park, S. J.; Taton, T. A.; Mirkin, C. A., Array-based electrical detection of DNA with nanoparticle probes. *Science* **2002**, *295*, 1503-1506.
63. Cao, Y. W. C.; Jin, R. C.; Mirkin, C. A., Nanoparticles with Raman spectroscopic fingerprints for DNA and RNA detection. *Science* **2002**, *297*, 1536-1540.
64. Rosi, N. L.; Giljohann, D. A.; Thaxton, C. S.; Lytton-Jean, A. K. R.; Han, M. S.; Mirkin, C. A., Oligonucleotide-modified gold nanoparticles for intracellular gene regulation. *Science* **2006**, *312*, 1027-1030.
65. Radovic-Moreno, A. F.; Chernyak, N.; Mader, C. C.; Nallagatla, S.; Kang, R. S.; Hao, L. L.; Walker, D. A.; Halo, T. L.; Merkel, T. J.; Rische, C. H.; Anantamula, S.; Burkhart, M.; Mirkin, C. A.; Gryaznov, S. M., Immunomodulatory spherical nucleic acids. *Proc. Natl. Acad. Sci. U. S. A.* **2015**, *112*, 3892-3897.
66. Myers, B. D.; Lin, Q. Y.; Wu, H. X.; Luijten, E.; Mirkin, C. A.; Dravid, V. P., Size-Selective Nanoparticle Assembly on Substrates by DNA Density Patterning. *ACS Nano* **2016**, *10*, 5679-5686.
67. Loweth, C. J.; Caldwell, W. B.; Peng, X. G.; Alivisatos, A. P.; Schultz, P. G., DNA-based assembly of gold nanocrystals. *Angew. Chem. Int. Ed.* **1999**, *38*, 1808-1812.
68. Zanchet, D.; Micheel, C. M.; Parak, W. J.; Gerion, D.; Williams, S. C.; Alivisatos, A. P., Electrophoretic and structural studies of DNA-directed Au nanoparticle groupings. *J. Phys. Chem. B* **2002**, *106*, 11758-11763.
69. Pramod, P.; Joseph, S. T. S.; Thomas, K. G., Preferential end functionalization of au nanorods through electrostatic interactions. *J. Am. Chem. Soc.* **2007**, *129*, 6712-6713.
70. Nie, Z.; Fava, D.; Kumacheva, E.; Zou, S.; Walker, G. C.; Rubinstein, M., Self-assembly of metal-polymer analogues of amphiphilic triblock copolymers. *Nat. Mater.* **2007**, *6*, 609-614.
71. Xu, L.; Kuang, H.; Xu, C.; Ma, W.; Wang, L.; Kotov, N. A., Regiospecific plasmonic assemblies for in situ Raman spectroscopy in live cells. *J. Am. Chem. Soc.* **2012**, *134*, 1699-1709.

72. Ma, W.; Kuang, H.; Xu, L.; Ding, L.; Xu, C.; Wang, L.; Kotov, N. A., Attomolar DNA detection with chiral nanorod assemblies. *Nat. Commun.* **2013**, *4*, 2689.
73. Laibinis, P. E.; Hickman, J. J.; Wrighton, M. S.; Whitesides, G. M., Orthogonal Self-Assembled Monolayers - Alkanethiols on Gold and Alkane Carboxylic-Acids on Alumina. *Science* **1989**, *245*, 845-847.
74. Gardner, T. J.; Frisbie, C. D.; Wrighton, M. S., Systems for Orthogonal Self-Assembly of Electroactive Monolayers on Au and Ito - an Approach to Molecular Electronics. *J. Am. Chem. Soc.* **1995**, *117*, 6927-6933.
75. Salem, A. K.; Searson, P. C.; Leong, K. W., Multifunctional nanorods for gene delivery. *Nat. Mater.* **2003**, *2*, 668-671.
76. Wildt, B.; Mali, P.; Searson, P. C., Electrochemical template synthesis of multisegment nanowires: fabrication and protein functionalization. *Langmuir* **2006**, *22*, 10528-10534.
77. Salant, A.; Amitay-Sadovsky, E.; Banin, U., Directed self-assembly of gold-tipped CdSe nanorods. *J. Am. Chem. Soc.* **2006**, *128*, 10006-10007.
78. Wang, Y. F.; Wang, Y.; Breed, D. R.; Manoharan, V. N.; Feng, L.; Hollingsworth, A. D.; Weck, M.; Pine, D. J., Colloids with valence and specific directional bonding. *Nature* **2012**, *491*, 51-55.
79. Xing, H.; Wang, Z.; Xu, Z.; Wong, N. Y.; Xiang, Y.; Liu, G. L.; Lu, Y., DNA-directed assembly of asymmetric nanoclusters using Janus nanoparticles. *ACS Nano* **2012**, *6*, 802-809.
80. Wang, F.; Cheng, S.; Bao, Z. H.; Wang, J. F., Anisotropic Overgrowth of Metal Heterostructures Induced by a Site-Selective Silica Coating. *Angew. Chem. Int. Ed.* **2013**, *52*, 10344-10348.
81. Bauer, L. A.; Reich, D. H.; Meyer, G. J., Selective functionalization of two-component magnetic nanowires. *Langmuir* **2003**, *19*, 7043-7048.
82. Xu, X. Y.; Rosi, N. L.; Wang, Y. H.; Huo, F. W.; Mirkin, C. A., Asymmetric functionalization of gold nanoparticles with oligonucleotides. *J. Am. Chem. Soc.* **2006**, *128*, 9286-9287.
83. Huo, F. W.; Lytton-Jean, A. K. R.; Mirkin, C. A., Asymmetric functionalization of nanoparticles based on thermally addressable DNA interconnects. *Adv. Mater.* **2006**, *18*, 2304-2306.

84. Rycenga, M.; McLellan, J. M.; Xia, Y. N., Controlling the assembly of silver nanocubes through selective functionalization of their faces. *Adv. Mater.* **2008**, *20*, 2416-2420.
85. Martin, C. R., Nanomaterials - a Membrane-Based Synthetic Approach. *Science* **1994**, *266*, 1961-1966.
86. Almawlawi, D.; Liu, C. Z.; Moskovits, M., Nanowires Formed in Anodic Oxide Nanotemplates. *J. Mater. Res.* **1994**, *9*, 1014-1018.
87. Martin, B. R.; Dermody, D. J.; Reiss, B. D.; Fang, M. M.; Lyon, L. A.; Natan, M. J.; Mallouk, T. E., Orthogonal self-assembly on colloidal gold-platinum nanorods. *Adv. Mater.* **1999**, *11*, 1021-1025.
88. Nicewarner-Pena, S. R.; Freeman, R. G.; Reiss, B. D.; He, L.; Pena, D. J.; Walton, I. D.; Cromer, R.; Keating, C. D.; Natan, M. J., Submicrometer metallic barcodes. *Science* **2001**, *294*, 137-141.
89. Klein, J. D.; Herrick, R. D.; Palmer, D.; Sailor, M. J.; Brumlik, C. J.; Martin, C. R., Electrochemical Fabrication of Cadmium Chalcogenide Microdiode Arrays. *Chem. Mater.* **1993**, *5*, 902-904.
90. Pena, D. J.; Mbindyo, J. K. N.; Carado, A. J.; Mallouk, T. E.; Keating, C. D.; Razavi, B.; Mayer, T. S., Template growth of photoconductive metal-CdSe-metal nanowires. *J. Phys. Chem. B* **2002**, *106*, 7458-7462.
91. Liu, R.; Lee, S. B., MnO₂/poly(3,4-ethylenedioxythiophene) coaxial nanowires by one-step coelectrodeposition for electrochemical energy storage. *J. Am. Chem. Soc.* **2008**, *130*, 2942-2943.
92. Schierhorn, M.; Boettcher, S. W.; Kraemer, S.; Stucky, G. D.; Moskovits, M., Photoelectrochemical performance of CdSe nanorod arrays grown on a transparent conducting substrate. *Nano Lett.* **2009**, *9*, 3262-3267.
93. Park, S.; Lim, J. H.; Chung, S. W.; Mirkin, C. A., Self-assembly of mesoscopic metal-polymer amphiphiles. *Science* **2004**, *303*, 348-351.
94. Ozel, T.; Bourret, G. R.; Schmucker, A. L.; Brown, K. A.; Mirkin, C. A., Hybrid semiconductor core-shell nanowires with tunable plasmonic nanoantennas. *Adv. Mater.* **2013**, *25*, 4515-4520.
95. Ozel, T.; Bourret, G. R.; Mirkin, C. A., Coaxial lithography. *Nat. Nanotech.* **2015**, *10*, 319-324.

96. Wen, L. Y.; Xu, R.; Mi, Y.; Lei, Y., Multiple nanostructures based on anodized aluminium oxide templates. *Nat. Nanotech.* **2017**, *12*, 244-250.
97. Yu, J. S.; Kim, J. Y.; Lee, S.; Mbindyo, J. K. N.; Martin, B. R.; Mallouk, T. E., Template synthesis of polymer-insulated colloidal gold nanowires with reactive ends. *Chem. Commun.* **2000**, *0*, 2445-2446.
98. Hurst, S. J.; Lytton-Jean, A. K.; Mirkin, C. A., Maximizing DNA loading on a range of gold nanoparticle sizes. *Anal. Chem.* **2006**, *78*, 8313-8.
99. Smith, A. M.; Marbella, L. E.; Johnston, K. A.; Hartmann, M. J.; Crawford, S. E.; Kozycz, L. M.; Seferos, D. S.; Millstone, J. E., Quantitative analysis of thiolated ligand exchange on gold nanoparticles monitored by ¹H NMR spectroscopy. *Anal. Chem.* **2015**, *87*, 2771-2778.
100. Azzaroni, O.; Schilardi, P. L.; Salvarezza, R. C., Metal electrodeposition on self-assembled monolayers: a versatile tool for pattern transfer on metal thin films. *Electrochim. Acta* **2003**, *48*, 3107-3114.
101. Auyeung, E.; Macfarlane, R. J.; Choi, C. H.; Cutler, J. I.; Mirkin, C. A., Transitioning DNA-engineered nanoparticle superlattices from solution to the solid state. *Adv. Mater.* **2012**, *24*, 5181-5186.
102. Brinkers, S.; Dietrich, H. R. C.; de Groote, F. H.; Young, I. T.; Rieger, B., The persistence length of double stranded DNA determined using dark field tethered particle motion. *J. Chem. Phys.* **2009**, *130*, 215105.
103. Gross, P.; Laurens, N.; Oddershede, L. B.; Bockelmann, U.; Peterman, E. J. G.; Wuite, G. J. L., Quantifying how DNA stretches, melts and changes twist under tension. *Nat. Phys.* **2011**, *7*, 731-736.
104. Shade, C. M.; Kennedy, R. D.; Rouge, J. L.; Rosen, M. S.; Wang, M. X.; Seo, S. E.; Clingerman, D. J.; Mirkin, C. A., Duplex-Selective Ruthenium-Based DNA Intercalators. *Chem. Eur. J.* **2015**, *21*, 10983-10987.
105. Seo, S. E.; Wang, M. X.; Shade, C. M.; Rouge, J. L.; Brown, K. A.; Mirkin, C. A., Modulating the Bond Strength of DNA-Nanoparticle Superlattices. *ACS Nano* **2016**, *10*, 1771-1779.
106. Chen, X.; Karpenko, A.; Lopez-Acevedo, O., Silver-Mediated Double Helix: Structural Parameters for a Robust DNA Building Block. *ACS Omega* **2017**, *2*, 7343-7348.

107. Ono, A.; Cao, S.; Togashi, H.; Tashiro, M.; Fujimoto, T.; Machinami, T.; Oda, S.; Miyake, Y.; Okamoto, I.; Tanaka, Y., Specific interactions between silver(I) ions and cytosine-cytosine pairs in DNA duplexes. *Chem. Commun.* **2008**, *39*, 4825-4827.
108. Oh, T.; Ku, J. C.; Lee, J. H.; Hersam, M. C.; Mirkin, C. A., Density-Gradient Control over Nanoparticle Supercrystal Formation. *Nano Lett.* **2018**, *18*, 6022-6029.
109. Nykypanchuk, D.; Maye, M. M.; van der Lelie, D.; Gang, O., DNA-guided crystallization of colloidal nanoparticles. *Nature* **2008**, *451*, 549-552.
110. Schuller, J. A.; Barnard, E. S.; Cai, W.; Jun, Y. C.; White, J. S.; Brongersma, M. L., Plasmonics for extreme light concentration and manipulation. *Nat. Mater.* **2010**, *9*, 193-204.
111. Maier, S. A.; Kik, P. G.; Atwater, H. A.; Meltzer, S.; Harel, E.; Koel, B. E.; Requicha, A. A. G., Local detection of electromagnetic energy transport below the diffraction limit in metal nanoparticle plasmon waveguides. *Nat. Mater.* **2003**, *2*, 229-232.
112. Zou, S.; Janel, N.; Schatz, G. C., Silver nanoparticle array structures that produce remarkably narrow plasmon lineshapes. *J. Chem. Phys.* **2004**, *120*, 10871-10875.
113. Kumar, K.; Duan, H.; Hegde, R. S.; Koh, S. C.; Wei, J. N.; Yang, J. K., Printing colour at the optical diffraction limit. *Nat. Nanotech.* **2012**, *7*, 557-561.
114. Jiao, Y.; Han, D.; Ding, Y.; Zhang, X.; Guo, G.; Hu, J.; Yang, D.; Dong, A., Fabrication of three-dimensionally interconnected nanoparticle superlattices and their lithium-ion storage properties. *Nat. Commun.* **2015**, *6*, 6420.
115. Choi, J. H.; Wang, H.; Oh, S. J.; Paik, T.; Jo, P. S.; Sung, J.; Ye, X. C.; Zhao, T. S.; Diroll, B. T.; Murray, C. B.; Kagan, C. R., Exploiting the colloidal nanocrystal library to construct electronic devices. *Science* **2016**, *352*, 205-208.
116. Wong, S.; Kitaev, V.; Ozin, G. A., Colloidal crystal films: Advances in universality and perfection. *J. Am. Chem. Soc.* **2003**, *125*, 15589-15598.
117. Kalsin, A. M.; Fialkowski, M.; Paszewski, M.; Smoukov, S. K.; Bishop, K. J. M.; Grzybowski, B. A., Electrostatic self-assembly of binary nanoparticle crystals with a diamond-like lattice. *Science* **2006**, *312*, 420-424.
118. Shevchenko, E. V.; Talapin, D. V.; Kotov, N. A.; O'Brien, S.; Murray, C. B., Structural diversity in binary nanoparticle superlattices. *Nature* **2006**, *439*, 55-59.

119. Srivastava, S.; Santos, A.; Critchley, K.; Kim, K. S.; Podsiadlo, P.; Sun, K.; Lee, J.; Xu, C. L.; Lilly, G. D.; Glotzer, S. C.; Kotov, N. A., Light-Controlled Self-Assembly of Semiconductor Nanoparticles into Twisted Ribbons. *Science* **2010**, *327*, 1355-1359.
120. Liang, Z. J.; Susha, A. S.; Caruso, F., Metallodielectric opals of layer-by-layer processed coated colloids. *Adv. Mater.* **2002**, *14*, 1160-1164.
121. Kiely, C. J.; Fink, J.; Brust, M.; Bethell, D.; Schiffrin, D. J., Spontaneous ordering of bimodal ensembles of nanoscopic gold clusters. *Nature* **1998**, *396*, 444-446.
122. Zhao, Y.; Thorkelsson, K.; Mastroianni, A. J.; Schilling, T.; Luther, J. M.; Rancatore, B. J.; Matsunaga, K.; Jinnai, H.; Wu, Y.; Poulsen, D.; Frechet, J. M. J.; Alivisatos, A. P.; Xu, T., Small-molecule-directed nanoparticle assembly towards stimuli-responsive nanocomposites. *Nat. Mater.* **2009**, *8*, 979-985.
123. Coelho, J. P.; Gonzalez-Rubio, G.; Delices, A.; Barcina, J. O.; Salgado, C.; Avila, D.; Pena-Rodriguez, O.; Tardajos, G.; Guerrero-Martinez, A., Polyrotaxane-Mediated Self-Assembly of Gold Nanospheres into Fully Reversible Supercrystals. *Angew. Chem. Int. Ed.* **2014**, *53*, 12751-12755.
124. Huang, H. Y.; Chen, W. F.; Kuo, P. L., Self-assembly of gold nanoparticles induced by poly(oxypropylene)diamines. *J. Phys. Chem. B* **2005**, *109*, 24288-24294.
125. Cigler, P.; Lytton-Jean, A. K. R.; Anderson, D. G.; Finn, M. G.; Park, S. Y., DNA-controlled assembly of a NaTl lattice structure from gold nanoparticles and protein nanoparticles. *Nat. Mater.* **2010**, *9*, 918-922.
126. Tian, Y.; Zhang, Y. G.; Wang, T.; Xin, H. L. L.; Li, H. L.; Gang, O., Lattice engineering through nanoparticle-DNA frameworks. *Nat. Mater.* **2016**, *15*, 654-661.
127. Wang, Y.; Wang, Y. F.; Zheng, X. L.; Ducrot, E.; Yodh, J. S.; Weck, M.; Pine, D. J., Crystallization of DNA-coated colloids. *Nat. Commun.* **2015**, *6*, 7253.
128. Ross, M. B.; Mirkin, C. A.; Schatz, G. C., Optical Properties of One-, Two-, and Three-Dimensional Arrays of Plasmonic Nanostructures. *J. Phys. Chem. C* **2016**, *120*, 816-830.
129. Esteban, R.; Aizpurua, J.; Bryant, G. W., Strong coupling of single emitters interacting with phononic infrared antennae. *New J. Phys.* **2014**, *16*, 013052.
130. Engheta, N., Circuits with light at nanoscales: Optical nanocircuits inspired by metamaterials. *Science* **2007**, *317*, 1698-1702.

131. O'Brien, M. N.; Jones, M. R.; Mirkin, C. A., The nature and implications of uniformity in the hierarchical organization of nanomaterials. *Proc. Natl. Acad. Sci. U. S. A.* **2016**, *113*, 11717-11725.
132. Whitmer, J. K.; Luijten, E., Sedimentation of aggregating colloids. *J. Chem. Phys.* **2011**, *134*, 034510.
133. Maye, M. M.; Nykypanchuk, D.; van der Lelie, D.; Gang, O., A simple method for kinetic control of DNA-induced nanoparticle assembly. *J. Am. Chem. Soc.* **2006**, *128*, 14020-14021.
134. Avrami, M., Kinetics of Phase Change. II Transformation-Time Relations for Random Distribution of Nuclei. *J. Chem. Phys.* **1940**, *8*, 212-224.
135. Oh, T.; Park, S. S.; Mirkin, C. A., Stabilization of Colloidal Crystals Engineered with DNA. *Adv. Mater.* **2019**, *in press*.
136. Zhang, Y.; Lu, F.; Yager, K. G.; van der Lelie, D.; Gang, O., A general strategy for the DNA-mediated self-assembly of functional nanoparticles into heterogeneous systems. *Nat. Nanotech.* **2013**, *8*, 865-872.
137. Wang, Y. F.; Jenkins, I. C.; McGinley, J. T.; Sinno, T.; Crocker, J. C., Colloidal crystals with diamond symmetry at optical lengthscales. *Nat. Commun.* **2017**, *8*, 14173.
138. Swasey, S. M.; Leal, L. E.; Lopez-Acevedo, O.; Pavlovich, J.; Gwinn, E. G., Silver (I) as DNA glue: Ag⁺-mediated guanine pairing revealed by removing Watson-Crick constraints. *Sci. Rep.* **2015**, *5*, 10163.
139. Liu, H. H.; Shen, F. S.; Haruehanroengra, P.; Yao, Q. Q.; Cheng, Y. S.; Chen, Y. Q.; Yang, C.; Zhang, J.; Wu, B. X.; Luo, Q.; Cui, R. X.; Li, J. X.; Ma, J. B.; Sheng, J.; Gan, J. H., A DNA Structure Containing Ag-I-Mediated G:G and C:C Base Pairs. *Angew. Chem. Int. Ed.* **2017**, *56*, 9430-9434.
140. Swasey, S. M.; Gwinn, E. G., Silver-mediated base pairings: towards dynamic DNA nanostructures with enhanced chemical and thermal stability. *New J. Phys.* **2016**, *18*, 045008.
141. Ennifar, E.; Walter, P.; Dumas, P., A crystallographic study of the binding of 13 metal ions to two related RNA duplexes. *Nucleic Acids Res.* **2003**, *31*, 2671-2682.
142. Miyake, Y.; Togashi, H.; Tashiro, M.; Yamaguchi, H.; Oda, S.; Kudo, M.; Tanaka, Y.; Kondo, Y.; Sawa, R.; Fujimoto, T.; Machinami, T.; Ono, A., Mercury(II)-mediated formation of thymine-Hg-II-thymine base pairs in DNA duplexes. *J. Am. Chem. Soc.* **2006**, *128*, 2172-2173.

143. Urata, H.; Yamaguchi, E.; Nakamura, Y.; Wada, S., Pyrimidine-pyrimidine base pairs stabilized by silver(I) ions. *Chem. Commun.* **2011**, *47*, 941-943.
144. Funai, T.; Miyazaki, Y.; Aotani, M.; Yamaguchi, E.; Nakagawa, O.; Wada, S.; Torigoe, H.; Ono, A.; Urata, H., AgI Ion Mediated Formation of a C-A Mismatch by DNA Polymerases. *Angew. Chem. Int. Ed.* **2012**, *51*, 6464-6466.
145. Kondo, J.; Tada, Y.; Dairaku, T.; Hattori, Y.; Saneyoshi, H.; Ono, A.; Tanaka, Y., A metallo-DNA nanowire with uninterrupted one-dimensional silver array. *Nat. Chem.* **2017**, *9*, 956-960.
146. Mason, J. A.; Laramy, C. R.; Lai, C. T.; O'Brien, M. N.; Lin, Q. Y.; Dravid, V. P.; Schatz, G. C.; Mirkin, C. A., Contraction and Expansion of Stimuli-Responsive DNA Bonds in Flexible Colloidal Crystals. *J. Am. Chem. Soc.* **2016**, *138*, 8722-8725.
147. Williamson, G. K.; Hall, W. H., X-Ray Line Broadening from Filled Aluminium and Wolfram. *Acta Metall. Mater.* **1953**, *1*, 22-31.
148. Volkov, I. L.; Smirnova, A.; Makarova, A. A.; Reveguk, Z. V.; Ramazanov, R. R.; Usachov, D. Y.; Adamchuk, V. K.; Kononov, A. I., DNA with Ionic, Atomic, and Clustered Silver: An XPS Study. *J. Phys. Chem. B* **2017**, *121*, 2400-2406.
149. Izatt, R. M.; Christensen, J. J.; Rytting, J. H., Sites and Thermodynamic Quantities Associated with Proton and Metal Ion Interaction with Ribonucleic Acid, Deoxyribonucleic Acid, and Their Constituent Bases, Nucleosides, and Nucleotides. *Chem. Rev.* **1971**, *71*, 439-481.
150. Okamoto, I.; Iwamoto, K.; Watanabe, Y.; Miyake, Y.; Ono, A., Metal-Ion Selectivity of Chemically Modified Uracil Pairs in DNA Duplexes. *Angew. Chem. Int. Ed.* **2009**, *48*, 1648-1651.
151. Madou, M. J., *Fundamentals of microfabrication : the science of miniaturization*. CRC Press: Boca Raton, Fla., 2002.
152. Auyeung, E.; Morris, W.; Mondloch, J. E.; Hupp, J. T.; Farha, O. K.; Mirkin, C. A., Controlling Structure and Porosity in Catalytic Nanoparticle Superlattices with DNA. *J. Am. Chem. Soc.* **2015**, *137*, 1658-1662.
153. Murray, C. B.; Kagan, C. R.; Bawendi, M. G., Synthesis and characterization of monodisperse nanocrystals and close-packed nanocrystal assemblies. *Annu. Rev. Mater. Sci.* **2000**, *30*, 545-610.
154. Redl, F. X.; Cho, K. S.; Murray, C. B.; O'Brien, S., Three-dimensional binary superlattices of magnetic nanocrystals and semiconductor quantum dots. *Nature* **2003**, *423*, 968-971.

155. Dong, A. G.; Ye, X. C.; Chen, J.; Murray, C. B., Two-Dimensional Binary and Ternary Nanocrystal Superlattices: The Case of Monolayers and Bilayers. *Nano Lett.* **2011**, *11*, 1804-1809.
156. Paik, T.; Diroll, B. T.; Kagan, C. R.; Murray, C. B., Binary and Ternary Superlattices Self-Assembled from Colloidal Nanodisks and Nanorods. *J. Am. Chem. Soc.* **2015**, *137*, 6662-6669.
157. Ma, K.; Yehezkeli, O.; Domaille, D. W.; Funke, H. H.; Cha, J. N., Enhanced Hydrogen Production from DNA-Assembled Z-Scheme TiO₂-CdS Photocatalyst Systems. *Angew. Chem. Int. Ed.* **2015**, *54*, 11490-11494.
158. He, L. C.; Brasino, M.; Mao, C. C.; Cho, S.; Park, W.; Goodwin, A. P.; Cha, J. N., DNA-Assembled Core-Satellite Upconverting-Metal-Organic Framework Nanoparticle Superstructures for Efficient Photodynamic Therapy. *Small* **2017**, *13*.
159. Ma, K.; Harris, A. W.; Cha, J. N., DNA assembled photoactive systems. *Curr. Opin. Colloid In.* **2018**, *38*, 18-29.
160. Ma, K.; Yehezkeli, O.; He, L. C.; Cha, J. N., DNA for Assembly and Charge Transport Photocatalytic Reduction of CO₂. *Adv. Sustain. Syst.* **2018**, *2*.
161. Goodman, S. M.; Siu, A.; Singh, V.; Nagpal, P., Long-range energy transfer in self-assembled quantum dot-DNA cascades. *Nanoscale* **2015**, *7*, 18435-18440.
162. Keren, K.; Berman, R. S.; Buchstab, E.; Sivan, U.; Braun, E., DNA-templated carbon nanotube field-effect transistor. *Science* **2003**, *302*, 1380-1382.
163. Yan, H.; Park, S. H.; Finkelstein, G.; Reif, J. H.; LaBean, T. H., DNA-templated self-assembly of protein arrays and highly conductive nanowires. *Science* **2003**, *301*, 1882-1884.
164. Park, S. H.; Prior, M. W.; LaBean, T. H.; Finkelstein, G., Optimized fabrication and electrical analysis of silver nanowires templated on DNA molecules. *Appl. Phys. Lett.* **2006**, *89*.
165. Jin, Z.; Sun, W.; Ke, Y.; Shih, C. J.; Paulus, G. L. C.; Wang, Q. H.; Mu, B.; Yin, P.; Strano, M. S., Metallized DNA nanolithography for encoding and transferring spatial information for graphene patterning. *Nat. Commun.* **2013**, *4*, 1663.
166. Schmidbaur, H.; Schier, A., Argentophilic Interactions. *Angew. Chem. Int. Ed.* **2015**, *54*, 746-784.
167. Auffinger, P.; Ennifar, E., Silver-wired DNA. *Nat. Chem.* **2017**, *9*, 932-934.

168. Lerch, S.; Reinhard, B. M., Effect of interstitial palladium on plasmon-driven charge transfer in nanoparticle dimers. *Nat. Commun.* **2018**, *9*, 168.
169. Raino, G.; Becker, M. A.; Bodnarchuk, M. I.; Mahrt, R. F.; Kovalenko, M. V.; Stoferle, T., Superfluorescence from lead halide perovskite quantum dot superlattices. *Nature* **2018**, *563*, 671-675.
170. Harman, T. C.; Taylor, P. J.; Walsh, M. P.; LaForge, B. E., Quantum dot superlattice thermoelectric materials and devices. *Science* **2002**, *297*, 2229-2232.

Appendix A. Supplementary Images and Information for Chapter 2



Figure A.1. Additional STEM micrographs for the directed assemblies of 20 nm Au nanoparticles onto the selectively functionalized barrels of Au nanorods.

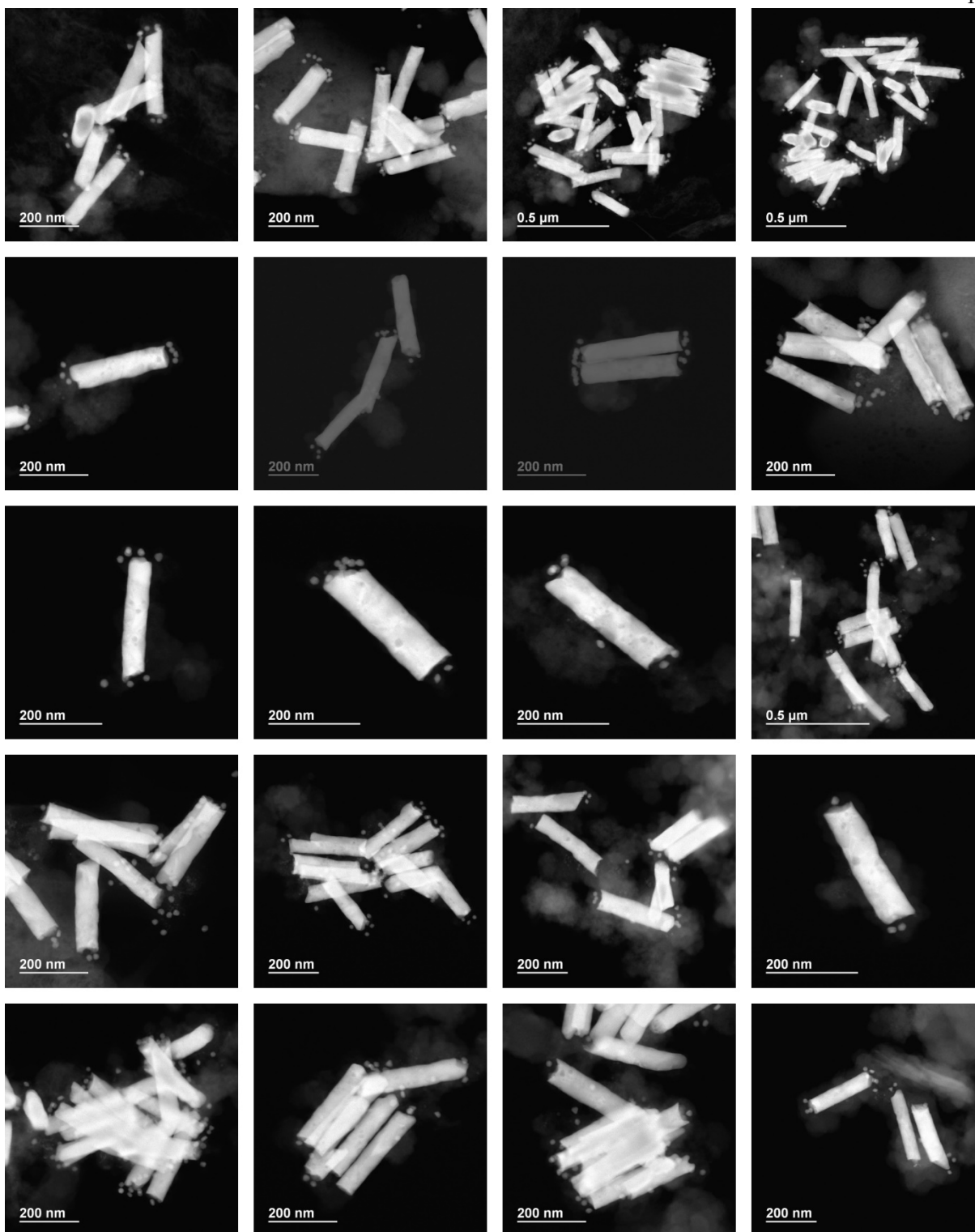


Figure A.2. Additional STEM micrographs for the directed assemblies of 20 nm Au nanoparticles onto the selectively functionalized bases of Au nanorods.

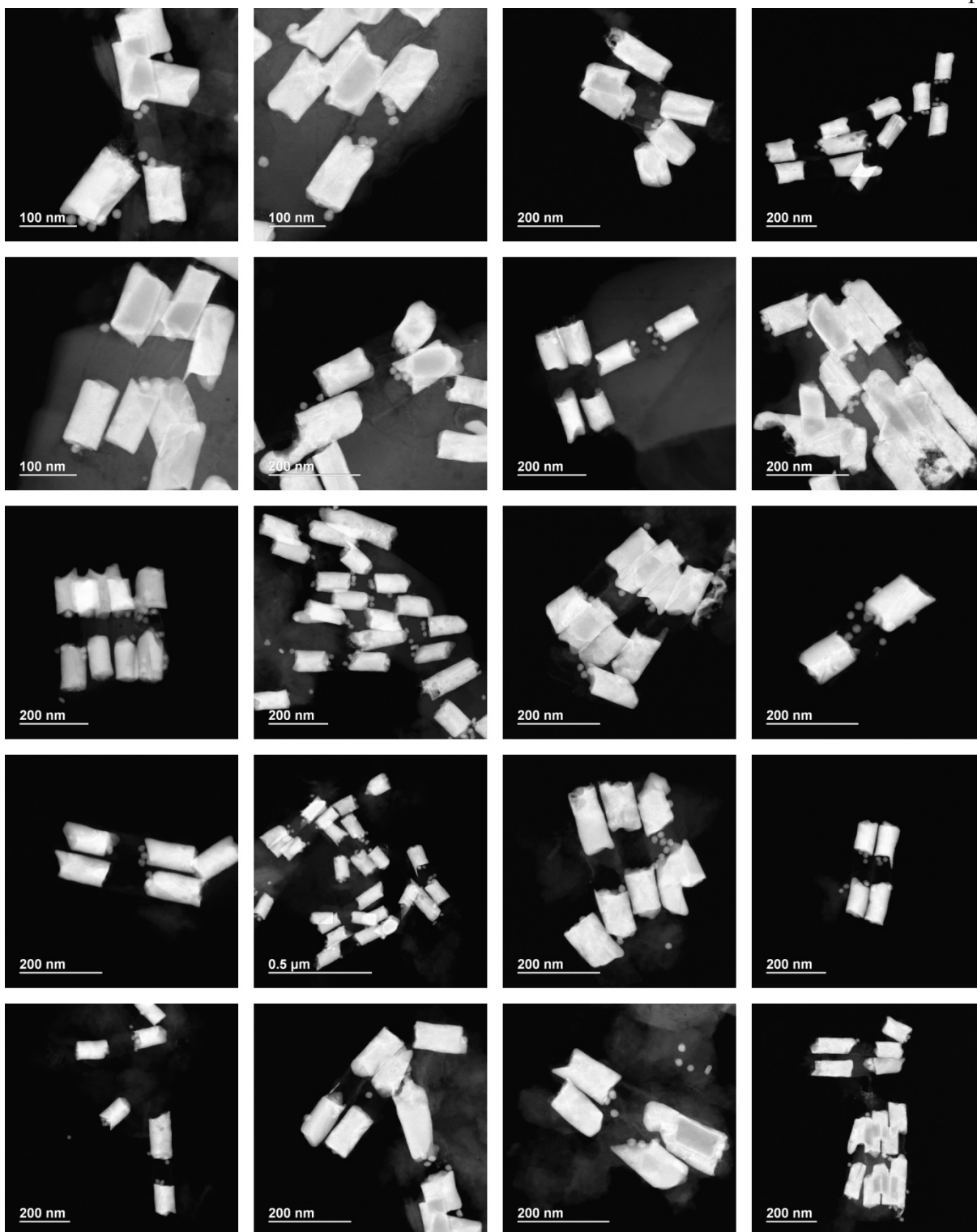


Figure A.3. Additional STEM micrographs for the directed assemblies of 20 nm Au nanoparticles onto the selectively functionalized gaps of Au nanorod dimers.

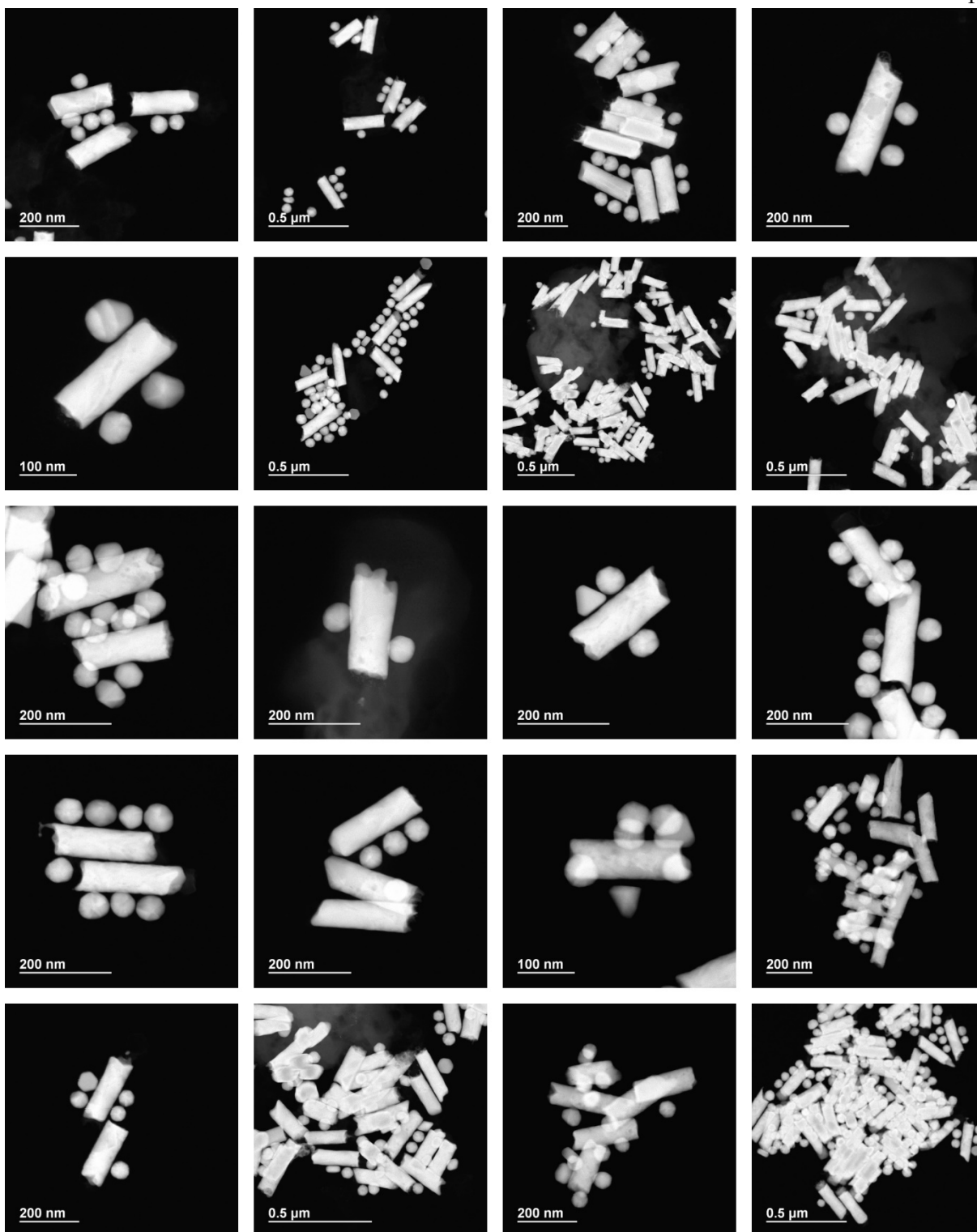


Figure A.4. Additional STEM micrographs for the directed assemblies of 60 nm Au nanoparticles onto the selectively functionalized barrels of Au nanorods.



Figure A.5. Additional STEM micrographs for the directed assemblies of 60 nm Au nanoparticles onto the selectively functionalized bases of Au nanorods.

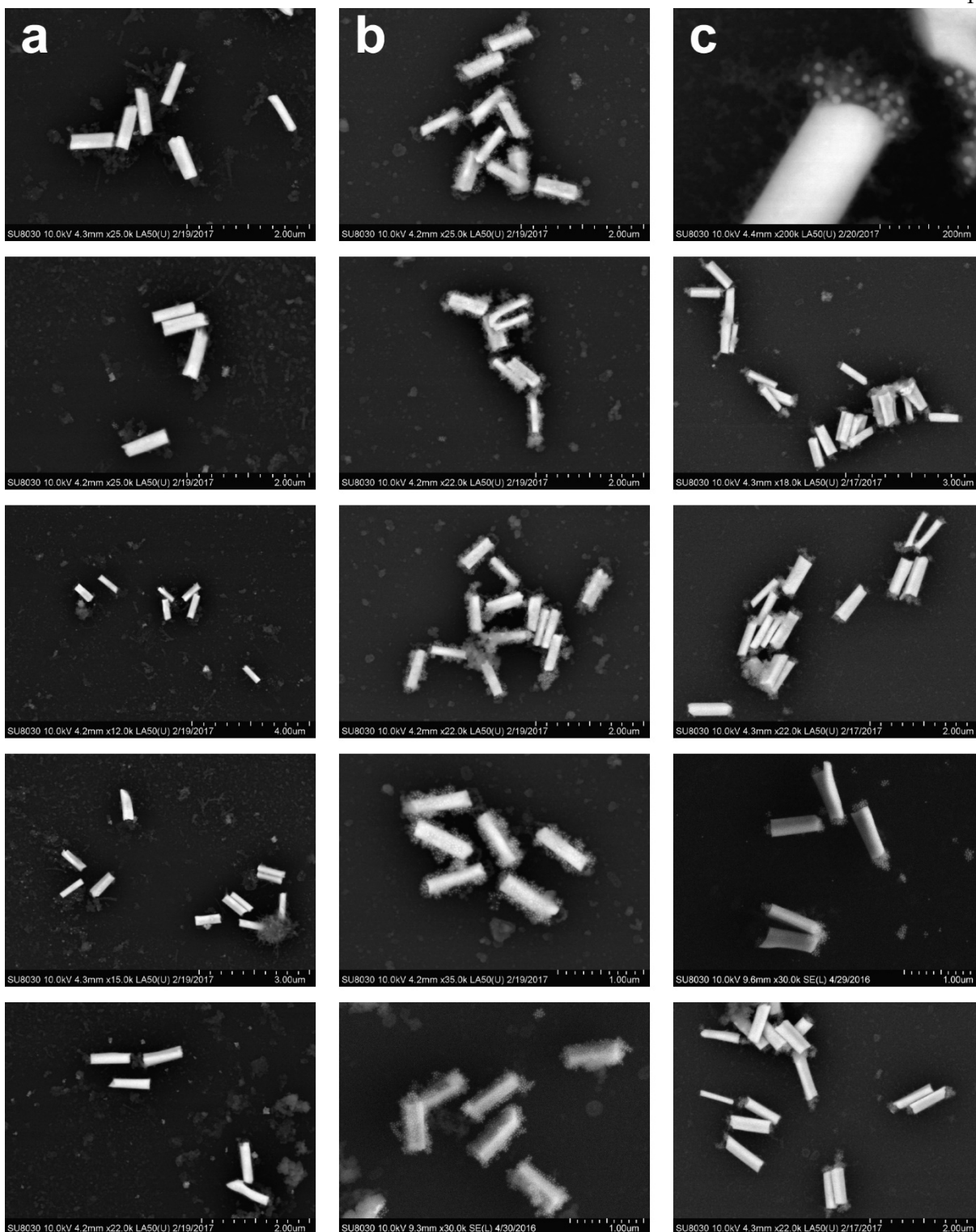


Figure A.6. Additional SEM micrographs for the substrate assemblies of 20 nm Au nanoparticles onto the DNA-functionalized Au nanorod: (a) without functionalization, (b) non-selective functionalization, and (c) selectively functionalization on the bases.

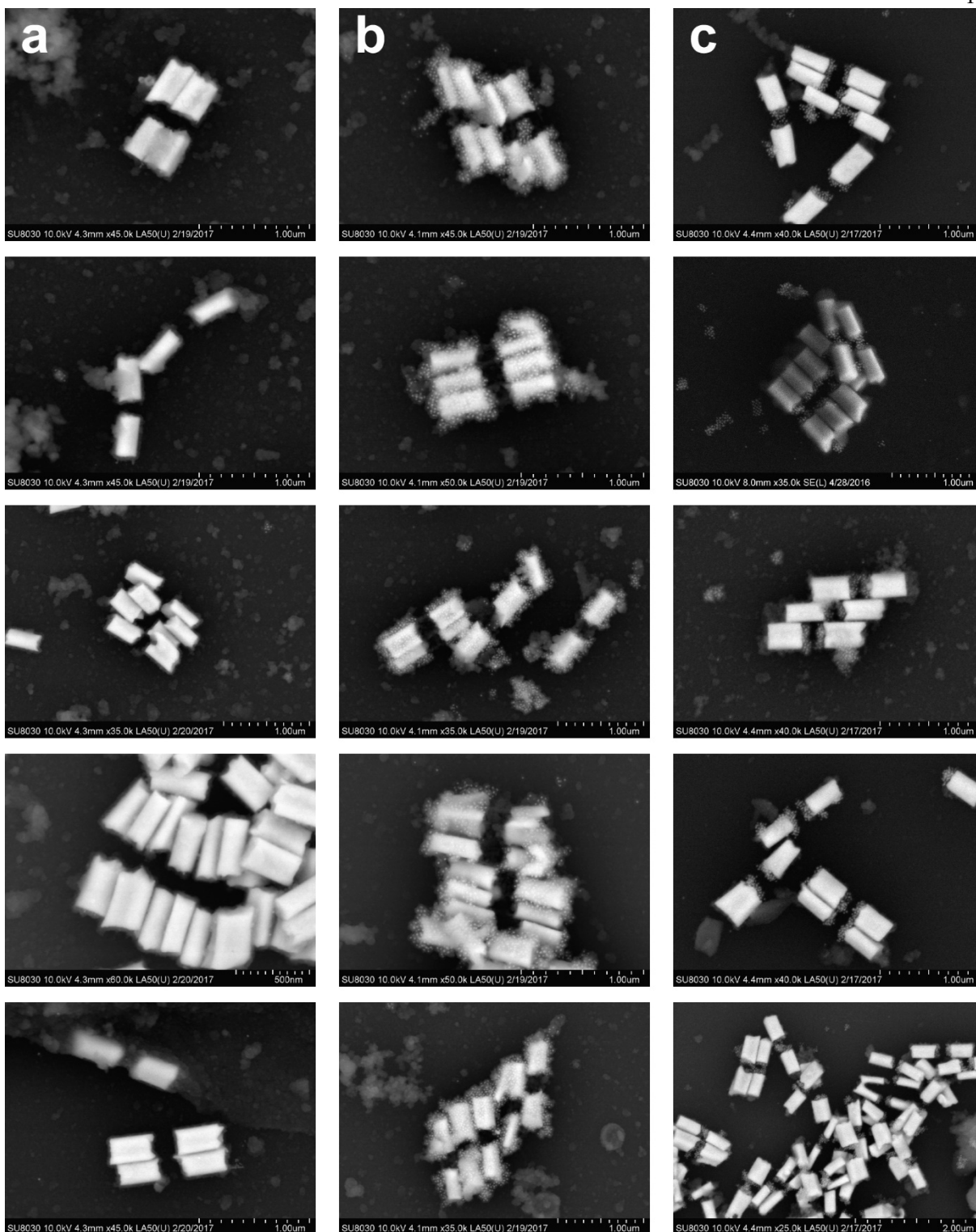


Figure A.7. Additional SEM micrographs for the substrate assemblies of 20 nm Au nanoparticles onto the DNA-functionalized Au nanorod dimers: (a) without functionalization, (b) non-selective functionalization, and (c) selectively functionalization in the gap.

Table A.1. Yields for the orthogonal functionalization of different faces of the nanowire and the gaps formed between two nanowires, in solution and when cast on a SiO₂ substrate. Statistical analyses were based upon electron microscopy (Figure S4-10).

	In aqueous solution: ends 20 nm	In aqueous solution: Sides 20 nm	In aqueous solution: Gaps 20 nm	In aqueous solution: Ends 60 nm	In aqueous solution: Sides 60 nm	Assembly of DNA-modified particles on rod ends functionalized with complementary DNA, when cast on a SiO ₂ substrate	Assembly of DNA-modified particles in gaps between rod dimers functionalized with complementary DNA when cast on a SiO ₂ substrate
Total count	125	86	63	95	121	58	47
Particles only on designated sites	100	73	48	73	106	51	40
Uncertain	20	11	7	3	11	7	7
No particles around	5	2	8	19	4	0	0
Yield	80%	85%	76%	77%	88%	88%	85%

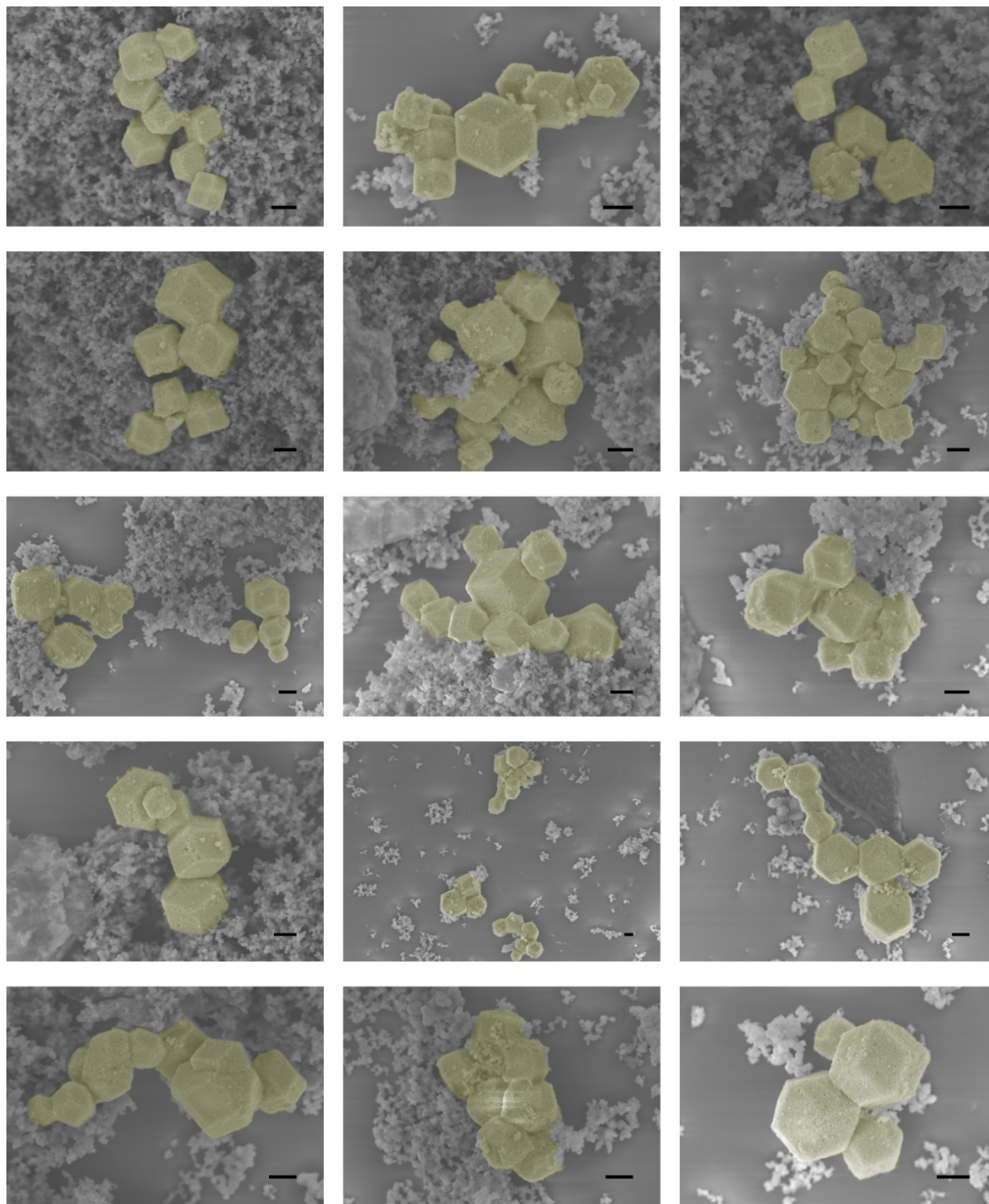
Appendix B. Supplementary Figures for Chapter 3

Figure B.1. Supplementary SEM micrographs of PAE colloidal crystals (20 nm Au nanoparticles and $n = 1$ DNA linkers) assembled without quenching sublayer. The colloidal crystals have been false colored to distinguish from the silica debris. All scale bars: 1 μm .

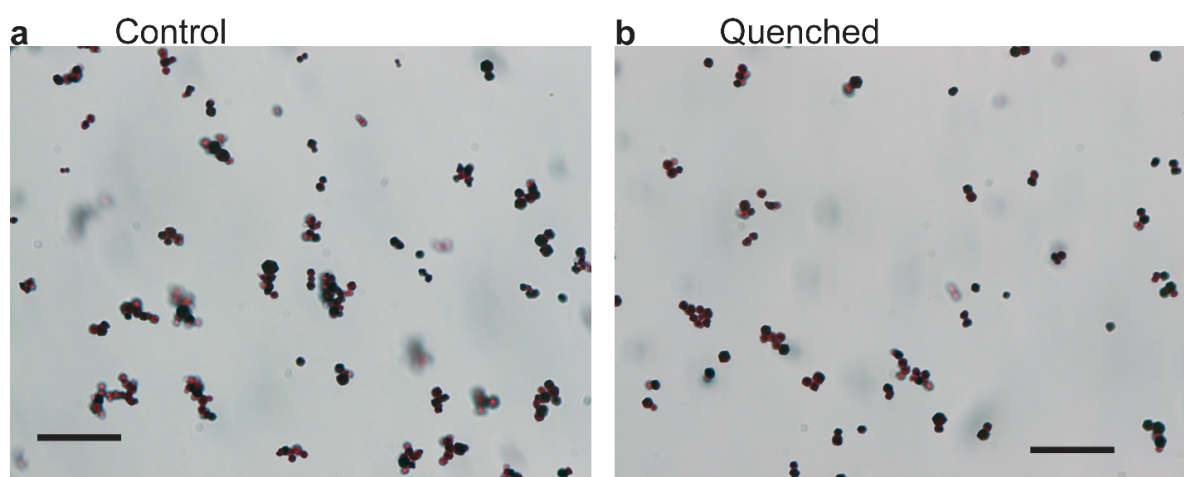


Figure B.2. Optical micrographs showing the wide-angle view of assembled microcrystals with 20 nm Au nanoparticles and $n = 1$ DNA linkers, in (a) control and (b) quenched samples. Scale bars: 10 μm .

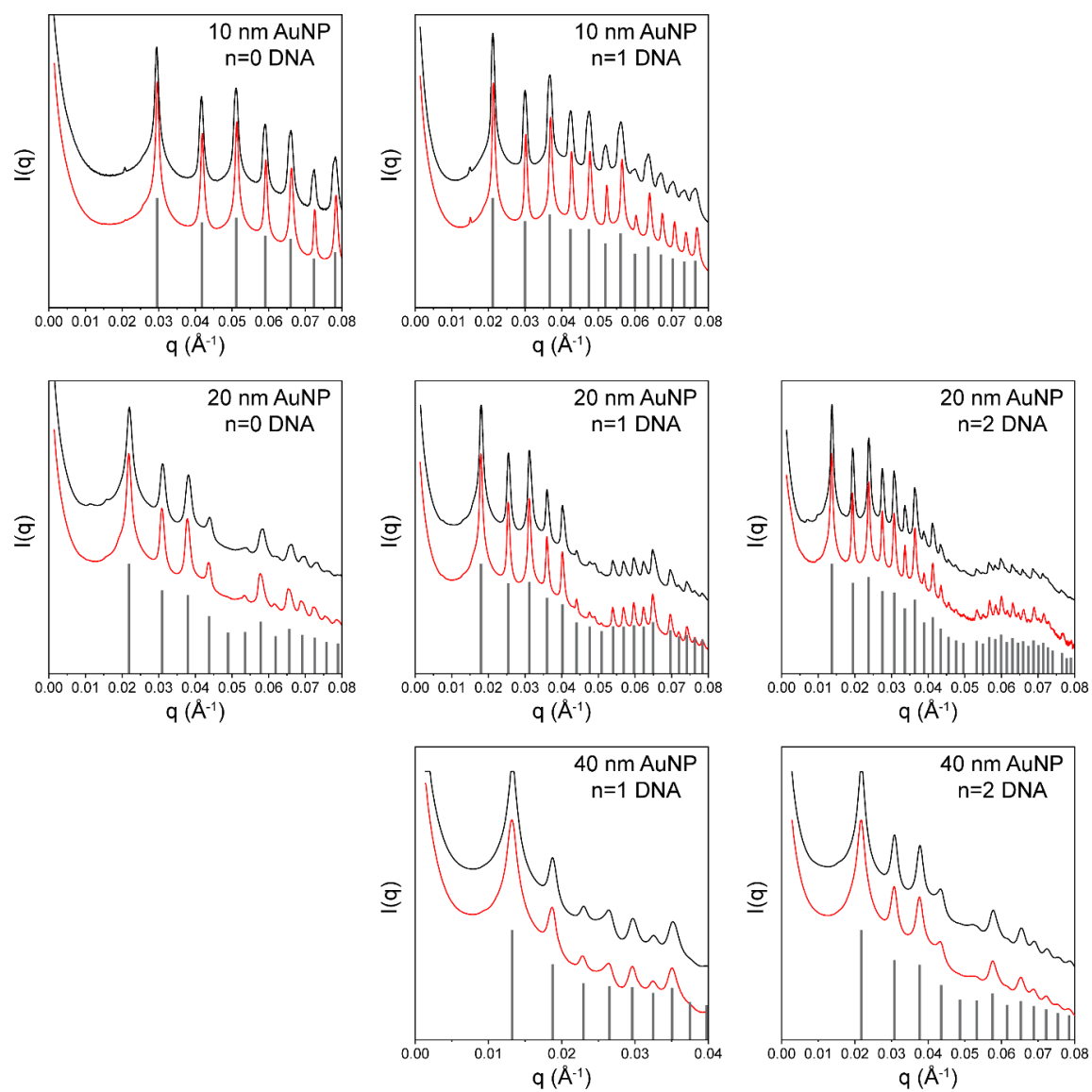


Figure B.3. Radially averaged one-dimensional SAXS patterns showing the same diffraction patterns (bcc) but different lattice parameters for the PAE systems studied. The parameters are tabulated in **Table 3.7.**

Curriculum Vitae

Taegon Oh

taegon.oh@u.northwestern.edu

2215 Maple Ave, APT D3

(217) 979-7815

Evanston, IL 60201

EDUCATION

Northwestern University

Evanston, Illinois

Ph. D. Candidate in Materials Science and Engineering

Sep 2013 – Mar 2019

Dissertation title: “Expanding the Properties and Utility of DNA-Engineered Nanoparticle Superlattices through Monodispersity, Metallization, and Interfacing with Electronic Circuitry”

Doctoral advisor: Professor Chad A. Mirkin. GPA – 3.78/4.00

University of Illinois at Urbana-Champaign

Urbana, Illinois

Master of Science in Material Science & Engineering

May 2013

Thesis title: “Dissociation of Carbon Dioxide in Atmospheric Pressure Microchannel Plasma Devices”

Thesis advisor: Professor J. Gary Eden. GPA – 3.89/4.00

Bachelor of Science in Material Science & Engineering, with Minor in Chemistry
with Highest Honor. GPA – 3.89/4.00

May 2013

RESEARCH EXPERIENCE

Mirkin Research Group – Research Assistant

Evanston, Illinois

- DNA-mediated colloidal crystal engineering Oct 2013 – present
 - Uniform synthesis of colloidal single crystals engineered by DNA
 - Metallo DNA as molecular wires for nanoparticle communication and energy transport
- Surface modification of nanomaterials with oligonucleotides
 - Orthogonal chemical modification for multifunctional nanomaterials and guided assembly
- Templated electrochemical synthesis of nanostructures and nanowire-based device fabrication

Laboratory for Optical Physics and Engineering – Research Assistant

Champaign, Illinois

- Microchannel array devices for microplasmas Oct 2009 - May 2013
 - Flexible microplasma devices using UV-transparent silicone polymers
 - Gaseous chemistry in microplasmas for CO₂ reduction

AWARDS / HONORS / FELLOWSHIPS

NUANCE Center Image Contest – Grand Prize

Oct 2018

The Graduate School Travel Grant

Mar 2018

Kwanjeong Fellowship

Sep 2013 – Aug 2018

Korean American Scientists and Engineers Association Scholarships

May 2016

NUANCE Center Image Contest – Honorable Mention

Jan 2016

Samsung Scholarship

Aug 2008 - May 2012

Lucille and Charles Wert Scholarship

April 2011

Alfred W. Allen Award

April 2009

Dean’s List – all 6 semesters

Fall 2008 - Spring 2011

Samsung Electronics Frontier Membership

2008 - present

39th International Chemistry Olympiad – Gold Medal

Aug 2007

TEACHING EXPERIENCE

Northwestern University – <i>Teaching Assistant</i>	Evanston, Illinois
• Analytic Electron Microscopy (by Professor Vinayak P. Dravid)	Mar 2016 - Jun 2016
• Materials Selection (by Professor Stephen Carr)	Jan 2018 – Mar 2018
University of Illinois at Urbana-Champaign – <i>Teaching Assistant</i>	Urbana, Illinois
• Electronic Properties of Solids (by Professor John H. Weaver)	Jan 2011 - May 2011
Mirae Yeongjae (Private Science Institute) – <i>Chemistry Teacher</i>	Seoul, Korea; 2008
2008 Korean Chemistry Olympiad Winter School – <i>Teaching Assistant</i>	Daejeon, Korea; 2008

PUBLICATIONS

-
- ***Oh, T.**; *Park, S. S.; Walker, D. D.; Hendon, C. H.; Mirkin, C. A. “Conductive metallo-DNA as Programmable Molecular Wires between Nanoparticles,” *in preparation*.
- *Seo, E. S.; ***Oh, T.**; Mirkin, C. A. “Triakis Tetrahedral Colloidal Crystals Assembled with DNA,” *in preparation*.
- *Lee, S. –H.; ***Oh, T.**; Mirkin, C. A.; Jang, J. –W. “Defining Optomagnetic Interactions in Fe Nanowire-Au Nanoring Hybrid Structures through Coaxial Lithography,” *in preparation*.
- ***Oh, T.**; *Park, S. S.; Mirkin, C. A. “Stabilization of Colloidal Crystals Engineered with DNA,” *Advanced Materials*, doi: 10.1002/adma.201805480.
- Oh, T.**; Ku, J. C.; Lee, J. –H.; Hersam, M. C.; Mirkin, C. A. “Density-Gradient Control over Nanoparticle Supercrystal Formation,” *Nano Letters*, **2018**, *18*, 6022-6029.
- Oh, T.**; Ku, J. C.; Ozel, T.; Mirkin, C. A. “Orthogonal Chemical Modification of Template-Synthesized Nanostructures with DNA,” *Journal of the American Chemical Society*, **2017**, *139*, 6831–6834.
- Shin, C.; **Oh, T.**; Houlahan, Jr., T. J.; Fann, C. –H.; Park, S. –J.; Eden, J. G. “Dissociation of Carbon Dioxide in Arrays of Microchannel Plasmas,” *Journal of Physics D: Applied Physics*, **2018**, doi: 10.1088/1361-6463/aaf37a.
- Lee, S. –H.; Lee, S. W.; **Oh, T.**; Mirkin, C. A.; Jang, J. –W. “Direct Observation of Plasmon-Induced Interfacial Charge Separation in Metal/Semiconductor Hybrid Nanostructures under Plasmon-Exiton Coupling via Detecting Surface Potentials,” *Nano Letters*, **2018**, *18*, 109-116.
- Kuang, W. –J.; Li, Q.; Tolner, H.; **Oh, T.**; Park, S. –J.; Eden, J. G. “Large-Area Polymeric Microplasma Devices with Elongated Lifetime for Flexible Display and Photonic Applications,” *IEEE Electron Device Letters*, **2014**, *35*, 765-767.

PATENT APPLICATION

-
- Mirkin C. A.; **Oh, T.**; Park, S. S. “Stabilization of Colloidal Crystals Engineered with Nucleic Acid,” filed Sep. 25, 2018, U.S. Patent No. 62/736,260.

PRESENTATIONS

-
- Oh, T.** “Advanced Production Processes for Colloidal Crystals Engineered with DNA.” *SPIE-MRSEC Student Seminar Series*, Evanston, IL, USA, Nov. 9, 2018.
- Oh, T.**; Park, J.; Ku, J. C.; Ozel, T.; Mirkin, C. A. “Orthogonal Chemical Modification of Template-Synthesized Nanostructures with Oligonucleotides.” *ACS National Meeting & Expo*, New Orleans, LA, USA, Mar. 18, 2018.

PRESENTATIONS (Continued)

- Mirkin, C. A. & Jang, J. –W. “Plasmonic Optoelectronic Interactions.” *US-Korea Nano-Bio-Information Technology (NBIT) Program Review and Nanoscience Technical Exchange*, Dayton, OH, USA, Jul. 24-25, 2017. **(on behalf of Prof. Chad Mirkin)**
- Mirkin, C. A. & Jang, J. –W. “Plasmonic Optoelectronic Interactions.” *US-Korea Nano-Bio-Information Technology (NBIT) Program Review and Nanoscience Technical Exchange*, Xitou, Taiwan, Aug. 8-12, 2016. **(on behalf of Prof. Chad Mirkin)**
- Oh, T.**; Ku, J. C.; Seo, E. S.; Ashley, M. J.; Ross, M. B.; Mirkin, C. A. “Elucidating the Transport Properties of Interconnected DNA Networks.” *Multidisciplinary University Research Initiative (MURI): Conductive DNA Systems and Molecular Devices: Annual Review*, Evanston, IL, USA, Oct. 23, 2015.
- Mirkin, C. A. & Jang, J. –W. “Plasmonic Optoelectronic Interactions.” *US-Korea Nano-Bio-Information Technology (NBIT) Program Review and Nanoscience Technical Exchange*, Seoul, South Korea, October 26-30, 2015. **(on behalf of Prof. Chad Mirkin)**
- Oh, T.**; Ku, J. C.; Ozel, T.; Brown, K. A.; Ashley, M. J.; Mirkin, C. A. “Elucidating the Transport Properties of Interconnected DNA Networks.” *Multidisciplinary University Research Initiative (MURI): Conductive DNA Systems and Molecular Devices: Annual Review*, Evanston, IL, USA, Nov. 21, 2015.
- Oh, T.**; Park, J. H.; Kwon, H. P.; Park, S. –J.; Eden, J. G. “Spectroscopic Analysis and Plasma Chemistry of Atmospheric Pressure Carbon Dioxide Plasma in Arrays of Microchannel Devices.” Institute of Electrical and Electronics Engineering, *IEEE Pulsed Power & Plasma Science 2013*, San Francisco, CA, Jun. 16-21, 2013.
- Kuang, W. –J.; Li, Q., **Oh, T.**, Park, S. –J., Eden, J. G., “Demonstration of Large Scale Polymeric Microplasma Devices with Elongated Lifetime for Flexible Display and Photonic Applications.” Institute of Electrical and Electronics Engineering, *IEEE Pulsed Power & Plasma Science 2013*, San Francisco, CA, Jun. 16-21, 2013.
- Oh, T.**; Park, S. –J.; Eden, J. G., “Dissociation and Conversion of Carbon Dioxide in Arrays of Atmospheric Pressure Microplasma Devices.” Institute of Electrical and Electronics Engineering, *39th IEEE International Conference on Plasma Science*, Edinburg, UK, Jul. 8-13, 2012.
- Oh, T.**; Kim, T.; Ma, J. H.; Park, S. –J.; Eden, J. G., “Flexible and Transparent Microplasma Devices for Ultraviolet Medical Treatment.” Institute of Electrical and Electronics Engineering, *38th IEEE International Conference on Plasma Science*, Chicago, IL, Jun. 26-30, 2011.